

***Ab initio* Investigations of the Intrinsic Optical Properties of Germanium and Silicon Nanocrystals**

Dissertation

zur Erlangung des akademischen Grades
doctor rerum naturalium (Dr. rer. nat.)

vorgelegt dem Rat der Physikalisch-Astronomischen Fakultät
der Friedrich-Schiller-Universität Jena

von Dipl.-Phys. Hans-Christian Weißker
geboren am 12. Juli 1971 in Greiz

Gutachter:

1. Prof. Dr. Friedhelm Bechstedt, Jena.
2. Dr. Lucia Reining, Palaiseau, Frankreich.
3. Prof. Dr. Victor Borisenko, Minsk, Weißrußland.

Tag der letzten Rigorosumsprüfung: 12. August 2004.

Tag der öffentlichen Verteidigung: 19. Oktober 2004.

Why is warrant
important to knowledge?
In part because
true opinion
might be reached by
arbitrary, unreliable means.

Peter Railton¹

¹*Explanation and Metaphysical Controversy*, in P. Kitcher and W.C. Salmon (eds.), *Scientific Explanation*, Vol. 13, Minnesota Studies in the Philosophy of Science, Minnesota, 1989.

Contents

1	Introduction	7
2	Theoretical Foundations	13
2.1	Density-Functional Theory	13
2.1.1	The Hohenberg-Kohn Theorem	13
2.1.2	The Kohn-Sham scheme	15
2.1.3	Transition to system without spin-polarization	17
2.1.4	Physical interpretation by comparison to Hartree-Fock	17
2.1.5	LDA and LSDA	19
2.1.6	Forces in DFT	19
2.2	Excitation Energies	20
2.2.1	Quasiparticles	20
2.2.2	Self-energy corrections	22
2.2.3	Excitation energies from total energies	25
2.2.3.1	Conventional Δ SCF method: $E_g^{\text{QP}} = I - A$	25
2.2.3.2	Discussion of the Δ SCF method $E_g^{\text{QP}} = I - A$	25
2.2.3.3	Δ SCF with occupation constraint	28
2.2.4	Other methods to calculate excitation energies of nanostructures	29
2.2.5	Spin: singlet vs. triplet excitons	31
2.2.6	Stokes shifts	32
2.3	Optical Properties	33
2.3.1	Dielectric function	33
2.3.2	Radiative recombination	35
2.4	Projector-Augmented-Wave Method and Matrix Elements	35
3	Model, Method, and Numerical Implementation	39
3.1	Model	39
3.1.1	Free crystallites	39
3.1.2	Crystallites embedded in a crystalline matrix	40
3.2	Electronic-Structure Calculations	41
3.2.1	Supercell method and description of NCs	41
3.2.2	Algorithms and potentials	41
3.2.3	\mathbf{k} points and cell size	42
3.2.4	Cut-off energies	44
3.3	Ionic Relaxations	44
3.4	Calculation of the Dielectric Function	45
3.4.1	Number of conduction bands	46

<i>CONTENTS</i>	3
3.4.2 BZ integration: Tetrahedron method	46
3.4.3 Extrapolation	49
3.4.4 Resampling – tetrahedron mesh	50
3.4.5 Band kissing / Anticrossing correction	53
3.4.6 Spurious transitions	55
3.4.7 Matrix element extrapolation	56
3.5 Results for Constituents	57
4 Results	61
4.1 Free, H-terminated Nanocrystals	61
4.1.1 Structure and importance of relaxation	61
4.1.2 Excitation energies	65
4.1.3 Exchange splitting	70
4.1.4 Transition probabilities	71
4.1.5 Radiative lifetimes	72
4.1.6 Spectra	74
4.2 Alloying: Germanium and Silicon	77
4.3 Embedment of the NCs	80
4.3.1 Electronic properties	80
4.3.2 Optical spectra	82
4.3.3 Hexagonal matrix and NCs	83
4.3.4 Influence of relaxation	84
4.4 Beyond the Ground-State Equilibrium	86
4.4.1 Pressure/ Strain	86
4.4.2 Stokes shifts	88
5 Conclusion and Prospectives	91
Acknowledgments	97
References	99
Deutsche Zusammenfassung	i
Ehrenwörtliche Erklärung	vii
Lebenslauf	ix
Publikationsliste	x
Vortragsliste	xii

List of Figures

2.1	Schematic of V_{xc} discontinuity	22
2.2	Cancellation of Coulomb and self-energy effects	24
2.3	Stoke shift: Schematic	32
3.1	Cubic GeSi NC in hexagonal SiC	40
3.2	Model structure: 83-atom NC free and embedded.	40
3.3	Number of Ge valence electrons: 4 vs. 22	42
3.4	Comparison of PAW and norm-conserving pseudopotential: Spectra	42
3.5	Convergence of electronic structure: \mathbf{k} points.	43
3.6	Convergence with cell size: Bands	43
3.7	Convergence with cell size: Spectra	43
3.8	Convergence: Energy cut-off for PAW data sets	44
3.9	Convergence: Energy cut-off and spectra	44
3.10	Relaxation algorithms	45
3.11	Convergence of ionic relaxation: $\text{Si}_{41}\text{H}_{60}$ excited state	45
3.12	Convergence of ionic relaxation: $\text{Si}_{41}\text{H}_{60}$ ground state	45
3.13	Contribution of band pairs to spectra.	46
3.14	Schematic of tetrahedron	48
3.15	Quality of matrix elements	49
3.16	Resampling: Tetrahedron meshes	49
3.17	Linear vs. quadratic extrapolation	49
3.18	Weight problem vs. symmetry-equivalent tetrahedron corners	52
3.19	Band integration parameter	52
3.20	Extrapolation: Number of bands in $\mathbf{k}\cdot\mathbf{p}$ expression	53
3.21	Anticrossing / “Kissing” correction	53
3.22	Applicability tetrahedron method: cell size	53
3.23	Supercells: Recovering the joint density of states	55
3.24	Density of states	55
3.25	Embedded structures: Applicability of extrapolative tetrahedron method	55
3.26	Bulk bands Ge: Theoretical lattice constant vs. SiC lattice constant	58
3.27	Bulk bands Si: Theoretical lattice constant vs. SiC lattice constant	58
3.28	Bulk bands SiC: Theoretical lattice constant	58
3.29	Spectra of the constituent materials of the NCs	58

4.1	Averaged interatomic distances	62
4.2	Bond-lengths distribution	62
4.3	Relaxation pattern	63
4.4	Wave functions near HOMO-LUMO gap	63
4.5	Effect of relaxation on excitation energies	64
4.6	Effect of relaxation on radiative lifetimes	64
4.7	Effect of relaxation on oscillator strengths of lowest transitions	64
4.8	Si: Excitation energies	66
4.9	Fits and hypotheses: Si	66
4.10	Δ SCF excitation energies vs. LDA HOMO-LUMO gap	67
4.11	Excitation energies Ge	68
4.12	Excitation energies Ge and Si: Unrelaxed	68
4.13	Excitation energies Ge and Si: Relaxed	68
4.14	Exchange splitting: Si and Ge	70
4.15	Oscillator strengths and dielectric function	71
4.16	Level scheme in Si and Ge NCs	72
4.17	Radiative lifetimes Si	73
4.18	Radiative lifetimes Si	73
4.19	Radiative lifetimes Ge	73
4.20	Optical spectrum: Si	75
4.21	Optical spectrum: Ge	75
4.22	Absorption Ge: Comparison with experiment	75
4.23	Spectra and transition probabilities: nonsymmetric Ge and Si NCs	76
4.24	GeSi alloy NCs: interatomic distances	77
4.25	Excitation energies: Alloying	77
4.26	Lifetimes GeSi NCs	78
4.27	Spectra GeSi NCs	78
4.28	Band structure of Ge NC embedded in SiC	80
4.29	Band structure of Si NC embedded in SiC	80
4.30	Density of states for Ge NCs in cubic SiC	81
4.31	Dielectric function of Ge NCs embedded in cubic SiC	82
4.32	Dielectric function of Si NCs embedded in cubic Si	82
4.33	Contribution of the localized gap states	82
4.34	Density of states of Ge NCs embedded in hexagonal SiC	84
4.35	Dielectric function of Ge NCs embedded in hexagonal SiC	84
4.36	Oscillator strengths of Ge in cubic SiC for ideal and relaxed structure	84
4.37	Bond lengths after relaxation	85
4.38	Influence of relaxation on band structure: 41-atom Ge NC in SiC, 216-atom cell	85
4.39	Influence of relaxation on spectra: Ge in 3C-SiC	85
4.40	Pressure dependence of spectra: Ge NCs	86
4.41	Blow-up: Pressure dependence of spectra: Ge NCs	86
4.42	Pressure dependence of radiative lifetimes: Ge NCs	86

4.43 Pressure dependence: Bulk vs. NCs	87
4.44 Pressure dependence: Excitation energies of GeSi alloy NCs	87
4.45 Stokes shifts of Ge and Si NCs: T_d symmetry	88
4.46 Stokes shifts of Ge and Si NCs: Free symmetry	88

Chapter 1

Introduction

The prefix *nano-* has become one of the attention getters in the public and political perception of science. The background of the strong interest is the modification of many of the properties of any given material by the spatial confinement in nanostructures which enables many interesting and hitherto impossible applications. In many cases it is also possible to observe textbook-like effects in reality, like for instance two-dimensional confined electrons in a square-well potential created by thin layers of different materials.

On the other hand, many things are not easily understood. Especially the effect of spatial confinement on the electronic states of a system has been in the focus of investigation. Subsequently, the co-acting effects producing the overall behavior of a nanostructured system have become important. Among them are the interplay of alloying effects and confinement as well as of structural relaxation and the electronic states. Due to the complexity of the physical systems, a close connection between theory and experiment is needed in order to advance the physical understanding.

Two steps are necessary for the development of applications: First, an understanding of the relevant effects and the physics behind must be achieved, and a model must be developed, before second the effects can be functionalized effectively. The present work hopes to contribute to the understanding of the different mechanisms and effects prevailing in the experimental samples. We refrain from listing all the accomplished and the targeted applications ranging from sensors [1], optical devices like quantum-dot lasers or porous-Si diodes [1] to quantum-computing and bio-functionalized materials.

It is ambiguous to speak of “Si nanocrystals” without further specification. The reason is not so much a lack of good results or suitable models, but it is the diversity of structures that have been investigated experimentally. No one would be considered serious today who spoke of silicon surfaces without specifying the direction. Yet the present state of nanocrystal research is similar to this. Many different methods have been devised to create nanostructures, each of them resulting in a different structure with necessarily distinct properties: porous Silicon consists of Si NCs and filaments [1]; very small, nearly spherical Ge nanocrystals with diameters down to 0.9 nm can be created by radio frequency (rf) cosputtering of Ge and SiO₂ [2], as colloidal NCs [3, 4], or by ion implantation in SiC and subsequent annealing [5]. Ion beam cooling techniques with size selection lead to well-defined structures [6]. Larger NCs can be

made using molecular-beam epitaxy or related techniques where the transition to the Stranski-Krastanov growth mode [7] and possibly subsequent overgrowth creates NCs. Well oriented and arranged but large NCs are produced by lithographic methods. Differences in crystal structure, defects, surface termination or reconstruction result for different fabrication methods. Defects, non-radiative centers (dangling bonds), and the chemical variations influence the material's properties strongly. Nonetheless, most of the nanocrystalline material retains its tetrahedral coordination down to very small sizes [3], albeit possibly with modifications like stacking faults and faceting of the surfaces [5].

A discrepancy exists which, in general, is the following. Experimental work struggles to obtain very small, well-defined structures with a uniform size-distribution. Theoretical work or simulation, on the other hand, has a hard time describing the imperfections and the sample composition of entities of different type, surface reconstruction, etc. Especially the treatable size proves a challenge. When this work started, there was little overlap between the size ranges of experimental characterization and simulation. This has decisively changed; today this gap is about being closed.

Yet the present state of the field is characterized by serious uncertainties about the meaning of available experimental and theoretical results and especially of the connection between them. There is frequently speculation and over-interpretation of fortuitous coincidences. This complexity of the situation is also reflected in the diverse terminology. We have here adopted the view that a *nanocrystal* (NC) is a very small crystalline structure of a size intermediate between the quasi-molecular regime of *clusters* and the larger *quantum dots*.

The theoretical methods also differ for the different size ranges. For “very large” quantum dots (diameters of, say, 5 through 100 nm) barrier and transport effects are important, but there are no strong modifications due to spatial confinement. In this regime, the empirical-pseudopotential method [8] and the semi-empirical tight-binding approach [9] yield reliable results, while the present *ab initio* approach is incapable of dealing with the necessary number of atoms. It is also here where empirical and classical descriptions of the atomic interaction are used with a great deal of success for the determination of structural properties [10]. One disadvantage of the latter methods is that they do not provide an electronic structure. On the other end of the size range, very small NCs are well defined again, being molecules rather than crystallites. Here one can look at deeper physical problems like the description of excitations. For the smallest sizes, full *ab initio* structure optimization is possible, cf., for instance, Refs. [11–14]. However, both total-energy and kinetic effects contribute to a given experiment [15]. Moreover, not necessarily all the NCs of a sample contribute to a given measured quantity [6].

For the intermediate and larger crystallites, the structures are less well defined, and the modeling is necessarily different. The “educated guesses” for starting structures are either bulklike structures with modified surfaces, or could be amorphous or similar [15]. Recently it has been demonstrated that icosahedral structures can be energetically favorable [16]. It seems that in the future hybrid techniques are going to be used: Repeated melting and cooling in terms of molecular-dynamics schemes [17], possibly connected with thermodynamical considerations, will lead to better structures. Model building using neural-network and similar approaches

might also be promising. In any case, the future models of NCs or nanostructures in general will have to take into account the growth process.

Silicon accounts for the largest part of the total semiconductor production, and silicon technology is highly advanced compared to the fabrication techniques for most other materials. Germanium and silicon NCs are especially interesting in view of their potential for Si-based optoelectronics. The effects due to spatial quantization promise to overcome the limitations of these indirect-gap semiconductors for light-emission applications. This is very interesting from the technological point of view because the two group-IV materials can be easily integrated into existing Si technology. Promising results have been obtained. In fact, even optical gain has been achieved in Si nanocrystals [18].

Ge is chemically similar to Si. Moreover, both elements are miscible at arbitrary composition x . However, their bulk bandstructures are decisively different. In Ge the indirect gap is between Γ and L, and the direct gap Γ - Γ is very close in energy. In Si, the indirect gap is between Γ and a point along the Γ -X line, while the band separation at Γ is much larger. The electronic states in a NC are derived from those states represented by the bulk band structures. They are modified by the spatial confinement as well as by the inhomogeneous strain, as it develops in the NCs. This will influence their energetic position and their charge density distribution. Thus there is the open question as to what is the main contribution to the lowest unoccupied state in the Ge NCs, and if there are strong transitions at the bottom of the absorption spectrum. In the language of experiment: Are Ge NCs direct? or: Will the \mathbf{k} selection rule be broken such as to enable strong transitions?

The choice of the quantities of interest is determined in part by the potential applications, in part by the accessibility of the latter within the respective experimental and theoretical methods. This can be exemplified for the field most interesting to optical device applications: photoluminescence (PL). Excitation energies are especially interesting because their manipulation enables the controlled change of the emission wavelength of light-emitting devices. They are easily experimentally accessible. Moreover they present both challenge and promise for theory. The same problems as in the description of bulk spectra are found here [19], while the confinement causes further effects. This incites the work for further development of the theoretical description, at present primarily along the lines of the GW approximation and the Bethe-Salpeter equation (BSE). For photoluminescence the transition probabilities of the lowest transitions are also very important. Thus the excitation energies and the transition probabilities are two of the principal targets of the present work. A basic problem here is that – unlike in the bulk – there is no confirmed experimental accurate reference (except for well-defined molecules or molecule-like structures). On the other hand, time-resolved techniques yield useful information about the dynamics of the PL [20].

As most spectral optical properties (absorption/transmission, reflectivity, etc.) are directly connected with the dielectric function of the material, the latter quantity has been chosen, besides the energy and transition probability, as the key quantity to be investigated. The experimental characterization is usually done using techniques like ellipsometry or reflectance, absorption, or transmission spectroscopy [1, 21].

In addition, many other quantities are helpful for the understanding of the NC systems. For instance, the relaxation patterns and the bond lengths, as accessible for instance by means of Raman scattering [22] or transmission-electron microscopy [5], help in the discussion of the interdependencies between confinement and strain. Further techniques include scanning probe microscopy, and X-ray scattering. The Stokes shift, i.e., the red-shift of PL emission with respect to absorption, is an example of a quantity which at the same time is easily measurable and gives a great deal of information about the structural changes in the NCs upon excitation.

At the beginning of the present work, the majority of the existing theoretical calculations on Si nanocrystals was semiempirical [23–26], being based on the knowledge of the electronic structure of bulk silicon. However, the transferability of bulk electronic interaction parameters to a nanocrystalline environment cannot be assumed *a priori*. This holds for both the tight-binding approximation and the empirical-pseudopotential approaches. By now, calculations have also been performed using an *ab initio* technique based on density-functional theory (DFT) and the local density approximation (LDA) [27] or using time-dependent LDA [14]. Many-body effects like self-energy corrections and excitonic effects have also been taken into account [28, 29]. However, there is still a controversy about the correct treatment of the many-body effects in the calculation of the electron-hole pair excitation energies [30, 31]. Calculations of optical absorption spectra including many-body effects were rather rare and restricted to Si clusters with a small number of Si atoms [32]. Semiempirical tight-binding approaches [33, 34] allow the treatment of larger clusters. The maximum number of Si atoms handled in an empirical pseudopotential approach was much higher [8, 23]. Using *ab initio* pseudopotentials and a minimum sp^3 basis for the expansion of the wave functions, Noguez and Ulloa had [11] calculated absorption spectra for Si clusters of up to 70 atoms. On the other hand, optical characterizations had been done by reflectance and absorption spectroscopy in a wide frequency range of oxidized Si nanocrystallites [35] and Ge nanocrystals of varying size embedded in an insulating sapphire matrix [36–38]. Recent developments which have influenced the course of the present work will be briefly commented on in the Conclusions.

When this work started, the interest was mostly on a general description of the intrinsic properties of NCs. Therefore our starting point are free, hydrogen-terminated NCs as both a model of NCs embedded in a wide-gap semiconductor or insulator, and of really free NCs. This yields information about their intrinsic properties: What are the effects of confinement on Ge and Si? Well-suited simple structural models like ours have been used by many groups [14, 39]. They lead to important results and produced many starting points for ensuing work.

This thesis is located somewhere between physics and computational materials science, trying to draw information from, and to contribute to, both – the focus of the methods being on the first, the focus of the content being on the latter. The aim of the present work was to answer some of the important open questions of the time, which included in particular:

- Possibility of a change of Ge NCs to “direct” material suitable for luminescence applications? That is, the question if Ge NCs would be governed by quasi-direct contributions or by the indirect nature of Ge.
- Influence of the confinement on the higher spectral features;

- Refinement of the description of excitation energies beyond DFT-LDA energy differences; inclusion of electron-hole interaction and quasi-particle effects;
- Extension of the applicability of *ab initio* techniques of optical-spectra calculation to the treatment of NCs of intermediate size embedded in a crystalline matrix;
- Influence of the confining matrix on the structure and the properties of NCs;
- Influence of ionic relaxation for the modeling of NCs;
- Effect of spin-polarization on the excitation energies.
- Finally, in many cases explanations of experimental results have been possible after a theoretical understanding was achieved, as in the case of the composition dependence of the properties of GeSi alloy NCs.

In the course of the work, a number of additional points got into the focus of our investigation:

- The question about the mutual interdependence of alloying and confinement;
- Influence of pressure or compressive strain;
- Influence of electronic excitation and the resulting ionic relaxation, yielding the luminescence Stokes shift. Especially this quantity will probably remain amenable to fully quantum-mechanical methods only.

At the same time, it must be stressed that the field of NC or quantum dot physics is extremely diverse and not well separated from adjacent fields like quantum chemistry. For that reason a large number of effects has not been considered. These include in particular the questions of surface saturation which have since the beginning of the present work been found by other groups to change the optical properties of NCs very strongly [40–46]. Neither did we consider questions of non-linear response, the modeling of the growth processes, the phonon-assisted transitions in NCs, or in general temperature effects. Moreover, the discussion is focused exclusively on the group-IV materials Ge and Si, in a way disregarding the direct-gap materials like the popular CdSe [47]. A more comprehensive discussion can be found for instance in the reviews of Yoffe [47] or Zunger [8].

The following topics have been part of the work but are not described for lack of space due to the formal lengths restrictions: Effective-medium treatment of embedded NCs [48]; GW description of the electronic structure and the optical properties of embedded NCs [49]; Our recent attempts to establish a combined approach of classical relaxation of NCs and *ab initio* electronic-structure calculation [50]; Embedment of Ge in Si, and of GeC in SiC (unpublished).

The structure of the present work is as follows. After the discussion of the theoretical foundations in Chapter 2, Chapter 3 presents the details of the numerical treatment of our model systems. After that, we present in Chapter 4 the Results, along with a discussion of relevant experimental as well as other theoretical findings. Conclusion and Perspectives complete the thesis.

Chapter 2

Theoretical Foundations

2.1 Density-Functional Theory

2.1.1 The Hohenberg-Kohn Theorem

We assume that the Born-Oppenheimer separation of the electronic and the ionic degrees of freedom has been carried out [51, 52] and start from the non-relativistic time-independent Hamiltonian of the many-electron system

$$\hat{H} = \hat{T} + \hat{U} + \hat{W} \quad (2.1)$$

with the kinetic energy

$$\hat{T} = -\frac{\hbar^2}{2m} \sum_{\alpha} \int d^3\mathbf{r} \hat{\Psi}_{\alpha}^{\dagger}(\mathbf{r}) \nabla^2 \hat{\Psi}_{\alpha}(\mathbf{r}) \quad (2.2)$$

and the one-particle contribution

$$\hat{U} = \sum_{\alpha} \int d^3\mathbf{r} \hat{\Psi}_{\alpha}^{\dagger}(\mathbf{r}) v_{\text{ext}}(\mathbf{r}) \hat{\Psi}_{\alpha}(\mathbf{r}) - \mu_0 \sum_{\alpha\beta} \int d^3\mathbf{r} \hat{\Psi}_{\alpha}^{\dagger}(\mathbf{r}) \mathbf{B}_{\text{ext}}(\mathbf{r}) \cdot \vec{\sigma}_{\alpha\beta} \hat{\Psi}_{\beta}(\mathbf{r}) \quad (2.3)$$

due to a scalar external potential $v_{\text{ext}}(\mathbf{r})$ and an external magnetic field $\mathbf{B}_{\text{ext}}(\mathbf{r})$.¹ $\hat{\Psi}_{\alpha}^{\dagger}(\mathbf{r})$ is the field operator for spin α , which describes the creation of an electron at the point \mathbf{r} . The potential of the fixed ions is contained in $v_{\text{ext}}(\mathbf{r})$. \hat{W} is due to the longitudinal two-particle Coulomb interaction $w(\mathbf{r}, \mathbf{r}') = e^2/4\pi\epsilon_0|\mathbf{r} - \mathbf{r}'|$,

$$\hat{W} = \frac{1}{2} \sum_{\alpha\beta} \int d^3\mathbf{r} \int d^3\mathbf{r}' \hat{\Psi}_{\alpha}^{\dagger}(\mathbf{r}) \hat{\Psi}_{\beta}^{\dagger}(\mathbf{r}') w(\mathbf{r}, \mathbf{r}') \hat{\Psi}_{\beta}(\mathbf{r}') \hat{\Psi}_{\alpha}(\mathbf{r}). \quad (2.4)$$

¹For the present work we need to include spin polarization. In the presence of a magnetic field $\mathbf{B}(\mathbf{r})$, the magnetization is an independent variable. In the case of spin-polarization and zero magnetic field, however, the magnetization itself becomes a functional of the density; it is then no independent variable [53]. Nonetheless, the resulting spin-polarized formalism in the presence of zero magnetic field proves advantageous for the introduction of the local spin-density approximation, which is the reason why we introduce the magnetic field at this point. The introduction in this way treats the coupling of the magnetic field only with the electron spins, not however, with the orbital motion [53]. For the purpose of the present discussion this is sufficient.

In this Hamiltonian, spin-orbit as well as spin-spin coupling have been neglected. Basic to this approach are now the density operator

$$\hat{n}(\mathbf{r}) = \sum_{\alpha} \hat{\Psi}_{\alpha}^{\dagger}(\mathbf{r}) \hat{\Psi}_{\alpha}(\mathbf{r}) \quad (2.5)$$

and the magnetic moment density operator

$$\hat{\mathbf{m}}(\mathbf{r}) = -\mu_0 \sum_{\alpha\beta} \hat{\Psi}_{\alpha}^{\dagger}(\mathbf{r}) \vec{\sigma}_{\alpha\beta} \hat{\Psi}_{\beta}(\mathbf{r}) \quad (2.6)$$

with the vector of the Pauli matrices $\vec{\sigma}_{\alpha\beta}$. For the stationary eigen-states $|\Psi\rangle$ of the Hamiltonian (2.1) there is evidently a unique mapping

$$\mathcal{D} : \{|\Psi\rangle\} \rightarrow \{(n(\mathbf{r}), \mathbf{m}(\mathbf{r}))\}, \quad (2.7)$$

i.e., any non-degenerate ground state $|\Psi\rangle$ leads to a unique set of density and magnetization² ($n(\mathbf{r}) = \langle \Psi | \hat{n}(\mathbf{r}) | \Psi \rangle$, $\mathbf{m}(\mathbf{r}) = \langle \Psi | \hat{\mathbf{m}}(\mathbf{r}) | \Psi \rangle$). Considering two different ground-state expectation values $E_{\text{gs}} = \langle \Psi | \hat{H} | \Psi \rangle$ and $E'_{\text{gs}} = \langle \Psi' | \hat{H}' | \Psi' \rangle$, where \hat{H} differs from \hat{H}' only through $\hat{U}' \neq \hat{U}$, i.e., by different external potentials, one obtains by virtue of the Ritz principle

$$E_{\text{gs}} = \langle \Psi | \hat{H} | \Psi \rangle < \langle \Psi' | \hat{H} | \Psi' \rangle = \langle \Psi' | \hat{H}' - \hat{U}' + \hat{U} | \Psi' \rangle \quad (2.8)$$

and, likewise,

$$E'_{\text{gs}} = \langle \Psi' | \hat{H}' | \Psi' \rangle < \langle \Psi | \hat{H} - \hat{U} + \hat{U}' | \Psi \rangle. \quad (2.9)$$

Hence

$$E'_{\text{gs}} + E_{\text{gs}} < E_{\text{gs}} + E'_{\text{gs}} + \int d^3\mathbf{r} \left\{ n'(\mathbf{r}) (v_{\text{ext}}(\mathbf{r}) - v'_{\text{ext}}(\mathbf{r})) + n(\mathbf{r}) (v'_{\text{ext}}(\mathbf{r}) - v_{\text{ext}}(\mathbf{r})) \right. \\ \left. - \mathbf{m}'(\mathbf{r}) (\mathbf{B}_{\text{ext}}(\mathbf{r}) - \mathbf{B}'_{\text{ext}}(\mathbf{r})) - \mathbf{m}(\mathbf{r}) (\mathbf{B}'_{\text{ext}}(\mathbf{r}) - \mathbf{B}_{\text{ext}}(\mathbf{r})) \right\}. \quad (2.10)$$

The integral vanishes for $n(\mathbf{r}) = n'(\mathbf{r})$ and $\mathbf{m}(\mathbf{r}) = \mathbf{m}'(\mathbf{r})$, which turns eq. (2.10) into a contradiction. No two different non-degenerate ground states may lead to the same density and magnetization, the mapping \mathcal{D} is invertible. This is the Hohenberg-Kohn theorem for a spin-polarized system: Density and magnetization determine the ground state uniquely. Consequently, a ground-state total-energy functional (for the external fields v_{ext} and \mathbf{B}_{ext})

$$E_{v_{\text{ext}}, \mathbf{B}_{\text{ext}}} [n, \mathbf{m}] = F [n, \mathbf{m}] + \int d^3\mathbf{r} [v_{\text{ext}}(\mathbf{r})n(\mathbf{r}) - \mathbf{B}_{\text{ext}}(\mathbf{r}) \cdot \mathbf{m}(\mathbf{r})] \quad (2.11)$$

exists where

$$F [n, \mathbf{m}] = \langle \Psi [n, \mathbf{m}] | \hat{T} + \hat{W} | \Psi [n, \mathbf{m}] \rangle \quad (2.12)$$

²The densities are here assumed to be v -representable [53]. This is a restriction on the considered densities, but it is not relevant at the level of the present discussion. The restriction applies also to the density variations, cf. (2.28) below.

is a universal functional of n and \mathbf{m} , i.e., it does not depend on the external field. The argument as given so far is restricted to the ground state because the Ritz principle has been used. Another immediate consequence of eq. (2.8) is that the minimum of the functional $E_{v_{\text{ext}}, \mathbf{B}_{\text{ext}}}[n, \mathbf{m}]$ is attained for the ground state density and magnetization.

From now we treat the case of zero magnetic field. In the limit $\mathbf{B}_{\text{ext}} \rightarrow 0$ we have a purely scalar external potential and $\hat{V} = \sum_{\alpha} \int d^3\mathbf{r} \hat{\Psi}_{\alpha}^{\dagger}(\mathbf{r}) v_{\text{ext}}(\mathbf{r}) \hat{\Psi}_{\alpha}(\mathbf{r})$ instead of \hat{U} . Assuming the existence of a $\hat{V}' \neq \hat{V} + \text{const.}$ leading to the same ground state $|\Psi\rangle$ as \hat{V} , one arrives at an evident contradiction:

$$(\hat{T} + \hat{W} + \hat{V})|\Psi\rangle = E_{\text{gs}}|\Psi\rangle \quad (2.13)$$

and

$$(\hat{T} + \hat{W} + \hat{V}')|\Psi'\rangle = E'_{\text{gs}}|\Psi'\rangle \quad (2.14)$$

are inconsistent with the assumption of equal ground states, $\Psi = \Psi'$, because in that case adding eqs. (2.13) and (2.14) results in

$$(\hat{V} - \hat{V}') = E_{\text{gs}} - E'_{\text{gs}} = 0. \quad (2.15)$$

Thus also the mapping of the possible external potentials onto the ground states,

$$C : \{\hat{V}\} \rightarrow \{\Psi\} \quad (2.16)$$

is invertible.³ Thus, for a non-degenerate system with scalar external potential, the density determines both the ground state and the external potential uniquely, and vice versa.

The second statement of the Hohenberg-Kohn theorem is that the ground-state density may be determined by minimization of the functional $E_{v_{\text{ext}}, \mathbf{B}_{\text{ext}}}[n, \mathbf{m}]$. By virtue of the Ritz principle we have

$$E_{v_{\text{ext}}, \mathbf{B}_{\text{ext}}}[n_0, \mathbf{m}_0] < E_{v_{\text{ext}}, \mathbf{B}_{\text{ext}}}[n, \mathbf{m}] \quad \text{for any } n \neq n_0, \mathbf{m}(\mathbf{r}) \neq \mathbf{m}_0(\mathbf{r}). \quad (2.17)$$

Consequently, the ground-state energy is

$$E_0 = E_{v_{\text{ext}}, \mathbf{B}_{\text{ext}}}[n_0, \mathbf{m}_0] = \min_{n, \mathbf{m}} E_{v_{\text{ext}}, \mathbf{B}_{\text{ext}}}[n, \mathbf{m}]. \quad (2.18)$$

As mentioned before in footnote 1, the Hohenberg-Kohn theorem can be derived for the density alone. However, for the practical application, the present form is more convenient [53].

2.1.2 The Kohn-Sham scheme

We consider the case of zero external magnetic field. The Kohn-Sham (KS) formalism rests upon the central assumption that for any interacting N -particle system with ground-state density $n(\mathbf{r})$, a local single-particle potential $v_s(\mathbf{r})$ exists that results in the density $n_s(\mathbf{r})$ of non-interacting particles which is equal to $n(\mathbf{r})$,⁴ i.e.,

$$n_s(\mathbf{r}) = n(\mathbf{r}). \quad (2.19)$$

³Note that this is not necessarily true for $\mathbf{B} \neq 0$ [53].

⁴The validity of this assumption is discussed in detail in [53], as well as the question of v -representability of the densities.

For non-degenerate ground states, the lowest N single-particle eigenfunctions of the Schrödinger equation

$$\left(-\frac{\hbar}{2m}\nabla^2 + v_s^{(\alpha)}(\mathbf{r})\right)\phi_i^{(\alpha)}(\mathbf{r}) = \varepsilon_i^{(\alpha)}\phi_i^{(\alpha)}(\mathbf{r}) \quad (2.20)$$

provide a unique representation of the density,

$$n(\mathbf{r}) = \sum_{\alpha} \sum_{i=1}^{N_{\alpha}} |\phi_i^{(\alpha)}(\mathbf{r})|^2. \quad (2.21)$$

In order to obtain a practical scheme one has to determine the auxiliary potential v_s . The spin polarization is accommodated for by splitting the density into a spin-up and a spin-down density,

$$n_{(\alpha)}(\mathbf{r}) = \sum_{i=1}^{N_{\alpha}} |\phi_i^{(\alpha)}(\mathbf{r})|^2; \quad \alpha \in \{\uparrow, \downarrow\} \quad (2.22)$$

with $n(\mathbf{r}) = n_{\uparrow}(\mathbf{r}) + n_{\downarrow}(\mathbf{r})$ and $N = N_{\uparrow} + N_{\downarrow}$.

N_{\uparrow} and N_{\downarrow} are the number of spin-up and spin-down electrons, respectively. Both densities and, hence, the magnetization, are themselves functionals of the total density. This can be easily inferred from the fact that the argument of the Hohenberg-Kohn theorem remains valid if in eq. (2.10) the term containing the magnetization is omitted. Moreover, it should be noted that the introduction of a spin-up and a spin-down component distinguishes a certain direction along which the spin polarization is determined.

The non-interacting kinetic energy is a unique functional of the density as well, which follows from the Hohenberg-Kohn theorem: The argument in the previous chapter made no assumption about the interaction $w(\mathbf{r}, \mathbf{r}')$ of eq. (2.4) and is, therefore, also valid for the case $w(\mathbf{r}, \mathbf{r}') = 0$. Inserting the latter into eq. (2.12) shows that in this case

$$F[n, \mathbf{m}] = \langle \Psi[n, \mathbf{m}] | \hat{T} | \Psi[n, \mathbf{m}] \rangle = T_s[n, \mathbf{m}] \quad (2.23)$$

which implies that also T_s must be a functional of the density and magnetization,

$$T_s = \sum_{\alpha} \sum_{i=1}^{N_{\alpha}} \phi_i^{*(\alpha)}(\mathbf{r}) \left(-\frac{\hbar}{2m}\nabla^2\right) \phi_i^{(\alpha)}(\mathbf{r}) = T_s[n, \mathbf{m}]. \quad (2.24)$$

However, while the dependence of T_s on the ϕ_i is known, the functional dependence on $n(\mathbf{r})$ and $\mathbf{m}(\mathbf{r})$ is not. Note that in the interacting case the ground state cannot be represented by the lowest eigenstates of a single-particle equation. Rather it will contain contributions of Slater determinants involving higher eigenstates, if one wants to keep the idea of single-particle states at all. This is exploited in the “direct diagonalization” or configuration-interaction approach, cf. section 2.1.4 below. In particular, the kinetic energy of the interacting particles is different, $T_s[n] \neq T[n]$ [53].

The ground-state energy functional becomes

$$\begin{aligned} E_{v_{\text{ext}}} [n_{\uparrow}; n_{\downarrow}] &= F [n_{\uparrow}; n_{\downarrow}] + \int d^3 \mathbf{r} v_{\text{ext}}(\mathbf{r}) n(\mathbf{r}) \\ &= T_s [n_{\uparrow}; n_{\downarrow}] + \int d^3 \mathbf{r} v_{\text{ext}}(\mathbf{r}) n(\mathbf{r}) + \frac{1}{2} \int d^3 \mathbf{r} \int d^3 \mathbf{r}' n(\mathbf{r}) w(\mathbf{r}, \mathbf{r}') n(\mathbf{r}') + E_{\text{XC}} [n_{\uparrow}; n_{\downarrow}], \end{aligned} \quad (2.25)$$

where T_s is the kinetic energy of the non-interacting particles (depending only on n_{\uparrow} and n_{\downarrow} which are the same for the true and the auxiliary system) and the exchange-correlation functional

$$E_{\text{XC}} [n_{\uparrow}; n_{\downarrow}] = F [n_{\uparrow}; n_{\downarrow}] - T_s [n_{\uparrow}; n_{\downarrow}] - \frac{1}{2} \int d^3 \mathbf{r} \int d^3 \mathbf{r}' n(\mathbf{r}) w(\mathbf{r}, \mathbf{r}') n(\mathbf{r}'). \quad (2.26)$$

Variation with respect to n_{α} : $\alpha \in \{\uparrow, \downarrow\}$, i.e., calculation of the expression $\delta E_{v_{\text{ext}}}/\delta n(\mathbf{r})$ in compliance with the requirement that $n(\mathbf{r}) + \delta n(\mathbf{r})$ be v -representable [53], yields the auxiliary potential

$$v_s^{(\alpha)}(\mathbf{r}) = v_{\text{ext}}(\mathbf{r}) + \int d^3 \mathbf{r}' w(\mathbf{r}, \mathbf{r}') n(\mathbf{r}') + v_{\text{XC}}^{(\alpha)}(\mathbf{r}) \quad (2.27)$$

with

$$v_{\text{XC}}^{(\alpha)}(\mathbf{r}) = \frac{\delta E_{\text{XC}} [n_{\uparrow}; n_{\downarrow}]}{\delta n_{\alpha}(\mathbf{r})}. \quad (2.28)$$

Eqs. (2.20), (2.21) and (2.27) represent the Kohn-Sham scheme for a non-degenerate spin-polarized system. Spin enters the scheme only via $v_{\text{XC}}^{(\alpha)}(\mathbf{r})$, because the Hamiltonian eq. (2.1) does not couple the spatial and spin degrees of freedom.⁵

2.1.3 Transition to system without spin-polarization

The original Hohenberg-Kohn theorem and Kohn-Sham scheme have been given for a spinless system. This is recovered from the above equations by considering zero magnetization, i.e., only paired electrons and $n_{\uparrow}(\mathbf{r}) = n_{\downarrow}(\mathbf{r})$. From equation (2.28) it is evident that in this case $v_{\text{XC}}^{\uparrow}(\mathbf{r}) = v_{\text{XC}}^{\downarrow}(\mathbf{r})$. Hence $\phi_i^{\uparrow}(\mathbf{r}) = \phi_i^{\downarrow}(\mathbf{r})$ in eq. (2.20). The equations without spin-polarization are now obtained by representing the respective sums by factors of 2.

2.1.4 Physical interpretation by comparison to Hartree-Fock

The whole argument thus far does not contain any approximations beyond those contained in the initial Hamiltonian. It is instructive to compare the results with those of the Hartree-Fock approximation (HFA). Unlike in the HFA, due to the mapping of the interacting problem to a non-interacting auxiliary problem, the ground state density is exactly given by that of the

⁵This is similar to the Hartree-Fock approximation where the spin dependency rests in the exchange term. In the HFA the correlation is completely neglected.

auxiliary problem, albeit at the price of the unknown exchange-correlation potential. Approximations are entered only later, e.g., the local density approximation (LDA).

The HFA, by contrast, limits the space of wave functions from the beginning by restricting its ground states to being single Slater determinants of single-particle wave functions calculated for some effective potential of the other electrons.

Comparison of the Kohn-Sham ground-state energy functional eqs. (2.25) and (2.26), which can be written

$$E_{v_{\text{ext}}}[n_{\uparrow}; n_{\downarrow}] = T_s[n_{\uparrow}; n_{\downarrow}] + H[n] + E_{\text{XC}}[n_{\uparrow}; n_{\downarrow}] + \int d^3\mathbf{r} v_{\text{ext}}(\mathbf{r})n(\mathbf{r}), \quad (2.29)$$

with the Hartree term in eq. (2.25),

$$H[n] = \frac{1}{2} \int d^3\mathbf{r} \int d^3\mathbf{r}' n(\mathbf{r})w(\mathbf{r}, \mathbf{r}')n(\mathbf{r}'), \quad (2.30)$$

and the corresponding quantity of the Hartree-Fock scheme

$$E_{\text{HFA}} = T_s[\Psi^{\text{HFA}}] + H[n^{\text{HFA}}] + E_{\text{X}}[\Psi^{\text{HFA}}] + \int d^3\mathbf{r} v_{\text{ext}}(\mathbf{r})n^{\text{HFA}}(\mathbf{r}) \quad (2.31)$$

brings out two differences. E_{XC} contains the correlation which is missing in the HFA. Second, while the expression $T_s[\Psi^{\text{HFA}}]$ looks very similar to the kinetic energy of independent Kohn-Sham particles T_s as written in terms of the orbitals, cf. eq. (2.24), its meaning is different: Ψ^{HFA} is the ground state of *uncorrelated* electrons, unlike the true ground state whose density is represented by the Kohn-Sham orbitals according to eq. (2.21).

This is due to the fundamentally different approaches. Kohn-Sham stipulates that the ground state density be exactly represented and then constructs the necessary potentials, deferring the difficulty to the exchange-correlation potential v_{XC} . Hartree-Fock, on the other hand, first constructs the potential and then looks for the ground state in a subspace of the possible many-electron wave functions.

Under the assumption that the orbitals of the remaining electrons do not change when one electron is taken from (or added to) the system (i.e., in frozen-orbital approximation), the energy eigenvalues of the Hartree-Fock equations represent excitation energies. This is the content of Koopman's theorem.

The shortcomings of the HFA can, in principle, be remedied by application of the scheme not to a single Slater determinant of the lowest single-particle wave functions, but to the infinite sum over all such determinants, now including the higher single-particle states. This sum exhausts the Hilbert space of N -electron wave functions, which means that this so-called configuration interaction (CI) approach is exact. No approximation is done to the Hamiltonian in HFA.⁶ T_s becomes the kinetic energy of correlated particles, and $E_{\text{X}}[\Psi^{\text{HFA}}]$ is complemented by the correlation contribution. In this sense, correlation are those quantum effects which are not accounted for by the kinetic, the Hartree, and the exchange energies. In the Kohn-Sham approach, this corresponds to the definition of the exchange-correlation energy eq. (2.26) which is the difference between the full expectation value of the Hamiltonian and the non-interacting kinetic energy, the Hartree energy, and the contribution due to the external potential.

⁶This statement refers to the derivation of the Hartree-Fock equation using the full Hamiltonian and a Slater determinant for the wave function.

2.1.5 LDA and LSDA

In the Kohn-Sham scheme the many-electron system is described by a Schrödinger-like single-particle equation with a *local* potential. However, the difficulty of the initial many-electron problem has now been transferred to the task of finding the exchange-correlation part of this potential. Using the spin-polarization parameter

$$\zeta(\mathbf{r}) = \frac{n_{\uparrow}(\mathbf{r}) - n_{\downarrow}(\mathbf{r})}{n(\mathbf{r})}, \quad (2.32)$$

the exchange-correlation energy can in general be written as

$$E_{\text{XC}}[n_{\uparrow}; n_{\downarrow}] = \int d^3\mathbf{r} n(\mathbf{r}) e_{\text{XC}}([n; \zeta], \mathbf{r}) \quad (2.33)$$

with the exchange-correlation energy per particle e_{XC} . For the homogeneous electron gas, e_{XC} is only a function of the constant electron densities $n_{0\uparrow}$ and $n_{0\downarrow}$ or, alternatively, of n_0 and ζ_0 . The basic assumption of the L(S)DA is that for a system with a slowly varying density, replacement of e_{XC} by that of the homogeneous electron gas, $e_{\text{XC}}^{\text{hom}}$, for the given density and magnetization provides a reasonable approximation. In practice, the exchange-correlation energy per particle of the homogeneous electron gas $e_{\text{XC}}^{\text{hom}}$ is used in the replacement [54]

$$E_{\text{XC}}[n, \zeta] \approx E_{\text{XC}}^{\text{LDA}}[n, \zeta] := \int d^3\mathbf{r} n(\mathbf{r}) e_{\text{XC}}^{\text{hom}}(n_0, \zeta_0) \Big|_{n_0 \rightarrow n(\mathbf{r}), \zeta_0 \rightarrow \zeta(\mathbf{r})}. \quad (2.34)$$

The exchange-correlation potential of the Kohn-Sham scheme eq. (2.28) is then given by the respective functional derivatives with respect to $n_{\downarrow}(\mathbf{r})$ and $n_{\uparrow}(\mathbf{r})$,

$$v_{\text{XC}}^{\uparrow\downarrow}(\mathbf{r}) \approx \frac{\partial}{\partial n_{\uparrow\downarrow}(\mathbf{r})} \left\{ n(\mathbf{r}) e_{\text{XC}}^{\text{hom}}(n(\mathbf{r}), \zeta(\mathbf{r})) \right\} := v_{\text{XC}}^{\uparrow\downarrow \text{LSDA}}(n(\mathbf{r}), \zeta(\mathbf{r})). \quad (2.35)$$

The exchange-correlation energy is mostly interpolated between the paramagnetic ($\zeta = 0$) and the saturated ferromagnetic ($\zeta = 1$) case according to the “standard interpolation” due to von Barth and Hedin [55]. For the density dependence of these two cases, the interpolation of Perdew and Zunger [56] of the Monte-Carlo results of Ceperley and Alder [57] is used in the present work. Evidently, the LDA, for non-spin-polarized systems, follows simply for $\zeta = 0$.

Surprisingly, the L(S)DA turned out to work much better than expected even for systems with strongly varying densities, be it solids, molecules, or even atoms. The reasons for this success lie probably in the correct representation of the spherically averaged exchange-correlation hole, and in a subtle cancellation of errors [53]. Note that the L(S)DA does not, as sometimes wrongly stated, consist in neglecting correlation.

2.1.6 Forces in DFT

For molecular dynamics calculations and relaxations one needs to calculate the forces acting on the ionic cores of the system. Neglecting electron-phonon interactions as well as the vibrational

energy of the lattice of ions at the positions \mathbf{R}_s with charges Z_s , one can write the total energy of the system as

$$E_{\text{tot}} = \frac{1}{2} \sum'_{s,s'} v(\mathbf{R}_s - \mathbf{R}'_{s'}) + E_{v_{\text{ext}}} [n_{\uparrow}, n_{\downarrow}] \quad (2.36)$$

where the first term is the classical ion-ion interaction energy (which makes sense since after introducing the Born-Oppenheimer approximation the fixed cores are described classically) and the electronic term depends implicitly on the \mathbf{R}_s via $v_{\text{ext}} = v_{\text{ext}}(\{\mathbf{R}_s\})$. The forces on the individual nuclei s are found as the derivatives of the energy with respect to the ionic coordinates R_s ,

$$\mathbf{F}_s = -\nabla_{\mathbf{R}_s} E_{\text{tot}} = e^2 \sum'_{s,s'} Z_s Z_{s'} \frac{\mathbf{R}_s - \mathbf{R}_{s'}}{|\mathbf{R}_s - \mathbf{R}_{s'}|^3} - \int d^3 \mathbf{r} [\nabla_{\mathbf{R}_s} v_{\text{ext}}(\mathbf{r})] n(\mathbf{r}). \quad (2.37)$$

They are called the Hellmann-Feynman forces [58,59] and correspond to the force on a nucleus due to the classical electrostatic potential of the other nuclei and the electrons [59]. In eq. (2.37) an additional term of variational forces has been omitted. These are zero in the ground state [60].

By means of the forces of eq. (2.37), molecular-dynamics calculations or relaxations of the ionic positions can be carried out according to a number of different algorithms [61]. One can also, unlike in the present work, minimize the electronic and ionic degrees of freedom simultaneously [62].

2.2 Excitation Energies

2.2.1 Quasiparticles

We are primarily interested in optical properties. Any optical process such as absorption or radiative recombination involves excited states. Hence it is necessary to consider in detail the relation between the ground-state theory and the excited states.

The text-book-like Schrödinger equation of one particle in a fixed external potential gives energy values which do not depend on whether or not the respective state is occupied. If the same were the case for an electron in the solid, a discussion of different band structures would not be necessary and optical calculations would be easy. However, in the solid the electron of the independent-particle approach is subjected to the effective field of the other particles which is not independent of the electron under question itself. If the respective electron is excited (or, which for this discussion is equivalent, removed, which means that a hole is created), the other electrons will rearrange according to the many-particle Schrödinger equation (2.1) whose self-consistent potential contains the wave function of the excited electron. Consequently, the energy values which can be assumed by the excited electron are different from the values calculated for the unoccupied states using the ground-state charge density in the self-consistent potential of the still exact one-particle description as given by the Kohn-Sham scheme. Moreover, the Kohn-Sham, i.e., local, description of the exchange contribution can only be correct for a single state

(HOMO). Thus one is lead naturally to the concept of quasiparticles representing one electron (or hole) “dressed” by the reaction of the rest of the system [63, 64].

In addition, if both an electron and a hole are present in the system, they must be described simultaneously in order to account fully for their interaction. A one-particle approximation cannot, therefore, provide a complete description of the excited system.

In the one-particle description one asks at what possible energies a particle can be added or removed from the system. These are the energies of the so-called quasiparticles of the system which are described by the Schrödinger-like quasiparticle equation containing the non-local energy-dependent self-energy in lieu of the exchange-correlation potential of the Kohn-Sham scheme. It is the quasiparticle band structure one is generally interested in (as opposed to, e.g., the LDA band structure). The addition and removal energies can be measured by photoemission and inverse photoemission, respectively [19]. These processes leave a charged system behind; the number of electrons changes.

Absorption processes and, likewise, the subsequent luminescence are different in that they do not change the number N of electrons in the system. The inferred continuum edge of the optical spectrum is taken as the difference between quasiparticle energies of the conduction and the valence bands or, more strictly speaking, as the difference between ionization energy and electron affinity [65–68]. Hence this so-called quasiparticle gap involves excitations and is not directly amenable to the ground-state theory DFT. Thus it is necessarily different from the gap of even the exact-DFT band structure.

Any DFT band structure is calculated for a fixed particle number. However, the exchange-correlation potential eq. (2.28) has been shown to exhibit a discontinuity when the number of electrons is changed [65, 68, 69]. The role of this can be understood from Fig. 2.1 which has been reproduced from Ref. [65]. The measured quasiparticle gap is the difference between the LUMO (lowest unoccupied molecular orbital) energy of the $(N + 1)$ -electron system and the VB edge of the N -electron system. The quasiparticle gap E_g^{QP} differs from the DFT-KS gap by the discontinuity $\Delta = v_{\text{XC}}^{(N+1)}(\mathbf{r}) - v_{\text{XC}}^{(N)}(\mathbf{r})$ (independent of \mathbf{r}) [65] with the exchange-correlation potential of the N - and the $(N + 1)$ -electron system. Hence the “LDA band-gap underestimate” is a misnomer and not giving due consideration to the two different effects; the first being the general need of an excited-state description, the second being the error incurred by the local approximation of the v_{XC} for fixed particle number. However, the relative importance of these two effects is not immediately obvious. Godby *et al.* [65] showed for a bulk semiconductor that about 80% of the “LDA gap error” is in fact due to the missing discontinuity in the exchange-correlation potential and therefore inherent in any DFT calculation for fixed particle number. Only the rest is due to the representation of v_{XC} by its counterpart of the homogeneous electron gas. For this reason we distinguish here the superscripts LDA and DFT.

This means that any DFT band structure that is calculated for constant particle number will suffer a serious gap underestimate, no matter which approximation of V_{XC} is used. This is a serious problem not only from the fundamental point of view but also qualitatively: The DFT-LDA band gap of silicon is about 50% too small, the band gap of germanium is even 0 – the valence and conduction bands overlap.

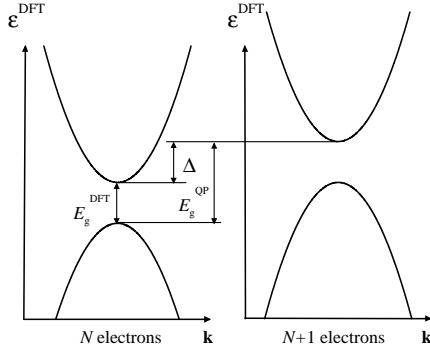


Figure 2.1 Schematic DFT band structure for an N -electron system and an $N+1$ -electron system [65]. Indicated are the DFT gap E_g^{DFT} , the quasiparticle gap E_g^{QP} , and the self-energy correction Δ .

In the following we give a brief account of the different approaches to excitation energies and locate the method used in the current work among them.

2.2.2 Self-energy corrections

As mentioned before, the Kohn-Sham scheme Eqs. (2.20), (2.21) and (2.27), provides the exact ground-state density and total energy. The Kohn-Sham eigenvalues ε_i are not, however, *a priori* endowed with physical meaning as excitation energies. Nonetheless, comparison with the quasiparticle equation (Dyson equation) derived from Green's functions theory [70],

$$\left[-\frac{\hbar^2}{2m}\Delta_{\mathbf{r}} + v_{\text{ext}}(\mathbf{r}) + v_H(\mathbf{r})\right]\phi_i^{\text{QP}}(\mathbf{r}) + \int d\mathbf{r}' \Sigma_{\text{XC}}(\mathbf{r}, \mathbf{r}', \varepsilon_i)\phi_i^{\text{QP}}(\mathbf{r}') = \varepsilon_i\phi_i^{\text{QP}}(\mathbf{r}) \quad (2.38)$$

where the ε_i are really single-(quasi-)particle excitation energies and i includes the spin index, shows a close formal similarity between the two equations. The only difference is that the (unknown) local exchange-correlation potential $v_{\text{XC}}^{(a)}(\mathbf{r})$ of the Kohn-Sham scheme is replaced by its counterpart in the quasiparticle equation (2.38), the non-hermitian, non-local, energy-dependent self-energy integral operator Σ_{XC} . This similarity itself should be viewed as an indication that the Kohn-Sham scheme, despite its lack of formal justification as a description of excitation energies, and in spite of the problems discussed above, bears at least some merit for the description of excitations. In fact, the KS energies have been shown to be well-defined approximations to the excitation energies [71].

This is exploited in the approach of self-energy corrections. It consists in considering KS as a zeroth approximation to be corrected by a self-energy correction,

$$\delta\Sigma(\mathbf{r}, \mathbf{r}', \varepsilon_i) = \Sigma_{\text{xc}}(\mathbf{r}, \mathbf{r}', \varepsilon_i) - v_{\text{xc}}(\mathbf{r})\delta(\mathbf{r} - \mathbf{r}') \quad (2.39)$$

which can be formally defined from the difference of the KS and the Dyson equations. One possible approach is Hedin's GW approximation [19, 70] which approximates the self-energy operator as the product of the Green's function G and the screened Coulomb interaction W , i.e., $\Sigma_{\text{xc}}^{\text{GW}} = G \cdot W$. If then the LDA exchange-correlation potential is used in the KS equation, $v_{\text{xc}}(\mathbf{r}) = v_{\text{xc}}^{\text{LDA}}(\mathbf{r})$, the self-energy correction is given as [72]

$$\delta\Sigma(\mathbf{r}, \mathbf{r}', \omega) = \frac{i}{2\pi} \int e^{i\delta\omega'} G(\mathbf{r}, \mathbf{r}', \omega') \cdot W(\mathbf{r}, \mathbf{r}', \omega - \omega') d\omega' - v_{\text{xc}}^{\text{LDA}}(\mathbf{r})\delta(\mathbf{r} - \mathbf{r}'). \quad (2.40)$$

As the DFT-LDA eigenfunctions are fairly close to the GW wave functions [19], $\delta\Sigma$ can be considered as a perturbation. This form of the self-energy approach is, therefore, a perturbative approach. One calculates shifts for the band edges $\Delta_{\text{HOMO}} = \langle \text{HOMO} | \delta\Sigma | \text{HOMO} \rangle$ and $\Delta_{\text{LUMO}} = \langle \text{LUMO} | \delta\Sigma | \text{LUMO} \rangle$ with respect to the corresponding DFT values [73]. The gap correction to the LDA gap E_g^{LDA} is then given by $\Delta = \Delta_{\text{LUMO}} - \Delta_{\text{HOMO}}$.

One can now calculate corrections iteratively. In a first step, the KS wave functions $\{\phi^{\text{LDA}}\}$ are kept, and the energy correction is calculated [19]. This is, at present, the customary thing to do. In a second step, the wave functions can be updated [32, 74]. The method yields single-quasiparticle energies and gaps E_g^{QP} . These quasiparticle energies reflect the insertion of one electron (or hole) in the system. In physical terms, when the additional electron is put into the LUMO state, the corresponding energy is the electron affinity $A = E_N - E_{N+1}$. Likewise, when an electron is removed from the HOMO, the ionization energy $I = E_{N-1} - E_N$ is obtained. E_N is the energy of the N -electron system, $E_{N\pm 1}$ is the energy of the negatively/positively charged system.

The quasiparticle gap of the system is given by the difference of I and A [68],

$$E_g^{\text{QP}} = I - A \quad (2.41)$$

and can thus be measured by combining photoemission and inverse-photoemission experiments. With respect to this QP gap, the optical (or: “excitonic”) gap, i.e., the gap as measured in an optical absorption experiment, is reduced by the electron-hole Coulomb interaction $E_{\text{e-h}}$,

$$E_g^{\text{opt}} = E_g^{\text{QP}} - E_{\text{e-h}}. \quad (2.42)$$

Using LDA we have E_g^{LDA} instead of E_g^{DFT} . The quasiparticle gap becomes

$$E_g^{\text{QP}} = E_g^{\text{LDA}} + \Delta \quad (2.43)$$

with a QP gap correction $\Delta = \Delta_{\text{LUMO}} - \Delta_{\text{HOMO}}$ [73] and, consequently, the optical gap

$$E_g^{\text{opt}} = E_g^{\text{LDA}} + \Delta - E_{\text{e-h}}. \quad (2.44)$$

In this equation, E_g^{opt} and $E_{\text{e-h}}$ are physical quantities independent of the nature of any approximation, unlike E_g^{LDA} . For that reason, Δ , cf. eq. (2.39), is also defined relative to the LDA and should, strictly speaking, also be superscripted by “LDA”. This is not, however, commonly done.

In order to correctly account for the electron-hole interaction, one has to go to a two-particle description and describe the simultaneous presence of electron and hole. This can be done by simultaneous solution of BSE and Dyson equation which follow from Green’s functions theory. However, this requires high numerical efforts [19]. Therefore, an alternative approach has been pursued in the present work [75], which will be discussed in the following section.

The independent calculation of the quasiparticle correction and the $E_{\text{e-h}}$ enables a comparison in the case of NCs, which has been carried out by Delerue *et al.* [29] using a combined approach of tight-binding wave functions, model screening, and BSE. While compensation effects have been known before [19, 76], they found that over a wide size range of Si nanocrystals

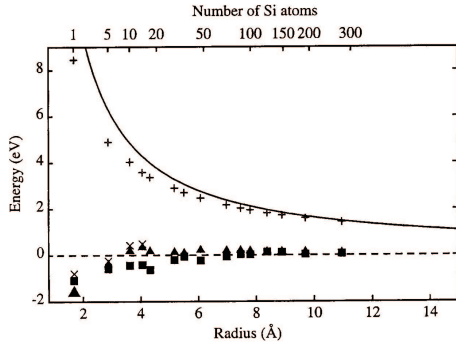


Figure 2.2 Exciton Coulomb energy $E_{e-h} = E_g^{\text{opt}} - E_g^{\text{QP}}$ [29] versus size in Si nanocrystals (Plus: full GW + Bethe-Salpeter calculation; continuous line: classical electrostatics calculation with effective-mass wave functions). Difference between the self-energy correction $\Delta - \Delta_{\text{bulk}}$ and E_{e-h} (squares: Delerue *et al.*, full tight binding [29]; triangle up: Delerue *et al.*, LDA approximation of v_{XC} , cf. Ref. [29]; x: *ab initio* results of Ref. [32]). The figure has been reproduced from Ref. [29].

the Coulomb energy and the self-energy correction cancel up to a constant which Delerue *et al.* suggest to represent the bulk self-energy correction,

$$\Delta - E_{e-h} \approx \text{const.} \stackrel{?}{=} \Delta_{\text{bulk}}. \quad (2.45)$$

The “constant” (or, better: weakly R -dependent contribution) will be discussed in more detail below in section 2.2.3.2

From this finding it can be concluded that *in this size regime* of NCs the LDA eigenvalues present very reasonable approximate excitation energies. In particular their R -dependence reproduces the exact values very well,

$$E_g^{\text{opt}}(R) = E_g^{\text{LDA}}(R) + \text{const.} \quad (2.46)$$

This fortuitous fact calls for an explanation. The physical reason for the cancellation over a wide size range can be understood, at least qualitatively, when eq. (2.42) is rewritten with the NC radius as a parameter,

$$E_g^{\text{opt}}(R) = E_g^{\text{LDA}}(R) + \Delta(R) - E_{e-h}(R). \quad (2.47)$$

It has been shown for the GW approximation of the self-energy that in the limit of strong localization but radii larger than the screening length given by the inverse Thomas-Fermi wave vector, for both the electron and the hole the R -dependent part of the quasiparticle correction goes like $1/\varepsilon_{\text{eff}}R$ [73],

$$\delta\Sigma(R) \propto \frac{e^2}{\varepsilon_{\text{eff}}R}. \quad (2.48)$$

This is the same R -dependence as that of the Coulomb contribution,

$$E_{\text{coul}}(R) \propto \frac{e^2}{\varepsilon_{\text{eff}}R} \quad (2.49)$$

Here the radius of the NC is taken as the localization radius of the respective wave functions. The screening constant ε_{eff} is, of course, also R -dependent, but this cancels out as far as eqs. (2.48) and (2.49) are concerned. This means that the cancellation over a wide range of sizes is explicable in term of the size dependence of the different quantities.

The expression (2.48) does not yield the correct bulk limit Δ_{bulk} for $R \rightarrow \infty$ where it vanishes. For large radii, Δ must go over into Δ_{bulk} . This will be discussed below. Moreover, the Coulomb energy eq. (2.49) is also given only for NC radii smaller than the localization radius of the free exciton in the respective material. If larger NCs are considered, the NC radius loses its meaning for the localization of the electron and hole wave functions.

2.2.3 Excitation energies from total energies

2.2.3.1 Conventional Δ SCF method: $E_g^{\text{QP}} = I - A$

Alternatively to the self-energy approach, there is the conceptionally much simpler so-called Δ SCF approach which uses the total energies of different Self-Consistent Field calculations, as for instance in DFT or HFA. In this approach, the quasiparticle gap as defined in terms of ionization energy I and electron affinity A in eq. (2.41) [66, 67, 69, 77] is used,

$$\begin{aligned} E_g^{\text{QP}} &= I - A \\ &= E_{N-1} + E_{N+1} - 2E_N \end{aligned} \quad (2.50)$$

where E_N signifies the total energy of the system with N electrons (i.e., the ground state), and $E_{N\pm 1}$ signifies the total energy of the positively/negatively charged system. One problem of this approach is that the electron and the hole of the excitation are never simultaneously present in the NC. In order to obtain the optical gap, $E_{\text{e-h}}$ has to be inserted by hand: This has been done by Ögüt, Chelikowsky, and Louie [28] using

$$E_g^{\text{opt}} = E_{N-1} + E_{N+1} - 2E_N - \int \frac{|\psi_e(\mathbf{r}_1)|^2 |\psi_h(\mathbf{r}_2)|^2}{\varepsilon(\mathbf{r}_1, \mathbf{r}_2) |\mathbf{r}_1 - \mathbf{r}_2|} d\mathbf{r}_1 d\mathbf{r}_2. \quad (2.51)$$

For E_{coul} they used the intuitive expression under the integral to approximately calculate the electron-hole interaction energy $E_{\text{e-h}}$. $\psi_h(\mathbf{r}_2)$ and $\psi_e(\mathbf{r}_1)$ are here the HOMO and the LUMO state of the $N - 1$ and the $N + 1$ -system, respectively.

2.2.3.2 Discussion of the Δ SCF method $E_g^{\text{QP}} = I - A$

Equation (2.50) has been given in the original publication of Sham and Schlüter for electron numbers in the limit of $N \rightarrow \infty$ [68]. This limitation is not mentioned by Ögüt *et al.* [28]. However, one could still take eq. (2.50) as the definition of the respective energies. From the quasiparticle energies, Ögüt *et al.* calculate the optical gap simply by means of eq. (2.42), with the Coulomb energy calculated as in eq. (2.51).

However, this is only an approximation for optical absorption energies, i.e., energies of neutral excitations. In those, the electron and the hole occur simultaneously in the system. The remaining $N - 1$ electrons will rearrange according to the excitation, i.e., in the approximation of the excitation of Ögüt *et al.* according to the $N - 1$ and the $N + 1$ system. After an absorption, however, they react according to the presence of the electron-hole pair. As the effect of the electron and of the hole on the remaining electrons will tend to cancel in a zeroth approximation [19], the calculated optical gaps of Ögüt *et al.* will be overestimated.

This can also be expressed in the following sense: The Δ SCF method of Ögüt *et al.* starts from the LDA wave functions of the $N - 1$ - and the $N + 1$ -electron system and calculates, as an approximation, an energy correction according to eq. (2.51). But it does not allow for a mixing of electron and hole states due to the electron-hole interaction. However, such a mixing has been found to be important [32].

The QP gap E_g^{QP} as calculated by means of eq. (2.50) is known to reduce to the DFT (LDA, if LDA is used) gap in the bulk. As for the additional contribution to be added to the self-energy corrections as calculated by means of the Δ SCF method eq. (2.51), conflicting views have been expressed in the literature [28, 30, 31, 78, 79].

Godby and White commented [30] the following on the paper by Ögüt *et al.* [28]: The Δ SCF method of Ögüt *et al.* (which they term “ Δ LDA”) includes electrostatic relaxation effect and the corresponding relaxation in the LDA exchange-correlation potential. Both go to zero for large sizes, where the QP gap of in LDA reduces to the LDA gap [68, 69]. Here, the non-zero band-gap correction can be calculated using many-body perturbation theory in a suitable approximation. It is not reproduced by the LDA, in particular due to the missing discontinuity with changing electron number. Godby and White suggest that there is no reason to assume that the contribution of the latter will be negligible in the smaller clusters, and they claim that an extra contribution should be added to the optical gaps calculated by Ögüt *et al.* which corresponds roughly to the bulk self-energy correction. They support their claim by a fit of the calculated self-energy correction from Ögüt *et al.* [30].

Ögüt *et al.* answer [79] that the extrapolation from the crystallite size regime to the bulk is not feasible. This seems to be a valid criticism, in particular because the confinement mechanism changes when the NC radius is of the order of the free-exciton radius. Ögüt *et al.* use comparison to experiment [80] to show that this extra contribution would not have to be added. However, the agreement with experiment could also be due to a cancellation of the following two effects:

- The overestimate of their optical gap as discussed above; and
- the missing extra contribution as discussed by Godby and White.

What Ögüt *et al.* appear to have called the QP gap in the reply [79] to Godby and White, is in fact the ionization potential of SiH_4 [80] (cf. p. 4869). Moreover, this is only cited from an older paper, Pullen *et al.* [81]. If this is really what has been done, it would imply that the electron affinity is zero. However, we found that for instance for Si_5H_{12} , there is no bound LUMO state.⁷ This will be similar for SiH_4 and Si_2H_6 . It is, therefore, unlikely that the description by Ögüt *et al.* using LDA total energies will yield valid results for the affinity and, therefore, E_g^{QP} according to eq. (2.50). Moreover, given the fact that there are two experimental values for the ionization potential of Si_2H_6 , viz. 10.4 and 10.8 eV [80], it is apparent that the error bar of

⁷In LDA the LUMO is localized for the N -electron system, but if we calculate the system for $(N+1)$ electrons, the additional electron is not localized at the cluster [82]. Rinke *et al.* [83] calculated the energies for Si_5H_{12} in LDA and GW and found that in LDA there is a bound LUMO state, while with quasi-particle effects in GW the LUMO lies above the vacuum level.

these measurements is fairly large, and that probably the accuracy is not really sufficient to draw the conclusion they draw in the reply: That there is no additional contribution to their values to be added. The latter is even more serious as there are different experimental values of the ionization potential of 11.00 eV for SiH₄ and 9.74 eV for Si₂H₆ [84]. The conclusion of these points is that the refutation of the criticism of Godby and White is not necessarily stringent.

A second indication of the same point is the following: In their reply to the comment of Franceschetti, Wang, and Zunger [31], Ögüt *et al.* assume for a counterfactual argument that the additional contribution of roughly 0.68 eV (corresponding to Δ_{bulk}) would have to be added. From that they derive that the effective dielectric constants of dots between 2.3 and 3 nm diameter would have to be around 1.5, which they call *unrealistic*. However, this is roughly the value that they calculate in a newer publication [85] (without, however, mention of this contradiction.) Thus this argument is, in fact, another indication that the extra contribution should be added.

The third indication would be that the TB BSE result of Delerue *et al.* [29] shows a cancellation between the self-energy effects minus the bulk self-energy correction and the exciton Coulomb energy, $(\Delta - \Delta_{\text{bulk}}) - E_{\text{e-h}} \approx 0$. While it is not clear how well the TB description reproduces the effects, this also suggests the adding of a “constant.” For very small sizes, $(\Delta - \Delta_{\text{bulk}}) - E_{\text{e-h}} \approx 0$ becomes smaller than zero, which is consistent with the fact that Preuß *et al.* [86] found good agreement between vertical ionization energies and LDA eigenvalues for molecules, and on the other hand requiring to add the “constant” for intermediate sizes and in the bulk limit.

Finally, comparison of our excitation energies eq. (2.55) with the experimental results [75] would not be incompatible with an added approximately .6 eV, especially if the extra contribution would be smaller for smaller sizes. This will be discussed below on page 66.

In general, the main drawbacks of the Δ SCF method eq. (2.51) are that

- The method is inherently focused on single-particle excitations. Therefore it misses the electronic reaction to the simultaneous presence of electron and hole, or, in other words, the mixing of states due to the electron-hole interaction apart from the approximate treatment of the electron-hole interaction using the Coulomb integral in eq. (2.51).
- It requires three self-consistent calculations, unlike the method described below which needs only two.
- The system is charged, which necessitates a compensation charge when a supercell geometry is used; connected with this, convergence with respect to cell size is expected to be slower than for neutral crystallites [82].
- The negatively charged cluster may not have a bound LUMO state, as for instance in the case of Si₅H₁₂ [82, 83]. Spurious localization of the electron due to the fact that the LDA brings the LUMO – wrongly – below the vacuum level may compromise the validity of the method, although error cancellation appears possible. The localization due to DFT-LDA might mimic the localization due to the presence of the hole.
- The evaluation of the Coulomb energy E_{coul} remains intricate.

2.2.3.3 Δ SCF with occupation constraint

The approach employed in the present work is different. It goes beyond the single-particle description and targets directly the pair excitation. We use the Δ SCF method with occupation constraints which effectively introduce an electron-hole pair into the NC [87, 88].

Due to the use of the Ritz principle, the DFT/Kohn-Sham formalism provides only a description of the ground states. However, as shown by Perdew and Levy [89], all the extrema of the ground-state (!) functional $E_{v_{\text{ext}}}$ of eq. (2.25), i.e., the solutions of the Euler-Lagrange equation

$$\frac{\delta E_{v_{\text{ext}}}}{\delta n(\mathbf{r})} = \lambda \quad (2.52)$$

represent the density and the energy of a stationary state⁸. One way of finding these excited states is to specify occupation numbers accordingly. In the Kohn-Sham scheme, these enter only into the density, eq. (2.21), which is now modified to

$$n(\mathbf{r}) = \sum_{\alpha \in \{\uparrow, \downarrow\}} \sum_{i=1}^{N_\alpha} \gamma_i^{(\alpha)} |\phi_i^{(\alpha)}(\mathbf{r})|^2 \quad (2.53)$$

with occupation numbers $\gamma_i^{(\alpha)} \in \{0, 1\}$. Eqs. (2.20), (2.53) and (2.27) are formally identical to the original Kohn-Sham scheme. They can be used for a non-degenerate spin-polarized system with prescribed occupation numbers. Obviously, for

$$\gamma_i^{(\alpha)} = 1 : i \leq N_\alpha \quad (2.54)$$

the ground-state equations are recovered. An electron-hole excitation can be described by “un-occupying” one of the occupied states by choosing $\gamma_j^{(\alpha)} = 0$ and inserting the electron into one of the higher states, $\gamma_k^{(\beta)} = 1$. It should be noted that at this point the total magnetization is now no independent variable, but is specified by the fixed numbers of spin-up and spin-down electrons, see also section 2.2.5. However, the LSDA is not able to describe pure multiplets, cf. section 2.2.5 below.

In our calculation of the lowest pair excitation energies, the occupation constraint stipulates: HOMO \rightarrow empty; LUMO $\rightarrow e^-$. E_N^{e+h} is now the excited-state total energy of the N -electron system. This quantity includes the Hartree relaxation of the electronic system when the electron-hole pair is present, and it also includes the electron-hole Coulomb interaction⁹. Correlation

⁸These stationary states provide a subset of the excited states of the system [89].

⁹A practical remark is in order. While the Coulombic electron-hole interaction is, in fact, accounted for in a confined system, the situation in bulk calculations is different. Usually the primitive cell (or a different relatively small cell, compared to the localization radius of the exciton) is used which by its boundary conditions makes a description of excitons impossible: Electron and hole are forced to be distributed throughout the crystal. In other words, the method as described by (2.50) will work only when the principal influence on the distribution of the wave functions is the confinement – unlike in the bulk, where a localization in terms of $(\mathbf{r}_{\text{el}} - \mathbf{r}_{\text{h}})$ is brought about mainly by the Coulomb interaction and correlation. In this case, the singly ionized systems’ wave functions are drastically different from those of the electron-hole pair [90].

effects far beyond the frozen-orbital approximation are taken into account by performing the self-consistent calculation of the N -electron system with the electron-hole pair present. The pair excitation energy is now simply its difference to the ground-state total energy,

$$E_g^{\text{opt}} = E_N^{\text{e+h}} - E_N. \quad (2.55)$$

There are advantages of this approach over the “conventional” Δ SCF method of eqs. (2.50) and (2.51) described in the previous section. First of all, only two self-consistent calculations are necessary. Moreover, the Coulomb energy does not have to be calculated after the calculation but is naturally included. This alleviates also the problem of unbound LUMO states, because the electron-hole pair is bound much stronger due to the attractive Coulomb interaction. Both methods describe a pair excitation, but in the first method the electron-hole interaction is only partially introduced via the Coulomb integral of equation (2.51). Only for that reason is it possible to write the pair-excitation energy as the sum of two one-particle excitation energies I and A . Due to the numerous advantages, eq. (2.55) is the basic equation for the calculation of the pair-excitation energies in the present thesis.

However, the problem of the LDA which does not exhibit the discontinuity of the exchange-correlation potential also prevails here. For that reason, in the bulk limit eq. (2.55) also yields just the LDA gap. This leads to the question as to which parts of the self-energy are described correctly. As the method is, so to speak, a better version of the Δ SCF method eqs. (2.50), (2.51), the discussion about the added constant or R -dependent contribution as given in section 2.2.3.2 is also valid here. In view of the results of Delerue *et al.*, cf. Fig. 2.2, and of the discussion in section 2.2.3.1 this means that for the larger crystallites a contribution corresponding roughly to the bulk self-energy correction should be added, whereas for the smallest crystallite of 5 Si atoms the calculated value should be correct. This can be understood heuristically by considering that the effect of the spatial quantization is much stronger than the many-body effects when the NC radius is much smaller than the free-exciton radius. In the large-crystallite limit, on the other hand, the discontinuity of the exchange-correlation potential is needed. This will be discussed with respect to our calculated excitation energies in the results section 4.1.2.

2.2.4 Other methods to calculate excitation energies of nanostructures

The solution of the many-body problem has been targeted with a number of other methods. Simple approaches to the electronic structure (and, subsequently, optical properties) of NCs included the effective-mass approximation (EMA) which calculates electronic states for electrons and holes with an effective mass in a model confinement potential [8, 91, 92]. This method is accurate in the bulk limit, while for small systems the representation of the true situation is poor. This is easily understandable merely from the fact that the EMA has been derived for slowly varying potentials¹⁰, which is not valid down to the small sizes of nanostructures where the nanostructure size becomes comparable to the interatomic spacing [8, 93, 94].

¹⁰Slowly varying in this context means that the wave functions can be separated into an *envelope* function which is smooth at the level of the extension of the structure, and a part which represents the variations on the atomic length scale. For nanostructures, measuring a few or dozens of atoms across, this is not the case.

The same can be said, in general, about the empirical-pseudopotential approaches. Here, instead of deploying the full formalism of *ab initio* pseudopotential theory, potentials are created by fitting procedures to bulk properties [95]. Again, the bulk limit is necessarily reproduced well. The method has also been applied to quantum dots with a great deal of success, see, e.g., Ref. [8]. In particular, the calculated single-particle wave functions can be used to calculate physical properties like the exchange splitting in excitons using Coulomb integrals [96,97] or the influence of correlation [97]. However, when scaled down to the smallest sizes, the results become questionable. E.g., the pressure dependence of the gaps in Ge NCs is not in agreement with the results from the present *ab initio* calculations [98,99].

Another widely used approach is the tight-binding (TB) description of the electronic structure [9]. For small sizes, the transferability of the bulk atomic interaction parameters is, however, not immediately obvious. While the method fares much better than the EMA, its results in the smallest size range must be taken *cum grano salis* [100].

Conventional DFT is basically a ground state theory. This limitation is no longer there for the **T**ime-**D**ependent DFT (TDDFT) [19, 101, 102] where the response of an electron to a time-dependent external potential is derived by searching the extrema of the quantum-mechanical action functional, which leads to a time-dependent Kohn-Sham equation [19]. In general, TDDFT in the adiabatic local-density approximation (TDLDA) seems to fare well for excitation energies in confined systems like Na_4 clusters [103] as well as for electron energy-loss spectra of solids, but it improves only slightly upon the RPA absorption spectra of solids [104].

The Hartree-Fock approximation, applied on the single-particle level, neglects correlation effects. (In fact, correlation is *defined* as the difference between the exact and the HF result for the ground-state configuration.) If the full Hamiltonian (2.1) is applied to a trial wave function, this is due to the use of a single Slater determinant. However, if instead a sum over all Slater determinants is used, i.e., determinants including excited states, the resulting equation is the exact description of the system because the linear combination of Slater determinants is the most general form of a function compatible with the Pauli principle. The practical implementation of this approach, popular especially among chemists, is called **C**onfiguration **I**nteraction (CI). Appealing though it is, CI is limited to very small particle numbers due to its unfavorable exponential scaling [19]. In fact, full CI can hardly be done for more than five electrons [105]. However, partial inclusion of the correlation effects is possible for a limited number of Slater determinants. For instance, correlation has been included via CI into the calculation of HF excitation energies of Si crystallites [33]. Moreover, CI has also been used starting from the single-particle wave functions obtained from empirical-pseudopotential calculations [97].

Finally, Quantum-Monte-Carlo (QMC) methods [106] have been applied successfully to the problem of excitation energies of crystallites [107].

2.2.5 Spin: singlet vs. triplet excitons

Optical excitation usually creates singlet excitons due to the spin selection rule, which afterwards recombine without change when exchange is weak. However, in strongly confined Si systems there are many (indirect) observations of triplet excitons due to the electron-hole exchange interaction [22, 108–110]. Since the corresponding optical transitions are spin-forbidden they have been termed “dark” excitons in contrast to the ‘bright’ spin-allowed singlet excitons [39]. Usually the triplet excitons are slightly lower in energy. The splitting can be determined from fitting measured life times using a model [108] that accounts for both singlet and triplet excitons [22, 108–110].

The spin-density is given as the expectation value of the spin-density operator. Its z component is (cf. eqs. (2.3) and (2.22))

$$s_z(\mathbf{r}) = \frac{\hbar}{2} \sum_{\alpha\beta} \langle \Psi | \hat{\Psi}_\alpha^\dagger(\mathbf{r}) \sigma_{\alpha\beta}^z \hat{\Psi}_\beta(\mathbf{r}) | \Psi \rangle \quad (2.56)$$

$$= \frac{\hbar}{2} [n_\uparrow(\mathbf{r}) - n_\downarrow(\mathbf{r})]. \quad (2.57)$$

The total electronic spin integrates to

$$S_z = \int d^3\mathbf{r} s_z(\mathbf{r}) = \frac{\hbar}{2} [N_\uparrow(\mathbf{r}) - N_\downarrow(\mathbf{r})], \quad (2.58)$$

where for the last step we assume that only integer occupations $\gamma_i^{(a)}$ are used, cf. eq. (2.53). In the present work we describe, in this way, excitations of electron-hole pairs with $S_z = 1$ (triplet) and $S_z = 0$ (singlet), by setting the occupation accordingly.¹¹ The spin or exchange splitting of the exciton energies is given by

$$\Delta E = E_g^{\text{opt}}(S_z = 0) - E_g^{\text{opt}}(S_z = 1) \quad (2.59)$$

with the excitation energies E_g^{opt} of eq. (2.55) and the z projection of the spin fixed by setting the occupation number accordingly, cf. eq. (2.53).

The splitting is given by the electron-hole exchange term

$$2 \int d^3\mathbf{r}_1 d^3\mathbf{r}_2 \frac{e^2}{|\mathbf{r}_1 - \mathbf{r}_2|} \psi_h^*(\mathbf{r}_1) \psi_e^*(\mathbf{r}_2) \psi_h(\mathbf{r}_2) \psi_e(\mathbf{r}_1) \quad (2.60)$$

as discussed for confined systems, e.g., in Ref. [39].

However, DFT-LSDA [55] as used here is not able to describe pure multiplets. This is a general problem [111]. A rigorous description of multiplets requires symmetry-adapted exchange-correlation functionals, which are not available [112]. In the spin-polarized approach one can

¹¹In practical terms, in the VASP code [61] we specify occupation numbers for the spin-up and spin-down electrons, respectively. For $N_\uparrow = N_\downarrow = N/2$ a singlet exciton is described by occupation numbers $\gamma_{N/2-2}^\uparrow = 1, \gamma_{N/2-1}^\uparrow = 1, \gamma_{N/2}^\uparrow = 0, \gamma_{N/2+1}^\uparrow = 1, \gamma_{N/2+2}^\uparrow = 0$, etc., and $\gamma_{N/2-2}^\downarrow = 1, \gamma_{N/2-1}^\downarrow = 1, \gamma_{N/2}^\downarrow = 1, \gamma_{N/2+1}^\downarrow = 0, \gamma_{N/2+2}^\downarrow = 0$, etc. Accordingly, the triplet exciton is described by $\gamma_{N/2-2}^\uparrow = 1, \gamma_{N/2-1}^\uparrow = 1, \gamma_{N/2}^\uparrow = 0, \gamma_{N/2+1}^\uparrow = 0, \gamma_{N/2+2}^\uparrow = 0$, etc., and $\gamma_{N/2-2}^\downarrow = 1, \gamma_{N/2-1}^\downarrow = 1, \gamma_{N/2}^\downarrow = 1, \gamma_{N/2+1}^\downarrow = 1, \gamma_{N/2+2}^\downarrow = 0$, etc.

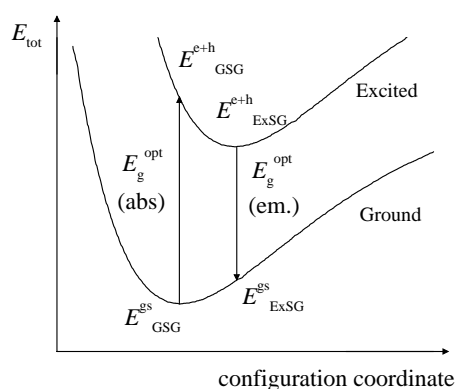


Figure 2.3 Schematic representation of the processes that produce the Stokes shift. The y -axis is in this representation, strictly speaking, the energy of the involved valence state (in our case generally the HOMO) and the excited state (here: the LUMO). The sub- and superscripts are GSG for Ground-State Geometry, ExSG for Excited-State Geometry, and e+h for electron-hole pair. E_{tot} is the total energy, cf. eq. (2.36).

only fix the projection M_S of the total spin S but not the total spin itself. One describes actually a high-spin state with $S = 1$, $M_S = \pm 1$ (which is a triplet state) and a low-spin state with $M_S = 0$ (which might be a mixture of spin states). Consequently, this approach tends to underestimate the spin splitting and gives a lower limit to the possible values.

2.2.6 Stokes shifts

Measured PL peak energies of NC samples are red-shifted with respect to the lowest absorption energies [47]. This shift is influenced by two main contributions. First of all, after thermalization of electrons and holes the line width of the PL spectra determines the shifts as discussed in Refs. [113, 114]. This is an effect of the size distribution of the crystallites. The recombination probability of the electron-hole pairs is, roughly, inversely proportional to the transition energy. Consequently, after non-resonant high-energy excitation the larger NCs of a sample with a size distribution contribute more to the PL signal. In an absorption experiment, on the other hand, more or less all NCs contribute. We do not consider this contribution to the Stokes shift in the present work, as this would require knowledge of the size distribution of the experimental sample.

Second, there is the structural contribution which is determined by the structural relaxation of the individual NCs after an optical excitation as visualized in Fig. 2.3. This has also been called Franck-Condon shift [115]. For each of the different electronic states (ground state, excited state), a total-energy curve exists along a — possibly fictitious — configuration coordinate. Electronic excitation (or recombination) thus takes place between two such total-energy curves. For each of them, a total-energy minimum is assumed after the *structural* relaxation following the electronic excitation. As the electronic movements are by orders of magnitude faster than the motion of the cores, the electronic relaxation may be considered instantaneous, whereas the structural relaxation is slow. An absorption event hence takes place from the minimum of the ground-state curve E_{GSG} to a state on the excited-state total energy curve, $E_{\text{GSG}}^{\text{e+h}}$. Here we drop the index N but instead indicate if they are calculated for the ground-state geometry (GSG) or the excited-state geometry (ExSG). All the energies here are of the N -electron system. After that, the structure will relax such that the electron assumes the minimum on the excited-state total-energy curve, $E_{\text{ExSG}}^{\text{e+h}}$. This can involve transitions between different vibrational states; this

will, in general, take place as a non-radiative relaxation. For the emission, i.e., the transition from $E_{\text{ExSG}}^{\text{e+h}}$ to E_{ExSG} , the transition energy is lower. The resulting red-shift

$$\Delta_{\text{Stokes}} = (E_{\text{GSG}}^{\text{e+h}} - E_{\text{GSG}}) - (E_{\text{ExSG}}^{\text{e+h}} - E_{\text{ExSG}}) \quad (2.61)$$

is the structural contribution to the Stokes shift.

Finally, another contribution to the Stokes shift is due to the splitting between the singlet and the triplet exciton [115, 116]. This is connected with the selection rules and has to be considered when experimental data are interpreted. However, the Stokes shifts of the present work have been calculated mostly for non-spin-polarized systems.

2.3 Optical Properties

2.3.1 Dielectric function

In order to calculate the optical properties of a material, the response to an external potential must be determined. We are, in the present work, interested in the influence of the confinement on the optical properties. These are restricted to linear response and described in the independent-particle approximation, neglecting local-field effects.

We use the supercell method, cf. chapter 3 below. Therefore we have, despite the fact that we treat localized structures, a system with translational symmetry. Consequently the eigenfunctions of the Hamiltonian eq. (2.1) are Bloch functions. Thus the following treatment is written in terms of Bloch functions, in particular because the meaning of the wave vector is then easily apparent.

We need to calculate the response of the system to an external perturbing potential $V^{\text{pert}}(\mathbf{r}, t)$. To this end, we write the total potential $V(\mathbf{r}, t)$ as the sum of the external potential $V^{\text{pert}}(\mathbf{r}, t)$ and the potential $V^{\text{ind}}(\mathbf{r}, t)$ induced by $V^{\text{pert}}(\mathbf{r}, t)$:

$$V(\mathbf{r}, t) = V^{\text{pert}}(\mathbf{r}, t) + V^{\text{ind}}(\mathbf{r}, t). \quad (2.62)$$

The inverse dielectric function $\varepsilon^{-1}(\mathbf{r}, \mathbf{r}', t)$ is now introduced after Fourier transformation,

$$V(\mathbf{q} + \mathbf{G}, \omega) = \sum_{\mathbf{G}'} \varepsilon^{-1}(\mathbf{q} + \mathbf{G}, \mathbf{q} + \mathbf{G}', \omega) V^{\text{pert}}(\mathbf{q} + \mathbf{G}', \omega) \quad (2.63)$$

where \mathbf{G} and \mathbf{G}' are reciprocal lattice vectors and \mathbf{q} is the wave vector of the external perturbing potential. It connects the latter with the total potential $V(\mathbf{r}, t)$. Due to the spatial inhomogeneity, cf. (2.62), the dielectric function is a matrix with respect to \mathbf{G} and \mathbf{G}' .

In the independent-particle approximation and after Fourier transformation the dielectric matrix is given by

$$\varepsilon(\mathbf{q} + \mathbf{G}, \mathbf{q} + \mathbf{G}'; \omega) = \delta_{\mathbf{G}\mathbf{G}'} - \frac{4\pi e^2}{|\mathbf{q} + \mathbf{G}|^2 V} P(\mathbf{q} + \mathbf{G}, \mathbf{q} + \mathbf{G}'; \omega) \quad (2.64)$$

with the polarizability [117]

$$P(\mathbf{q} + \mathbf{G}, \mathbf{q} + \mathbf{G}', \omega) = \sum_{n,n'} \sum_{\mathbf{k}, \mathbf{k}'} B_{n,n'}^{\mathbf{k}, \mathbf{k}'}(\mathbf{q} + \mathbf{G}) B_{n,n'}^{\mathbf{k}, \mathbf{k}'*}(\mathbf{q} + \mathbf{G}') \frac{f(\varepsilon_n(\mathbf{k})) - f(\varepsilon_{n'}(\mathbf{k}'))}{\hbar\omega + \varepsilon_n(\mathbf{k}) - \varepsilon_{n'}(\mathbf{k}') + i\eta} \quad (2.65)$$

containing the Bloch integrals

$$B_{n,n'}^{\mathbf{k},\mathbf{k}'}(\mathbf{q}) = \int d^3\mathbf{r} \phi_{n\mathbf{k}}^*(\mathbf{r}) e^{-i\mathbf{q}\mathbf{r}} \phi_{n'\mathbf{k}'}(\mathbf{r}) \quad (2.66)$$

and the Fermi functions $f(\varepsilon(\mathbf{k}))$ which determine the γ_i in eq. (2.53). The $\phi_{n\mathbf{k}}^*(\mathbf{r})$ are Kohn-Sham Bloch wave functions.

The off-diagonal elements of the dielectric matrix describe the local-field effects, i.e., the difference between the microscopic and the macroscopic induced fields due to the atomic structure of the solid. In the present work, local-field effects are neglected throughout. It is apparent from eq. (2.63) that in this case all the Fourier components of the perturbation are screened independently.

The dielectric function eq. (2.64) has been derived here for a longitudinal perturbation, i.e., a perturbation resulting from an external charge. In the optical limit $\mathbf{q} \rightarrow 0$ one can demonstrate the equality of the longitudinal and the transverse (resulting from an external vector potential) dielectric function $\lim_{\mathbf{q} \rightarrow 0} \varepsilon_l(\mathbf{q}, \omega) = \lim_{\mathbf{q} \rightarrow 0} \varepsilon_t(\mathbf{q}, \omega)$ [118, 119]. Hence we do not distinguish between the symbols of the longitudinal and the transverse dielectric function.¹²

For practical calculations, interband transition matrix elements of the form [120]

$$\lim_{\mathbf{q} \rightarrow 0} \langle c\mathbf{k} | e^{i\mathbf{q}\mathbf{r}} | v\mathbf{k}' \rangle = \lim_{\mathbf{q} \rightarrow 0} i\mathbf{q} \langle c\mathbf{k} | \mathbf{r} | v\mathbf{k}' \rangle \quad (2.67)$$

have to be calculated, which has to be done with care. Otherwise, ill-defined quantities like matrix elements of the dipole operator appear [162]. Instead, use is made of the relation

$$\langle c\mathbf{k} | [e^{i\mathbf{q}\mathbf{r}}, \hat{H}_s]_- | v\mathbf{k}' \rangle = [\varepsilon_v(\mathbf{k}') - \varepsilon_c(\mathbf{k})] \langle c\mathbf{k} | e^{i\mathbf{q}\mathbf{r}} | v\mathbf{k}' \rangle, \quad (2.68)$$

\hat{H}_s being the single-particle Hamiltonian of the independent particles [121]. As the two concerned bands are different, the transition matrix elements can be related to matrix elements of the velocity operator $\hat{\mathbf{v}}$ which now assumes the role of the optical transition operator,

$$\lim_{q_\alpha \rightarrow 0} \frac{1}{\hbar q_\alpha} [e^{iq_\alpha r_\alpha}, \hat{H}_s]_- = \frac{i}{\hbar} [r_\alpha, \hat{H}_s]_- = -\hat{v}_\alpha.$$

Consequently we do not have to carry out the transition $\mathbf{q} \rightarrow 0$ explicitly. Instead, we have now the requirement $\mathbf{k} = \mathbf{k}'$; only transitions between states with equal \mathbf{k} contribute.

In the present work we use all-electron wave functions obtained using the projector-augmented-wave method (PAW) as described in section 2.4 below. For that reason, the simple relationship

$$\hat{\mathbf{v}} = \frac{\hat{\mathbf{p}}}{m} \quad (2.69)$$

is valid [121], introducing the momentum operator \mathbf{p} . This replacement leads to a modified Ehrenreich-Cohen formula for the dielectric function

$$\varepsilon_{\alpha\beta}(\omega) = \delta_{\alpha\beta} + \frac{16\pi e^2 \hbar^2}{\Omega m^2} \sum_{\mathbf{k}} \sum_{cv} \frac{1}{[\varepsilon_c(\mathbf{k}) - \varepsilon_v(\mathbf{k})]} \frac{\langle c\mathbf{k} | \hat{\mathbf{p}}_\alpha | v\mathbf{k} \rangle \langle v\mathbf{k} | \hat{\mathbf{p}}_\beta | c\mathbf{k} \rangle}{[\varepsilon_c(\mathbf{k}) - \varepsilon_v(\mathbf{k})]^2 - \hbar^2(\omega + i\eta)^2}, \quad (2.70)$$

¹²In cubic materials, the dielectric function is diagonal, $\varepsilon_{\alpha\beta}(\omega) = \varepsilon(\omega)\delta_{\alpha\beta}$; only one independent component exists. Consequently, the equality of longitudinal and transverse dielectric function holds for arbitrary directions of \mathbf{q} . Moreover, in the present work we use $\varepsilon(\omega)$ without indicating the tensorial character, except where necessary as for instance in the case of hexagonal material.

which here is written including the tensorial nature of the quantity. For systems of cubic symmetry, the tensor has just one independent component; the response is isotropic.

Without damping, i.e., for $\eta = 0$, the imaginary part of the dielectric function

$$\text{Im } \varepsilon_{\alpha\beta}(\omega) = \frac{8\pi^2 e^2 \hbar^2}{\Omega m^2} \sum_{cv} \sum_{\mathbf{k}} \frac{\langle c\mathbf{k} | \hat{p}_\alpha | v\mathbf{k} \rangle \langle v\mathbf{k} | \hat{p}_\beta | c\mathbf{k} \rangle}{[\varepsilon_c(\mathbf{k}) - \varepsilon_v(\mathbf{k})]^2} \delta[\varepsilon_c(\mathbf{k}) - \varepsilon_v(\mathbf{k}) - \hbar\omega] \quad (2.71)$$

and its real part

$$\text{Re } \varepsilon_{\alpha\beta}(\omega) = \delta_{\alpha\beta} + \frac{16\pi e^2 \hbar^2}{\Omega m^2} \sum_{cv} \sum_{\mathbf{k}} \frac{\langle c\mathbf{k} | \hat{p}_\alpha | v\mathbf{k} \rangle \langle v\mathbf{k} | \hat{p}_\beta | c\mathbf{k} \rangle}{[\varepsilon_c(\mathbf{k}) - \varepsilon_v(\mathbf{k})] [\varepsilon_c(\mathbf{k}) - \varepsilon_v(\mathbf{k})^2 - (\hbar\omega)^2]} \quad (2.72)$$

are obtained. Eq. (2.71) has been used in the present work for the practical implementations of the theory presented here.

2.3.2 Radiative recombination

The derivation of eq. (2.71) shows that it is just Fermi's golden rule in the dipole approximation and the one-electron picture [122, 123]. In order to describe photoluminescence — the quantity of prime interest for the nanostructures intended for optoelectronics — one has to calculate the radiative lifetimes averaged over the relevant transitions. Assuming that the thermalization is faster than the radiative recombination, the electron-hole pairs will be thermalized according to the temperature T of the system. In this case, the averaged recombination rate determining the radiative life time – again in independent-particle approximation – is given by [124, 125]

$$\tau^{-1} = 4 n_{\text{eff}} \frac{e^2}{\hbar^2 m c^3} \frac{\sum_{\mathbf{k}} \sum_{c,v} f_{cv}^{\alpha\alpha}(\mathbf{k}) (\varepsilon_c(\mathbf{k}) - \varepsilon_v(\mathbf{k}))^2 \exp\left(-\frac{\varepsilon_c(\mathbf{k}) - \varepsilon_v(\mathbf{k})}{kT}\right)}{\sum_{c,v} \exp\left(-\frac{\varepsilon_c(\mathbf{k}) - \varepsilon_v(\mathbf{k})}{kT}\right)}, \quad (2.73)$$

where n_{eff} is the effective refractive index and the $f_{cv}^{\alpha\alpha}(\mathbf{k})$ are the oscillator strengths [126]

$$f_{cv}^{\alpha\beta}(\mathbf{k}) = \frac{1}{m} \frac{\langle \mathbf{k}c | p_\alpha | \mathbf{k}v \rangle \langle \mathbf{k}v | p_\beta | \mathbf{k}c \rangle + \langle \mathbf{k}c | p_\beta | \mathbf{k}v \rangle \langle \mathbf{k}v | p_\alpha | \mathbf{k}c \rangle}{\varepsilon_c(\mathbf{k}) - \varepsilon_v(\mathbf{k})} \quad (2.74)$$

for the optical transition between a conduction state c and a valence state v . In our case, these are Kohn-Sham states. The peak energies of PL spectra correspond roughly to the energy of the lowest optically allowed transition in the excited system, see also section 2.2.6. The measurement of Stokes shifts and radiative lifetimes can, therefore, give valuable information about the structure and the processes in the NCs.

2.4 Projector-Augmented-Wave Method and Matrix Elements

The Kohn-Sham equation contains the potential of the atomic nuclei as the “external” potential. All electrons are contained as individual particles. However, the bonding and optical properties

of solids are primarily determined solely by the valence electrons, and here, in turn, in the interatomic regions. This is exploited by the pseudopotential approaches in two ways [127].

First, one creates an ionic core from the nucleus and the inner shells of electrons. The assumption of the “frozen core approximation” [128] is that this ionic core is unchanged when the chemical situation of the valence electrons is changed. The distinct advantage of this is that the deep Coulomb potentials at the atomic positions are replaced by much “softer” screened Coulomb potentials. Moreover, the number of electrons to be treated is reduced.¹³ The pseudopotential creation now simplifies the wave functions of the valence electrons by removing the oscillations in the core region whose description is only of minor importance for the sought-for quantities. This can be done because now the core electrons are part of the inert core, and the valence wave functions do not have to be orthogonalized with respect to them. However, in certain cases a so-called “non-linear core correction” has to be added. In the present work this is important for Ge due to its $3d$ electrons.

In the construction of the pseudopotential, the removal of the core-region oscillations of the valence wave functions is done for the atom. There is a great deal of freedom how this can be done, and many different schemes have been conceived by, e.g., Phillips and Kleinman [130], Bachelet, Hamann, and Schlüter [131, 132], Troullier and Martins [133], and Vanderbilt [134]. The basic idea is to take the wave functions and construct some well behaved “pseudo”-version of it which inside some cut-off radius is smooth. Outside, however, it must be identical with the true wave functions which in this context are called “all-electron wave functions”.¹⁴ In the initial pseudopotential idea, a projection procedure by means of the core states was used [130]. While initially the norm of the wave functions inside the cut-off radius was required to be equal to that of the original wave function, this requirement has been shown to be dispensable [134], leading to “softer” potentials and hence reduced numerical efforts [135].

Subsequently, the Schrödinger equation (or, for a better description, its relativistic counterpart [136]) is inverted. In this manner, a “screened” pseudopotential is created. The construction yields potentials for different angular momenta; the pseudopotentials are, in general, nonlocal. For the technical treatment, an “unscreening” procedure yields the ionic pseudopotential which, like the pseudo-wave-function, is much smoother than its all-electron counterpart [136]. Moreover, for numerical convenience, the pseudopotential can be transcribed into a fully nonlocal form which in \mathbf{k} space factorizes and thus facilitates the calculations [137].

In general, the scattering properties of the pseudopotentials have to be the same as those of the corresponding all-electron potential, which must also hold in different chemical environ-

¹³While in some cases like the group-IV elements, the choice of the valence electrons is hardly any issue, in other cases this can be different, as in the case of extended d-electrons. In general, a higher number of valence electrons will result in deeper core potentials and, hence, in much higher cut-off energies. In the case of Ge, the cut-off for a decent band-structure calculation with norm-conserving pseudopotentials is about 4 Hartree for a 4-valence-electron potential, while it is increased to about 150 Hartree when 22 valence electrons are used [129].

¹⁴We mention that the term “all-electron” as used attributively for the wave functions or the potentials is somehow misleading. It does not refer to the number of electrons considered for the valence states. [There are also frozen-core all-electron calculations.] Instead, it signifies that – unlike in the pseudopotential approximation – the whole one-particle wave function of any valence electron is considered.

ments. The respective tests are dealing with this problem under the name “transferability” and “chemical hardness” [136].

The effect of introducing the pseudopotentials is a modified Kohn-Sham equation which neglects effects of the core regions but is much more tractable numerically. Especially for a plane-wave expansion of the KS wave functions, the numerical effort is drastically reduced. The description of the properties, lattice constants, bulk moduli, and even optical properties (see, e.g., Ref. [138] and references therein, as well as Ref. [139], reproduces the true quantities rather well – *iff well-constructed pseudopotentials are used*. For large systems like ours, usually non-norm-conserving pseudopotentials are used. However, due to the relaxation of the norm-conservation condition, the method does not yield wave functions in the core region as it is necessary for the for the calculation of the transition matrix elements of eq. (2.69).

This can be solved by means of the projector-augmented-wave (PAW) method [140] which is, in its philosophy, slightly different from the pseudopotential method. While it also seeks to construct smooth valence-electron wave functions, it does not rely on the negligibility of their core regions for the description of the desired properties. Instead, a transformation \mathcal{T} is introduced between the space of all-electron (AE) wave functions $|\psi\rangle$ (which can – but do not have to – be the Kohn-Sham wave functions of equation (2.20)) and of smooth, numerically convenient pseudo-wave-functions (PS) $|\tilde{\psi}\rangle$,

$$|\psi\rangle = \mathcal{T}|\tilde{\psi}\rangle \Leftrightarrow |\tilde{\psi}\rangle = \mathcal{T}^\dagger|\psi\rangle \quad (2.75)$$

and consequently for operators

$$A = \mathcal{T}\tilde{A}\mathcal{T}^\dagger \Leftrightarrow \tilde{A} = \mathcal{T}^\dagger A\mathcal{T}. \quad (2.76)$$

We want to determine the transformation

$$\mathcal{T} = 1 + \sum_R \mathcal{T}_R \quad (2.77)$$

such that it is unity apart from local, atom-centered transformations \mathcal{T}_R which act only inside an augmentation region Ω_R around each atom. Only within this augmentation region – similar to the core region of the pseudopotential approach – are $|\tilde{\psi}\rangle$ and $|\psi\rangle$ different. The \mathcal{T}_R are defined inside the augmentation region by the specification of a set of target functions $|\phi_i\rangle$ of \mathcal{T}_R or AE partial waves, and a set of initial functions $|\tilde{\phi}_i\rangle$ or pseudo-partial-waves which is complete in the augmentation region and orthogonal to the core states. The name partial waves stems from the fact that the solutions of the radial Schrödinger equation multiplied by spherical harmonics present a natural choice for these functions. Outside the augmentation region, the PS partial waves are identical to the AE partial waves.

One finds that the general form of the transformation is

$$\mathcal{T} = 1 + \sum_i (|\phi_i\rangle - |\tilde{\phi}_i\rangle) \langle \tilde{p}_i| \quad (2.78)$$

with the *projector functions* $|\tilde{p}_i\rangle$ which must be dual to the PS partial waves,

$$\langle \tilde{p}_i|\tilde{\phi}_j\rangle = \delta_{ij}. \quad (2.79)$$

The freedom in the construction of the pseudo-wave-function is now contained in the construction of the projector functions. Following a suitable choice of these, the PAW method has a direct relationship with the ultrasoft-pseudopotentials [134, 141].

The linear transformation (2.78) now connects the AE- and the PS-wave-function according to eq. (2.75). This rests on the assumption of completeness of the projector functions inside the augmentation sphere. Unlike in the pseudopotential approach, which is an approximation, one can now transform the original all-electron Kohn-Sham equation into a numerically more convenient PS-Kohn-Sham equation by transforming all operators and the wave functions by means of \mathcal{T} . This equation can be solved, e.g., using the usual plane-wave expansion of the Hamiltonian's \tilde{H} eigenfunctions. The desired quantities are then obtained using a back-transformation via the inverse of \mathcal{T} . Expressions for the transformed quantities are given in the references [140, 141]. For a local operator A , the result is

$$\tilde{A} = \mathcal{T}^\dagger A \mathcal{T} = A + \sum_{ij} |\tilde{p}_i\rangle \left(\langle \phi_i | A | \phi_j \rangle - \langle \tilde{\phi}_i | A | \tilde{\phi}_j \rangle \right) \langle \tilde{p}_j|. \quad (2.80)$$

The target quantities of the present work contain momentum-operator matrix elements, as shown in eqs. (2.71), (2.72), and (2.73). The matrix element of \mathbf{p} between the AE wave functions n and m within the PAW description is then naturally given, according to the inversion of eq. (2.80), by [139]

$$\mathbf{p}_{nm} = \mathcal{T} \mathbf{p}_{nm} \mathcal{T}^\dagger = \langle \tilde{\Psi}_n | \mathbf{p} | \tilde{\Psi}_m \rangle + \sum_{ij} \langle \tilde{\Psi}_n | \tilde{p}_i \rangle \left(\langle \phi_i | \mathbf{p} | \phi_j \rangle - \langle \tilde{\phi}_i | \mathbf{p} | \tilde{\phi}_j \rangle \right) \langle \tilde{p}_j | \tilde{\Psi}_m \rangle. \quad (2.81)$$

The first term on the right-hand side of eq. (2.81) corresponds to the usual pseudopotential description (identifying the $|\tilde{\Psi}\rangle$ with the pseudo-wave-functions) which simply neglects the effect of the pseudo-description of the core region. The additional terms follow naturally from the PAW method and correct the result for this omission. They are formally identical to the *core repair term* that has been introduced independently by Kageshima and Shiraishi [142]. It has been shown [139] that for materials with rather localized core states, like C, Si, or SiC, this description is roughly equivalent to standard pseudopotential calculations of the optical spectra. However, in the presence of extended shallow core orbitals, the PAW method improves distinctly over the pseudopotential description.

Furthermore, as the PAW method yields all-electron wave functions, the simple relation eq. (2.69) connects the velocity and the momentum operator. This means that one does not have to take into account the cumbersome additional contribution due to the non-local terms in the one-particle Hamiltonian [121] as it has to be done for the conventional pseudopotentials.

Chapter 3

Model, Method, and Numerical Implementation

3.1 Model

Two distinct model systems have been treated: Free, hydrogen-terminated group-IV crystallites and crystallites embedded in a crystalline matrix. The H-saturation is used to model the high potential barrier for electrons and holes of a NC embedded in a wide-gap or insulating matrix. It prevents surface effects and dangling bonds. At the same time, these structures are a model for hydrogenated NCs in porous silicon. On the other hand, the embedment of NCs in a crystalline matrix seeks to investigate directly the relevant effects including interface and strain. Moreover, the partial localization of electrons or holes is investigated in these structures.

3.1.1 Free crystallites

We construct NCs by starting from one atom and adding its nearest neighbors, thereby assuming the tetrahedral coordination as well as the interatomic distances of the respective cubic bulk materials. Successively adding the nearest neighbors of the surface atoms shell by shell we obtain NCs of $N = 5, 17, 41, 83, 147, 239,$ and 363 atoms. The remaining dangling bonds are saturated by H atoms. Thereby N denotes the number of atoms in the NC, disregarding the hydrogen atoms. Similar construction procedures have been applied by different groups [14,39,143,144]. The system is illustrated in Fig. 3.2. The point group of the resulting NCs is T_d , i.e., inversion is the only missing point-symmetry operation compared to the initial diamond-structured bulk material. Inspection of the model NCs reveals that they are not precisely spherical but exhibit small facets at the surface due to the construction procedure. Basically, their shape is a cube with cut-off corners in such a way that triangular faces arise which connect the midpoints of the rectangles that touch at the respective corner. They have six rectangular faces corresponding to a $\langle 001 \rangle$ orientation as well as eight faces corresponding to a $\langle 111 \rangle$ orientation. However, the construction procedure results in two different situations, alternating with increasing number of shells: Either the six $\{001\}$ faces are quadratic, in which case the $\{111\}$ facets are of the same size. This is the case for the NCs of $N = 17, 83, 239,$ etc. atoms. Alternatively, for the NCs of

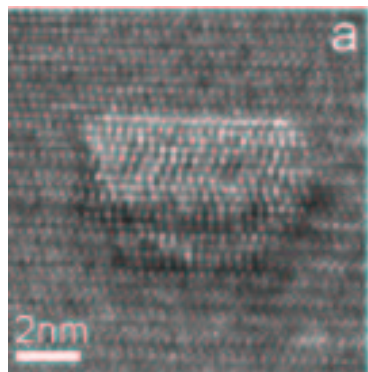


Figure 3.1 HRTEM image of cubic GeSi nanocrystal in hexagonal SiC [5, 145]

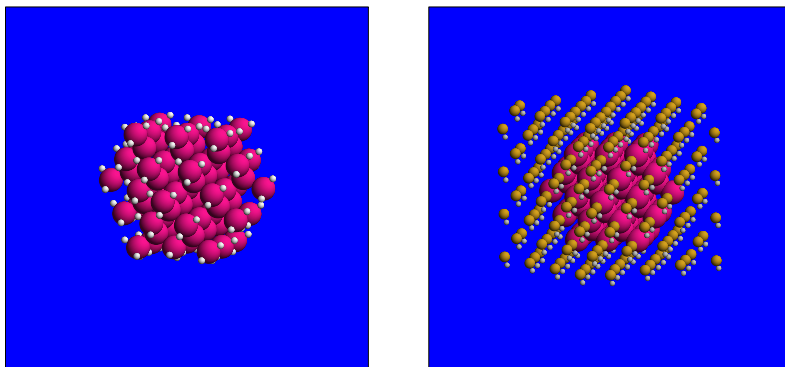


Figure 3.2 Example of model structures: NC of 83 Ge or Si atoms, surrounded by 108 H atoms for the free NC (left panel), or by a matrix containing Si (yellow) and C (grey) atoms (right panel).

$N = 41, 148, 363$, etc. atoms, the six $\{001\}$ faces are rectangular with edge lengths differing by one atom. In these cases, two different kinds of triangular $\{111\}$ facets arise. Even in the first case of equal edge lengths of the $\{111\}$ facets, they are inequivalent due to the construction procedure.

The T_d symmetry is always kept in the present work except in those cases where the effects of lowered symmetry have been studied, which is then indicated in the text.

We consider simple-cubic supercells, both for simplicity and because in this case the number of nearest-neighbor supercells is smallest. When no symmetry is broken the IBZ is itself a tetrahedron. A simple-cubic supercell is constructed by basis vectors $\mathbf{a}_1 = Na_0(1, 0, 0)$, $\mathbf{a}_2 = Na_0(0, 1, 0)$, and $\mathbf{a}_3 = Na_0(0, 0, 1)$. Here N gives the length of the supercell in multiples of the cubic lattice constant a_0 of the underlying diamond structure. Correspondingly, the reciprocal lattice vectors are shortened by a factor of N . Applying $N = 1, 2, 3$, and 4 in each of the three Cartesian directions, one obtains supercells of 8, 64, 216, 512, and 1000 atoms, respectively. Thus, for Ge we use edge lengths of 16.9, 22.6, and 28.2 Å. For the radius of the NCs we take the radius of the sphere of equal volume according to the volume per atom in the bulk.

3.1.2 Crystallites embedded in a crystalline matrix

The second situation dealt with is that of NCs embedded in a crystalline matrix. For most of the calculations, the model system of Ge (or Si) NCs in a SiC matrix has been chosen. The geometry of the NCs is chosen in analogy with the free NCs. The NC atoms now replace the atoms of the host material on a one-to-one basis. Therefore, all bonds at the NC-host interface are saturated. As a starting point, the lattice constant of the host is assumed. Due to the different lattice constants of SiC and Si or Ge, this procedure results in rather strongly strained systems. The system is illustrated in Fig. 3.2. Again, the system's symmetry is T_d .

As a consequence of the construction procedure, the interface bonds between the NC and the matrix are either all Ge-C, or all Ge-Si.

3.2 Electronic-Structure Calculations

3.2.1 Supercell method and description of NCs

Bulk semiconductors have a small primitive cell (2-atomic in the case of cubic Ge and Si) and a correspondingly large Brillouin zone (BZ). A preliminary step towards the supercell method is the construction of a large cell. To this end, the primitive cell of the material is repeated n_i times along the lattice vectors \mathbf{a}_i , leading to cells of $n_1 \times n_2 \times n_3 \times N_0$ atoms, where N_0 is the number of atoms in the primitive cell. Accordingly, the BZ is reduced by a factor of n_i in the respective directions. The bands which are now outside the (supercell-) BZ are translated back (or, more strictly speaking, are equivalent to bands inside the BZ) into the BZ in such a way as to present a *band folding*.

This is a redundant description of the bulk material. However, insertion of a perturbation like a defect or a nanocrystal into this cell makes it the primitive cell of the supercell system. The bands within the new BZ are less dispersive, in absolute terms, but their number has increased by a factor of $n_1 \times n_2 \times n_3$ due to the band folding.

Localization results in weakly dispersive bands. In the case of the strongly confined states in the hydrogen-terminated NCs dispersion is minimal. For the embedded structures one has a large number of bands representing the folded bulk band structure of the host as well as states localized to different degrees, which show still a sizable dispersion due to the interaction of the NCs in adjacent supercells.

By means of the supercell method, the localized structure has been transformed into a new translationally invariant lattice. Consequently all the useful “tools” of solid-state physics can be applied. This concerns especially the plane-wave expansion of the wave functions.

3.2.2 Algorithms and potentials

The optical properties are calculated in the present work within the independent-particle approximation. They are based on the one-particle wave functions calculated using DFT as presented in chapter 2. We employ the Vienna *ab initio* Simulation Package (VASP) [61, 146] with the projector-augmented-wave method (PAW) [139–141], cf. section 2.4. The PAW data sets have been created by J. Furthmüller. The calculation of transition matrix elements eq. (2.81) elements has been incorporated into the VASP package, also by J. Furthmüller. The supercell approach is taken in order to use the plane-wave expansion of the eigenfunctions. The electron-electron interaction is described within the parameterization of Perdew and Zunger [147] of the results of Ceperley and Alder [57]. Nonlinear core corrections are taken into account [148].

In order to obtain an independent reference, two norm-conserving Ge pseudopotentials have been created using the *fhi98pp* code [136]. The calculations for these potentials have been done using the ABINIT package [149]. In Fig. 3.3, we compare the two norm-conserving pseudopotentials of 4 and of 22 valence electrons. In the latter, the whole 3-shell is treated as valence electrons. Obviously the band structures coincide very well, apart from very small differences. This means that the choice of the 4s and 4p electrons as the valence is well justified. Second, we present in Fig. 3.4 the spectra of two H-terminated NCs. While there are certain differences

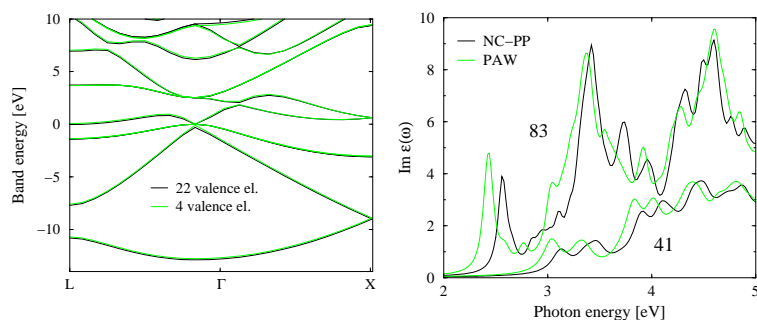


Figure 3.3 Comparison of Ge band structures obtained for two norm-conserving pseudopotentials with 4 and 22 valence electrons, respectively.

Figure 3.4 Comparison of Ge NC spectra obtained by means of the present method with the PAW data sets, compared to spectra obtained for norm-conserving pseudopotential constructed for comparison, and using the ABINIT package. NCs of 83 and 41 Ge atoms have been used.

in the energetic positions of some of the peaks, all the structures correspond very closely to each other, including good agreement of the intensities. In particular the fact that the lowest transitions are very strong is reproduced by both potentials. The latter is a particularly valuable corroboration of our results because the order of the band gaps in Ge is notoriously problematic for pseudopotential calculations in DFT-LDA where the Γ - Γ gap becomes practically zero.

The algorithms used for the electronic-structure calculations by means of VASP are based on the conjugate gradient scheme [150, 151], or, most frequently, a residual minimization scheme - direct inversion in the iterative subspace (RMM-DIIS) [152, 153]. For the mixing of the charge density an efficient Broyden/Pulay mixing scheme [153–155] is used.

The large calculations have been done on RS6000 workstations (with 1, 2 or 4 processors POWER 3 - II, 375 MHz). The treatment of the smaller supercells (up to the 216-atom cells) has also been carried out using standard LINUX PCs with memory between 500kB and 2GB.

3.2.3 \mathbf{k} points and cell size

In the supercell approach as described in section 3.2.1, electronic-structure calculations involve integrals (or sums, depending on whether the \mathbf{k} points are considered discrete) of functions of the \mathbf{k} points over the Brillouin zone. As the number of \mathbf{k} points treatable in a practical calculation is necessarily limited, an approximation has to be found. There are a number of special-point methods which chose a certain number of \mathbf{k} points to represent the mean values as best as possible [156–158]. In the case of the large supercells, the band dispersion inside the BZ is rather small; in terms of the bulk supercell description the effective number of \mathbf{k} points is much higher. It turns out that for the large supercell used in the present work, one \mathbf{k} point is sufficient for a reasonable description of the system.

For the free, hydrogenated NCs which are separated by vacuum, the band structure of the relevant bands is practically dispersionless, only the higher bands are slightly influenced. This is illustrated in Fig. 3.6: In the case of a 83-atom Si NC, the cell corresponding to 216 atoms of bulk material is not yet sufficient, so for this system, the cell corresponding to 512 atoms of bulk was used. Now the question of the \mathbf{k} -point sampling is rendered irrelevant. In fact, for these isolated structures it is only a remnant of the artificial translational symmetry which has been introduced for numerical convenience.

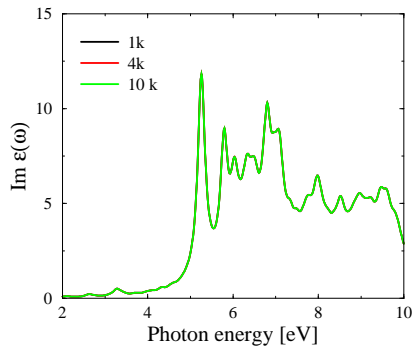


Figure 3.5 Spectrum calculated with one \mathbf{k} point for the calculation of the DF, but with different numbers of \mathbf{k} points for the calculation of the charge density as indicated in the figure.

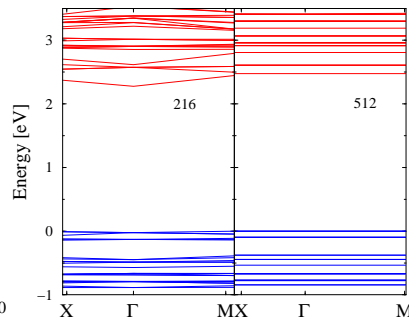


Figure 3.6 Band structures of the supercell system of the free, H-terminated 83-atom Ge NC in the 216- (left) and the 512-atom cell.

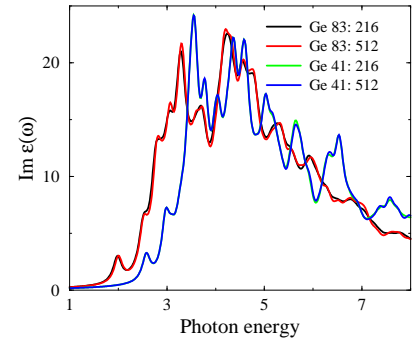


Figure 3.7 Spectra for different cell sizes for two NC sizes and the ideal geometry. The respective spectra are almost indistinguishable.

For the embedded crystallites, the situation is different. If convergence with respect to cell size had been reached, the energy levels due to states localized at the NC should show no dispersion, while the states representing the bulk band structure of the matrix will of course be dispersive. Nonetheless, also here it proved possible to use just one \mathbf{k} point for the NC-host supercell system. As Γ is a high-symmetry point, it does not exhibit any mean-value properties and is not suitable. We have chosen to work with a Monkhorst-Pack mesh [157] of $2 \times 2 \times 2$ \mathbf{k} points along the coordinate axes, which for the T_d systems reduces to one \mathbf{k} irreducible point, viz.

$$\mathbf{k}_{222} = \left(\frac{1}{4}, \frac{1}{4}, \frac{1}{4} \right). \quad (3.1)$$

In order to check the convergence of the electronic-structure calculation with respect to the number of \mathbf{k} points, Fig. 3.5 shows test spectra for a 5-atom Ge NC embedded in SiC in a 64-atom supercell: The electronic structure calculation has been done using $2 \times 2 \times 2 = 1$, $4 \times 4 \times 4 = 4$, and $6 \times 6 \times 6 = 10$ \mathbf{k} irreducible points. The resulting charge density was then used to calculate the spectrum using only \mathbf{k}_{222} . While this is of course not converged with respect to the number of \mathbf{k} points used for the spectrum (see below, section 3.4), it shows that the electronic structure calculation is rather well converged: The three spectra are virtually indistinguishable. For the larger cells which have been used in the present work, the situation will be even more favorable due to the higher number of band foldings.

For consistency we have used the same \mathbf{k} point for the calculations treating the free NCs, even though here, due to the practically vanishing dispersion, the Γ point would have been acceptable as well. A fortuitous fact is indicated in Fig. 3.7: Even in those cases where the band structure shows dispersion, the spectra prove very insensitive to this. The spectra for the 83-atom NC as calculated for the two different cell sizes used also in Fig. 3.6 do not show any distinct differences. The spectra have been scaled as discussed in section 4.1.6. This finding is also another indication that – as expected – the description of the system using just one \mathbf{k} point is sufficient. For the free NCs this holds also for the calculation of the spectra. For the embedded

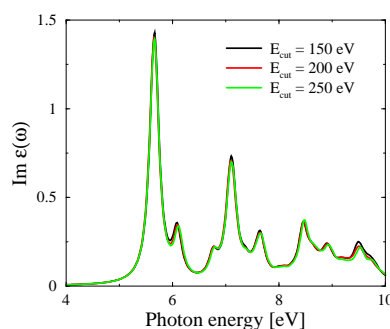
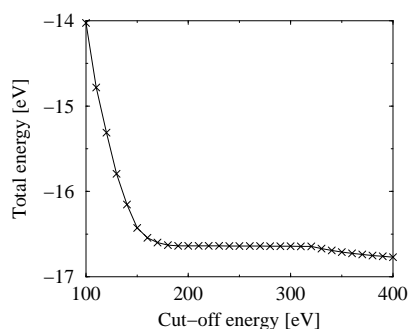


Figure 3.8 Convergence of total energy for SiC bulk with increasing cut-off energy.

Figure 3.9 Convergence of spectra of Si_5H_{12} with increasing cut-off energy.

NCs, a more powerful method is necessary which will be discussed in section 3.4.2. In any case, the chosen cell sizes were sufficient for the free crystallites to ensure reliable results.

3.2.4 Cut-off energies

In general, the “default cut-off” indicated in the PAW data sets has proven sufficient for the treatment of the respective materials. The values are 174 eV for Ge, 202 eV for C, and 207 eV for Si, i.e., 15 Ry, and 208 eV for H. Tests have shown that further increase did not result in any significant change in the spectra. An exception are the spin-polarized calculations which were done for the exchange splitting between the singlet and triplet excitons. Here, the cut-off was increased by 25 % to insure convergence of the very small energy differences. The quality of the cut-off is illustrated in Fig. 3.8. As can be seen, at the energies used in the present work, the calculation was well converged. A note of caution is in order, as also indicated by Fig. 3.8: An uncritical increase of the cut-off energy will not automatically lead to an increase of the quality of the results. Beyond 300 eV the results become questionable because of the PAW construction procedure. As for the spectra, the sufficiency of the chosen cut-off is demonstrated in Fig. 3.9.

3.3 Ionic Relaxations

The dependence of the total energy on the ionic coordinates discussed in section 2.1.6 enables the determination of the minimum-energy structure. The process is called ionic relaxation and can be done by means of three different methods. The choice depends on the system and on the progress of the relaxation. The methods we use are conjugate gradient, damped molecular dynamics [61], or, most frequently, the direct inversion in the iterative subspace (RMM-DIIS) [152, 153].

The choice of the relaxation algorithm depends on the system and also on the progress of the relaxation. Excited-state relaxations prove particularly difficult. This is illustrated in Fig. 3.10 where the **excited** (one electron-hole pair, spin neglected, no symmetry constraint) 41-atom Si cluster is treated. As can be seen, the choice of the algorithm is crucial. In the worst case, different algorithms may lead to different pathways on the Born-Oppenheimer surface and can lead into different local minima. This is seen in Fig. 3.10 as well.

The ionic relaxations are usually carried out until the target quantity of the calculation is converged. For this, it is not sufficient to stipulate a certain maximum residual force per atom.

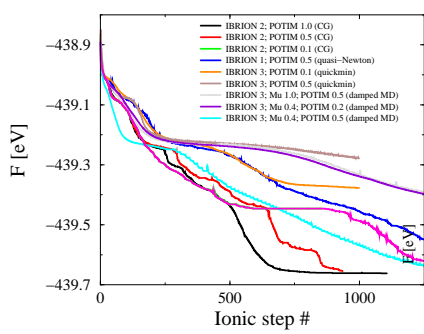


Figure 3.10 Non-spin-polarized calculation of $\text{Si}_{41}\text{H}_{60}$ with an electron-hole pair and no symmetry constraint. Performance of different relaxation algorithms, using the terminology of VASP tags [61]: IBRION=1: RMM-DIIS, 2: Conjugate gradient, 3: damped molecular dynamics.

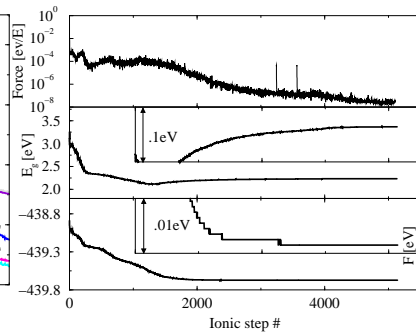


Figure 3.11 Convergence of ionic relaxation (IBRION=1: RMM-DIIS) for the same system as in Fig. 3.10: Overall forces, HOMO-LUMO gaps, and total energies. Note the very high number of ionic steps. The inserts are enlargements along the y -axis but keeping the x -axis.

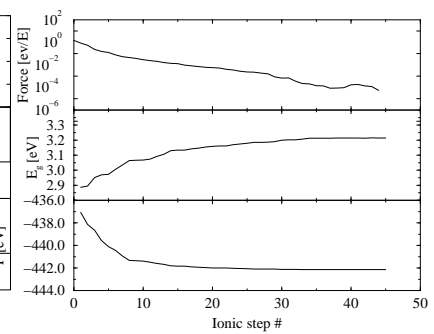


Figure 3.12 Same as Fig. 3.11, but for ground-state relaxation. Note the much lower number of ionic steps.

In particular, towards the end of the relaxation, the change in the HOMO-LUMO gaps can be much larger than the respective change in the total energy, as shown in the insets of Fig. 3.11.

However, the ground-state relaxations of our T_d systems proved relatively easy to accomplish and insensitive to technical parameters. This is, among other factors, due to the fact that the charge distribution is naturally also T_d . The number of relaxation steps is much smaller, as can be seen comparing Figs. 3.11 and 3.12.

3.4 Calculation of the Dielectric Function

In this section we describe the numerical details of the calculation of the dielectric function eq. (2.71), the density of states (DOS)

$$g(\varepsilon) = \sum_{\nu\mathbf{k}} \delta(\varepsilon - \varepsilon_{\nu}(\mathbf{k})) \quad (3.2)$$

and the joint density of states, (JDOS)

$$j(\varepsilon) = \sum_{c\nu\mathbf{k}} \delta\left(\varepsilon - (\varepsilon_c(\mathbf{k}) - \varepsilon_{\nu}(\mathbf{k}))\right). \quad (3.3)$$

For the hydrogenated NCs, the sum over all \mathbf{k} points in the supercell system's BZ can be trivially replaced by a multiplicative factor due to the absence of energy dispersion. The δ peaks can then be broadened to obtain spectra comparable to their experimental counterparts. The situation for the embedded systems is described in section 3.4.2.

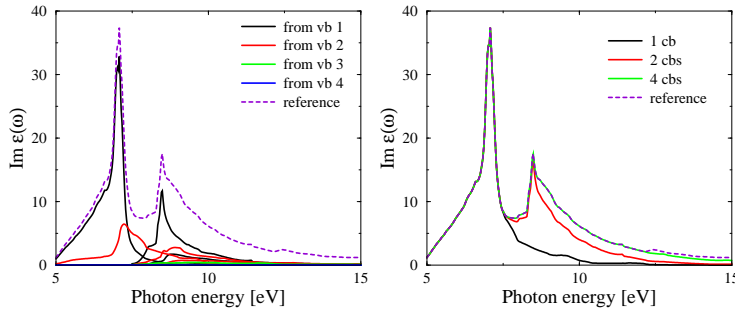


Figure 3.13 Contribution of transitions between single band pairs to spectra. (a) Transitions from the highest valence band into the first, second, third, and fourth CB (black), from the second highest VB etc. (red), from the third highest VB etc. (green), from the fourth highest VB etc. (blue), and reference (purple). (b) Summed transitions into the lowest four CBs from the first VB (black), the second VB (red), etc. The converged reference spectrum has been calculated using 100 cbs. All spectra calculated using the tetrahedron method with 89 tetrahedra in the IBZ.

3.4.1 Number of conduction bands

The numeric calculation of the dielectric function according to eq. (2.71) is done by truncating the sum over the conduction bands at a certain number. As no local-field effects are included, the dielectric function eq. (2.64) is simply a sum over all transitions. It turns out that already with a relatively small number of bands the spectra are relatively well described. In Fig. 3.13 a) the contribution of different band pairs is shown. As shown in Fig. 3.13 b), the lowest 4 conduction bands are already sufficient to account correctly for the spectrum of bulk SiC up to 12 eV. For the large supercells this number corresponds to a much higher number of bands. In general, we use for the calculation of the spectra as many valence bands as we use conduction bands. The total number of bands for the 216-atom bulk cell is 864, for the 512-atom bulk cell 2048. Yet even though this number of bands allows the calculation of the absorption spectrum, the calculation of integral properties which are sensitive to the whole spectral range is not necessarily equally satisfactory. An increase in the number of bands, however, would have been out of the range of the numerical resources available for the present work. It is for this reason that we have not considered any of the sum rules.

3.4.2 BZ integration: Tetrahedron method

For the embedded NCs, the calculation of the spectral properties, especially of the dielectric function according to eq. 2.65, the density of states (3.2), and the joint density of states (3.3), includes sums over all the \mathbf{k} points in the BZ. Unlike the electronic-structure discussed in section 3.2.3, where a relatively small number of \mathbf{k} points is sufficient, the spectra are very sensitive to the \mathbf{k} point sampling because they are determined primarily by the joint density of states (JDOS) and, therefore, by the band structure. Special-point techniques [156–158] can be used also here, but the number of \mathbf{k} points required to obtain converged results is rather high.¹

¹In the case of DFT-LDA, Ge bulk, at 2048 (shifted) \mathbf{k} points convergence is not yet reached [129].

For every \mathbf{k} point used, the electronic-structure calculation has to be carried through which leads to high numerical efforts. The problem is alleviated by the use of the tetrahedron method [159–161] which reduces the necessary number of \mathbf{k} points by about a factor of 10 [162, 163]. The method, which has been developed independently by Gilat and Raubenheimer [159] and Lehmann and Taut [160], is one of a group of methods which reduce the \mathbf{k} -space integrals to sums over surfaces of constant energy. Extrapolative [159, 164] and interpolative versions have been discussed [160, 161, 165–169]. The method can be used in 2 [170], 3, or 4 [171] dimensions and be modified when a Fermi surface is present [172]. Apart from the band structure, also the matrix elements of the integrand can be included [173].

The task to be accomplished is the calculation of an integral of the form

$$F(\omega) = \int_{\text{BZ}} f(\omega, \mathbf{k}) d^3\mathbf{k}. \quad (3.4)$$

The volume element in \mathbf{k} space can be written

$$d^3\mathbf{k} = dS \frac{d\varepsilon(\mathbf{k})}{|\nabla\varepsilon(\mathbf{k})|}, \quad (3.5)$$

where S is a surface of constant energy. This treatment can equally well be used for energy differences, $\varepsilon(\mathbf{k}) \leftrightarrow \varepsilon_{cv}(\mathbf{k}) = (\varepsilon_c(\mathbf{k}) - \varepsilon_v(\mathbf{k}))$, as they are needed in the dielectric function (2.71), where in addition f involves a sum over all valence-conduction-band pairs. Now the BZ is divided up into tetrahedra. Hence the integral (3.4) becomes a sum over all the tetrahedra γ ,

$$F(\omega) = \sum_{\gamma} \int d\varepsilon \int_{S_{\gamma}} dS \frac{d\varepsilon(\mathbf{k})}{|\nabla\varepsilon(\mathbf{k})|} f(\omega, \mathbf{k}). \quad (3.6)$$

Two approximations are now made. First, the band energies are linearized inside each tetrahedron,

$$\varepsilon(\mathbf{k}) := \varepsilon(\mathbf{k}_0) + \nabla\varepsilon(\mathbf{k}) \Big|_{(\mathbf{k}_0)} \cdot (\mathbf{k} - \mathbf{k}_0) \quad (3.7)$$

with a suitably chosen \mathbf{k}_0 and

$$\nabla\varepsilon(\mathbf{k}) \Big|_{(\mathbf{k}_0)} = \nabla\varepsilon(\mathbf{k}) \Big|_{\gamma} \quad (3.8)$$

constant for the tetrahedron γ . The gradient is obtained from the \mathbf{k} points and energies at the tetrahedron corners. The surfaces of constant energy are now planes.² Second, we assume that f in eq. (3.4) depends on \mathbf{k} only via $\varepsilon(\mathbf{k})$. In the case of the dielectric function this amounts to approximating the matrix elements as constant over any given tetrahedron. This turns the integral over S_{γ} into

$$\int_{S_{\gamma}} \frac{dS}{|\nabla\varepsilon(\mathbf{k})|} = \frac{A(S_{\gamma})}{|\nabla\varepsilon(\mathbf{k})|_{\gamma}}, \quad (3.9)$$

²The linearization is convenient but not necessary. A quadratic version of the tetrahedron method has been worked out by Methfessel and coworkers [174].

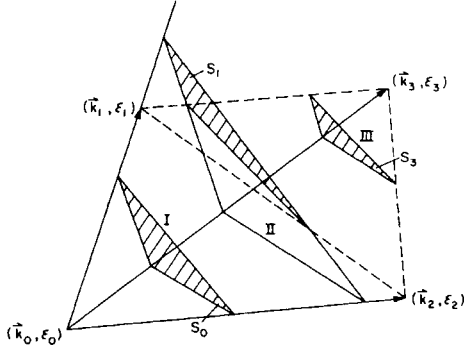


Figure 3.14 Schematic of one tetrahedron, with the corners \mathbf{k}_0 through \mathbf{k}_3 and the respective corner energies ε_i . The three possible positions of the surfaces S_i are shown.

where A is simply the area of S in the tetrahedron γ . Thus the dS_γ integral is reduced to the geometrical task of determining the surface area of the plane $S_\gamma(\varepsilon(\mathbf{k}))$ in the tetrahedron γ . Assuming a numbering of the corner \mathbf{k} points as indicated in Fig. 3.14 one finds that three situations have to be distinguished, as $S_\gamma(\varepsilon(\mathbf{k}))$ can be in any of the three positions S_1 , S_2 , and S_3 . The respective areas are given by

$$S_0(\varepsilon(\mathbf{k})) = \frac{[\varepsilon(\mathbf{k}) - \varepsilon_0]^2 V |\nabla \varepsilon(\mathbf{k})|}{2(\varepsilon_1 - \varepsilon_0)(\varepsilon_2 - \varepsilon_0)(\varepsilon_3 - \varepsilon_0)}, \quad (3.10)$$

$$S_1(\varepsilon(\mathbf{k})) = \frac{[\varepsilon(\mathbf{k}) - \varepsilon_1]^2 V |\nabla \varepsilon(\mathbf{k})|}{2(\varepsilon_1 - \varepsilon_0)(\varepsilon_3 - \varepsilon_1)(\varepsilon_2 - \varepsilon_1)}, \quad \text{and} \quad (3.11)$$

$$S_3(\varepsilon(\mathbf{k})) = \frac{[\varepsilon(\mathbf{k}) - \varepsilon_3]^2 V |\nabla \varepsilon(\mathbf{k})|}{2(\varepsilon_3 - \varepsilon_0)(\varepsilon_3 - \varepsilon_2)(\varepsilon_3 - \varepsilon_1)}. \quad (3.12)$$

The relevant S_2 is evidently given by $S_2 = S_0 - S_1$. The dS integration has now become an analytical expression only involving, besides $\varepsilon(\mathbf{k})$, the energies $\varepsilon_i = \varepsilon(\mathbf{k}_i)$ at the corners of the tetrahedron.³ The constant gradient is determined by the corner energies and the \mathbf{k} points themselves. V is the \mathbf{k} -space volume of the tetrahedron γ .⁴ All that's left now is to perform the energy integral in eq. (3.6). In the cases of interest for the present work, this is particularly simple because all three, the DOS (3.2), the JDOS (3.3), and the expression for the imaginary dielectric function (2.71) contain an “energy-conserving” δ function. Using an index function

$$\mathbf{I}_l = \begin{cases} 1 & \text{if } \varepsilon(\mathbf{k}) \text{ in region } l, \\ 0 & \text{else} \end{cases} \quad (3.13)$$

and the above-mentioned replacement $\varepsilon(\mathbf{k}) \rightarrow \varepsilon_{cv}(\mathbf{k})$ the final result for $\text{Im}\varepsilon(\omega)$ is

$$\text{Im}\varepsilon(\omega) = 48 \frac{e^2 \hbar^2}{2\pi} \sum_{\gamma \in \text{IBZ}} \sum_{cv} \bar{m}_\gamma^{cv} \int d\varepsilon^{cv}(\mathbf{k}) \sum_l \mathbf{I}_l \frac{S_l(\varepsilon(\mathbf{k}))}{|\nabla \varepsilon(\mathbf{k})|} \frac{\delta(\varepsilon^{cv}(\mathbf{k}) - \hbar\omega)}{[\varepsilon^{cv}(\mathbf{k})]^2} \quad (3.14)$$

$$= 48 \frac{e^2 \hbar^2}{2\pi} \sum_{\gamma \in \text{IBZ}} \sum_{cv} \bar{m}_\gamma^{cv} \sum_l \mathbf{I}_l \frac{S_l(\varepsilon(\mathbf{k}))}{|\nabla \varepsilon(\mathbf{k})|} \frac{1}{(\hbar\omega)^2} \quad (3.15)$$

³The formulae are modified when degenerate tetrahedron corners are considered, cf. section 3.4.4.

⁴Customarily, the volumes of all the tetrahedra are chosen to be equal. This is not, however, a requirement of the method.

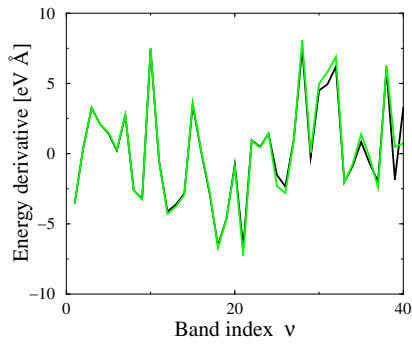


Figure 3.15 Test of matrix elements by comparing the gradient from the matrix elements eq. (3.18), to one calculated from band energies at close \mathbf{k} points.

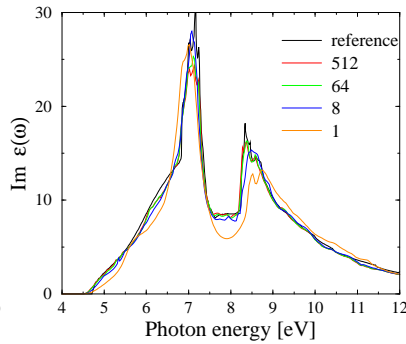


Figure 3.16 Spectra obtained using different resampling densities as indicated (=number of tetrahedra in IBZ).

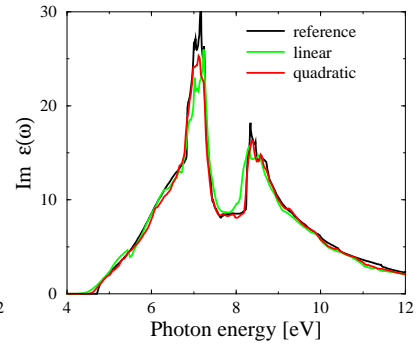


Figure 3.17 Spectra obtained using linear and quadratic extrapolation according to eq. (3.17).

where averaged oscillator strengths

$$\bar{m}_\gamma^{cv} = \frac{1}{4} \sum_{i=1}^4 \left[\frac{1}{3} \sum_{i_{\text{dir}}=1}^3 \left| f_{ii}^{cv}(\mathbf{k}) \right| \right] \quad (3.16)$$

have been introduced, cf. eq. (2.74). The first sum averages over the 4 tetrahedron corners, while the second sum yields the invariant for the cubic case. Hence we do not calculate the tensor $\varepsilon_{\alpha\beta}(\omega)$ of eq. (2.71) but its invariant trace $\sum_\alpha \frac{1}{3} \varepsilon_{\alpha\alpha}(\omega)$, $\alpha \in \{x, y, z\}$ [175]. The factor 48 in eq. (3.14) has been introduced here because we can in the cubic system restrict the integration to the irreducible part of the BZ (cf. section 3.4.4).

3.4.3 Extrapolation

It is obvious from the above formulae that the method relies on the allocation of the band energies at different \mathbf{k} points to individual bands. However, the electronic-structure calculations do not yield bands but merely stacks of energies at single \mathbf{k} points. While this problem is already present in the calculations for bulk materials using small unit cells, it is drastically aggravated when very large cells are used as in the present work. This is for two reasons: First, there are, after the multiple band foldings, many bands per energy interval, and band crossings are not uncommon. Second, due to the large cells and the high number of bands, any increase in the number of \mathbf{k} points is numerically very costly, independently of the fact that the calculations do not have to be carried out simultaneously.⁵ The tiny separations of the energy values due to the huge number of bands within the supercell description and the occurrence of band crossings and anticrossings make apparent that the idea of band allocation at different \mathbf{k} points and, hence, also any interpolative methods have to be abandoned.

We have developed, in the present work, an approach to both solve this problem and at the same time require the minimal number of \mathbf{k} points possible, viz., just one. An extrapolative

⁵This holds for the band-structure calculations and the accompanying matrix element calculations only, not for the determination of the charge density.

version of the tetrahedron method [159, 166, 176, 177] has been implemented [178]. To obtain the energy values of the bands for one tetrahedron we start from some \mathbf{k}_0 and extrapolate, essentially by means of $\mathbf{k} \cdot \mathbf{p}$ perturbation theory. Basically the formula we use is

$$\begin{aligned} \varepsilon_\nu(\mathbf{k}) &= \varepsilon_\nu(\mathbf{k}_0) + \sum_{\alpha=1}^3 \frac{\partial}{\partial k_\alpha} \varepsilon_\nu(\mathbf{k}) \Big|_{\mathbf{k}_0} (k_\alpha - k_{0\alpha}) \\ &+ \sum_{\alpha,\beta} (k_\alpha - k_{0\alpha})(k_\beta - k_{0\beta}) \frac{\partial^2}{\partial k_\alpha \partial k_\beta} \varepsilon_\nu(\mathbf{k}) \Big|_{\mathbf{k}_0}, \end{aligned} \quad (3.17)$$

with the gradients of the energy bands represented by the intraband matrix elements of the momentum operator at \mathbf{k}_0 ,

$$\frac{\partial}{\partial k_\alpha} \varepsilon_\nu(\mathbf{k}) \Big|_{\mathbf{k}_0} = \frac{\hbar}{m} \langle \nu \mathbf{k}_0 | p_\alpha | \nu \mathbf{k}_0 \rangle, \quad (3.18)$$

calculated according to eq. (2.81). The second derivatives are given by

$$\frac{\partial^2}{\partial k_\alpha \partial k_\beta} \varepsilon_\nu(\mathbf{k}) = \frac{\hbar^2}{m} \left\{ - \sum_{\nu'} f_{\nu\nu'}^{\alpha\beta}(\mathbf{k}) + \delta_{\alpha\beta} \right\} \quad (3.19)$$

with the oscillator strengths $f_{\nu\nu'}^{\alpha\beta}(\mathbf{k})$ of equation (2.74). Due to the use of nondegenerate $\mathbf{k} \cdot \mathbf{p}$ theory we have to use a \mathbf{k}_0 point that does not give rise to degenerate states. Thus \mathbf{k}_0 must not lie on a symmetry plane or line. For this reason, in the simple-cubic case the Baldereschi point [156] cannot be used. We use the center of gravity of the IBZ, which is itself a tetrahedron, as the \mathbf{k}_0 point. In reciprocal coordinates this is the point $\mathbf{k}_0 = (.250, 0.125, 0.375)$.

The quality of the calculations depends sensitively on the accuracy of the intra- and inter-band momentum matrix elements used within the extrapolation procedure. In order to demonstrate the precision of the calculations within the PAW method [139, 141] we study the numerical fulfillment of the relation between the intraband momentum matrix elements and the gradient of the corresponding Bloch band in \mathbf{k} space, eq. (3.18). A comparison of derivatives obtained from these gradients to derivatives from energy differences at two \mathbf{k} points in close vicinity is shown in Fig. 3.15. The test has been performed for the center of gravity of the tetrahedron, $\mathbf{k}_0 = (0.25, 0.125, 0.375)$, lying between $\mathbf{k}_1 = (0.25073, 0.12514, 0.37536)$ and $\mathbf{k}_2 = (0.4927, 0.12486, 0.37464)$, in units of the reciprocal basis vectors of the 8-atom simple-cubic SiC cell which has been used. Obviously the quality of the intraband matrix-element calculation is excellent.

3.4.4 Resampling – tetrahedron mesh

After we have availed ourselves with an approximate band structure as calculated by means of eq. (3.17), the usual procedure can be employed. In principle, the quadratic representation of the band structure around some \mathbf{k}_0 allows the application of the analytic quadratic tetrahedron method [174]. However, in view of the errors incurred from our extrapolation, the effort necessary to implement the quadratic method, and the existence of a code and expertise about the linear method we retain the linear method.

In order to diminish the obvious problem of committing the systematic error of linearly interpolating a quadratic function between two fairly distant points in \mathbf{k} space we introduce a resampling procedure. We divide the irreducible part of the BZ into smaller tetrahedra by choosing the midpoints of the tetrahedron edges and connecting them to obtain smaller tetrahedra. Successive application of this method yields tetrahedron meshes of 1, 8, 64, 512, and 4096 tetrahedra. The energies at their corners are calculated according to expression (3.17). The matrix elements according to eq. (3.4.2) are calculated at \mathbf{k}_0 and held constant for all the IBZ for any pair of bands $\{c, v\}$. For a refinement of this procedure see section 3.4.7. Resulting spectra are shown in Fig. 3.4.4 for SiC in a 216-atom cell. There is clearly an improvement of the absorption spectrum with increasing number of tetrahedra. The use of 512 tetrahedra produces already a converged result. Further subdivision of the tetrahedra does not lead to further improvement. Apart from the finestructure of the two main absorption peaks, the 512-tetrahedra result already approaches the reference spectrum. It should be noted that the “sampling” using just one tetrahedron – crude though it is – leads already to qualitatively correct results because due to the folding it is equivalent to many more tetrahedra in the corresponding smallest supercell (8 atoms). For the 512-atom cell, the IBZ corresponds to 64 tetrahedra in the 8-atom cell.

The question arises which supercell sizes our method is applicable to. The larger the real-space cell, the smaller is the BZ, and, consequently, the shorter are the extrapolation distances in \mathbf{k} space. The SiC results are shown in Fig. 3.22 for supercells containing 8, 64, 216, and 512 atoms, respectively. In all cases a 64-tetrahedra resampling has been employed. It is apparent that for the 8-atom cell the extrapolation distances are as large as to only allow a representation of the main features of the optical absorption spectrum in a crude manner. The method works much better in the 64-atom cell, although in this case it is still rather far from convergence. For the two largest cells under consideration the method gives a more or less well converged absorption spectrum. In the largest cell with 512 atoms the spectrum is in excellent agreement with the reference result, apart from a small underestimate of the heights of the main absorption peaks.

The subdivision of \mathbf{k} space into tetrahedra needs to be done with some care. Very often – and also in the present work – one takes simply the IBZ and introduces some convenient subdivision. However, it has been pointed out by Kleinman [179] that this necessarily results in giving uneven weights to different \mathbf{k} points. Subsequently, several publications have discussed ways of solving this problem [179–182]. Jepson and Anderson [180] suggested to divide not the IBZ but the whole BZ into tetrahedra, using the same \mathbf{k} points as before (and points equivalent to them). While this approach solves the weight problem, it introduces a new complication, which is not, apparently, discussed in the literature: The tetrahedron mesh now necessarily includes tetrahedra with symmetry-equivalent corners. These can be treated using the limits of Ren and Harrison [183] of the expressions (3.10), (3.11), and (3.12) for corners of equal energies. However, while these limits are useful for the case of accidentally degenerate corner energies, the solution of the problem is unsatisfactory for equivalent-cornered tetrahedra which will have many occasions of multiple degeneracy (or approximate degeneracy). We demonstrate this problem for the use of just one tetrahedron, the simple-cubic IBZ itself.

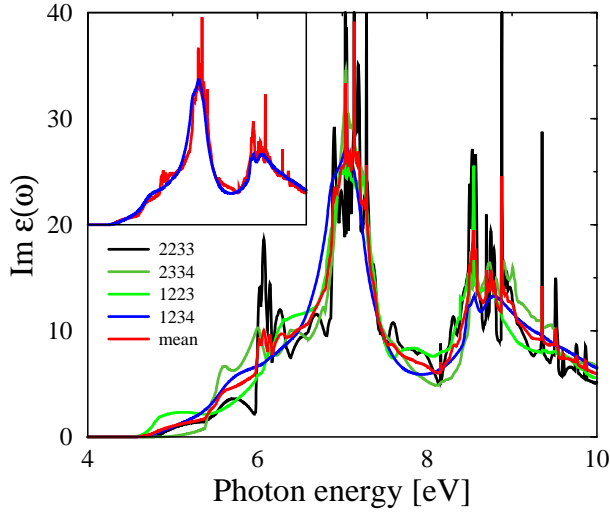


Figure 3.18 Spectra for the different tetrahedra using the whole BZ as described in the text. The fact that the results for the different tetrahedra are different in general is due to the fact that the single tetrahedra here do not comprise the whole IBZ but rather parts of it (and some of them more than once).

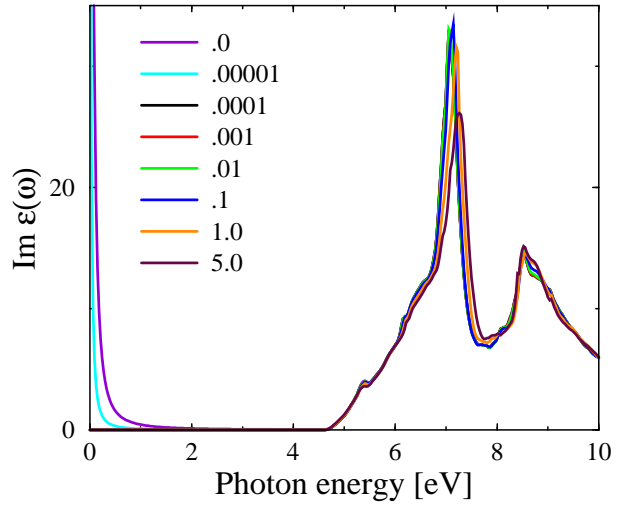


Figure 3.19 Spectra for different values of the parameter used for carrying out the principal-value integral. For SiC, 512-atom cell bulk, the spectra do not appreciably change over the range .0001 through 1.

The smallest possible number of inequivalent tetrahedron corners for the simple cubic BZ is four, viz. Γ (1), the midpoints of the faces (2), the midpoints of the edges (3), and the corners (4). In order to get a correct weight for every \mathbf{k} -point and to cover the whole BZ one has to consider the four tetrahedra 1234, 1223, 2334, and 2233. The problem occurs most strongly for the 2233 tetrahedron with its two doubly degenerate corner energies. The energy $\varepsilon(\mathbf{k})$ always lies between the second and the third corner energy. The formula for S_2 for degenerate ε_3 and ε_2 is [183],

$$S_2 \propto \frac{(\varepsilon(\mathbf{k}) - \varepsilon_0)}{(\varepsilon_2 - \varepsilon_0)(\varepsilon_3 - \varepsilon_0)} \left(\frac{\varepsilon_2 - \varepsilon(\mathbf{k})}{\varepsilon_2 - \varepsilon_0} + \frac{\varepsilon_3 - \varepsilon(\mathbf{k})}{\varepsilon_3 - \varepsilon_0} \right). \quad (3.20)$$

For the tetrahedron which has a second pair of degenerate corners, and looking at the contribution at $\varepsilon(\mathbf{k}) = \frac{1}{2}(\varepsilon_2 - \varepsilon_1)$ this reduces to a term proportional to $1/[\varepsilon_2 - \varepsilon_1]$. If ε_2 and ε_1 happen to be close in energy as well, the contribution of this tetrahedron becomes very large within a small energy range.

The consequence of this is shown in Fig. 3.18. While the tetrahedron representing the IBZ fares well because it does not have symmetry-degenerate corners, there are spikes in the curves of the others which also translate into the mean which should represent the “true” result.

The physical explanation of this behavior is that the tetrahedron is intersected by symmetry planes. There the band gradients have to vanish in the direction perpendicular to the plane. However, in the case of the degenerate tetrahedron corners the linear interpolation maps this behavior by bands running parallel in the direction connecting the two degenerate points. For the case of two pairs of degenerate corners where also the separation of these becomes very small, this is tantamount to smearing a critical point out onto the whole plane within the tetrahedron.

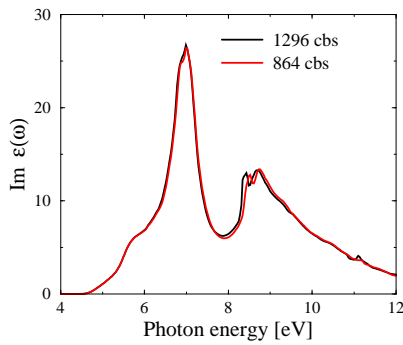


Figure 3.20 Influence of the number of bands considered in the $\mathbf{k}\cdot\mathbf{p}$ expression. The number of bands (as indicated) has been changed only for the extrapolation; the calculation of the spectrum has been done using the same number in both cases.

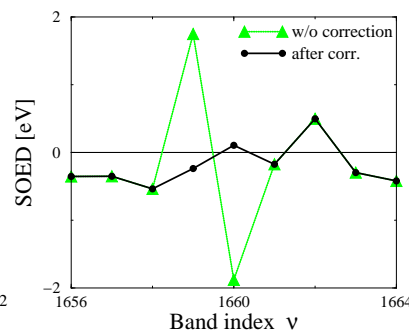


Figure 3.21 Correction of the “kissing” problem in the extrapolation. The second-order energy term is shown before and after the correction.

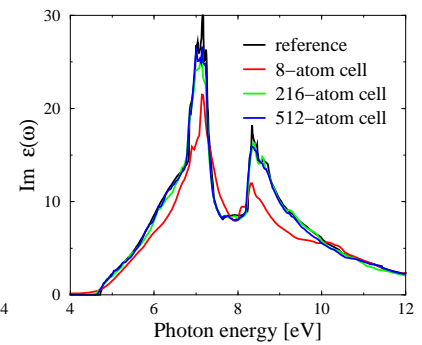


Figure 3.22 Spectra calculated using the extrapolation & tetrahedron method developed in the present work and applied to the different simple-cubic cell sizes.

Thus the problem is caused by the linearization of the band energies inside each tetrahedron, and it cannot be solved without changing this.

The weight problem due to the use of just the IBZ is limited to the \mathbf{k} points at the surface of the IBZ because all points inside occur just as many times as there are symmetry operations. Thus the problem vanishes in the limit of large tetrahedron numbers. Moreover, our tests have shown that the number of tetrahedra needed in order to reproduce the reference spectrum is not very large, cf. section 3.4.4. For that reason we have, after due consideration of this weight problem, chosen to keep using a subdivision of only the IBZ.

A comparison of the results after linear and quadratic extrapolation of the band energies is shown in Fig. 3.17. The poorer quality of the results after only linear extrapolation may be understood by the fact that at critical points the bands’ gradients are zero. The linear extrapolation starting from a general \mathbf{k}_0 overshoots here.

The method could be improved by starting from more than just one \mathbf{k} point in the BZ and extrapolate the bands to the different tetrahedron corners of a particular resampling mesh. For the purposes of the present work extrapolation was deemed sufficient. Besides, it should be noted that in this case, the bands used for the integration will not be continuous inside the IBZ. If the improvement just mentioned were to be implemented, a thorough test of the influence of that on the final results would be necessary.

3.4.5 Band kissing / Anticrossing correction

For the large-supercell systems the energies lie so dense that the sum over bands in the the second-order expansion of the energy bands (3.17), (3.19) and (2.74) effectively becomes an integral. In fact, the energy separations are frequently smaller than the precision of the energies. The sum can be replaced by an integral in the sense of the Riemann definition. The principal value is computed in practice by adding a small imaginary part $i\eta$ to the energy nominator and considering the real part. It turns out that the method is fairly insensitive with respect

to the choice of the parameter η . Between the two extremes where either the second-order energy terms scatter strongly due to a too small η , or the result starts losing structures due to a too large η , there is a rather wide region for the broadening parameter over which the result does not change appreciably. Our experience indicates that it is best to choose the parameter as small as possible but without a singular tail arising towards $\hbar\omega = 0$ due to a scatter of the extrapolated energies. The latter effect is due to the small energy differences between the band energies that enter in eq. (2.74), which are frequently smaller than the accuracy of the electronic-structure calculation. Reliable values of η are $\eta = 0.001\text{eV} - 0.1\text{ eV}$ for 216-atom cells and $\eta = 0.00001\text{eV} - 0.01\text{ eV}$ for 512-atom cells. For embedded NCs, the values have to be chosen somewhat larger. An example of the procedure is shown in Fig. 3.19.

The accuracy of the second-order expansion of the energy bands (3.17) and (2.74) depends on the number of conduction bands as well. Apart from the influence on the spectra as discussed in section 3.4.1, the number of bands influences the convergence of the perturbation series in expression (3.19). The “repulsion of the bands” due to their interaction requires, for each band considered, the inclusion of a reasonable number of bands above. Consequently, for the higher bands the second-order energy correction will be less accurate than for the lower ones, and the resulting error will be systematic. Figure 3.20 shows that this is really the case. The same calculation has been done for different numbers of conduction bands taken into the perturbation sum in eq. (3.19). However, for the calculation of the absorption in both cases the same number of bands were used. For the higher number of included bands the high-energy absorption peak slightly changes its location towards the reference value.

There is another point of importance. Perturbation theory requires the energy corrections to be smaller than the difference of the involved unperturbed energy levels. For the large extrapolation distances ($\mathbf{k} - \mathbf{k}_0$) that we have to deal with, this condition is poorly fulfilled, at best. In this sense we have to state clearly that by means of equation (3.17) we do not, strictly speaking, calculate a well-defined perturbative expansion but rather a geometrical extrapolation from the first and second derivatives of the energy bands at \mathbf{k}_0 . Thereby we do heavily rely on the smooth behavior of the bands. In other words, viewed as a perturbative calculation the convergence properties could not be assured. However, our results clearly indicate the viability of extrapolation in the face of this problem. Nevertheless, we have to discuss the question as to how well even exact second-order extrapolation can describe the bands, i.e., how dangerous is it for a particular band to drop the basic requirement of perturbation theory? This problem is exemplified by what Pickard and Payne call “band kissing” [176], also known as anticrossing. The effect occurs when two bands which would truly intersect each other are “repelled” by their interaction. This repulsion causes extreme values of the second-order energy derivatives for the respective two bands which are limited to the immediate vicinity of the anticrossing. If \mathbf{k}_0 happens to be very close to such a point, the second-order energy corrections to the two bands will be much too large, similar in value, and have opposite signs [176]. This can be seen in Fig. 3.17 where the second-order energy correction is plotted as a function of the band index. In the simplest possible case of just two bands, the problem can be solved by using $\mathbf{k}\cdot\mathbf{p}$ theory for almost degenerate bands [184] and crossing the bands “by hand” by an assignment of the new energy values such that smooth, crossed bands are obtained. We found that it is possible to

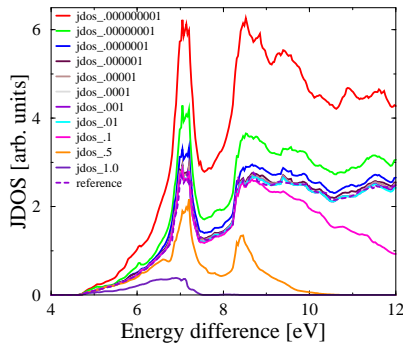


Figure 3.23 Joint density of states calculated for the 512-atom SiC supercell and using different cut-offs on the oscillator strengths as indicated. No appreciable change occurs between 10^{-2} and 10^{-6} .

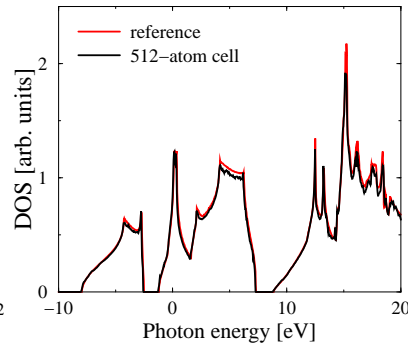


Figure 3.24 Density of states, calculated for the 512-atom SiC sc supercell using quadratic extrapolation and the method described in the text.

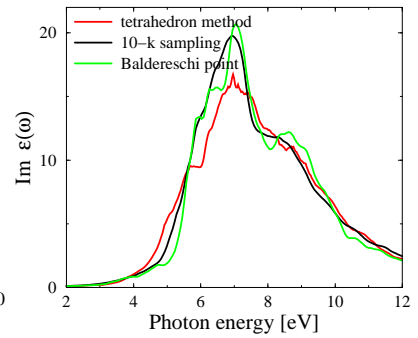


Figure 3.25 Application of the extrapolative method to a 41-atom Ge NC embedded in SiC, 216-atom supercell. Comparison with a one- \mathbf{k} spectrum using the Baldereschi point, and a 10- \mathbf{k} sampling using Monkhorst-Pack \mathbf{k} points.

look for extreme values of the second-order energy terms which are close in terms of the band indices and similar in size but have different signs. We only check those for the direction of highest curvature and apply the method of Pickard and Payne [176] to them: First, the direction is found in which the second-order energy term is diagonal. The system is then rotated, and new energies are calculated using second-order perturbation theory for nearly degenerate states [184]. Now the bands are crossed “by hand”. Finally the system is rotated back into the original coordinate system.

The result of such a treatment is also demonstrated in Fig. 3.17. However, at least in the cases we considered, the band-kissing effect on the overall result is negligible. Within the precision of our calculations the correction can safely be neglected.

As a further demonstration of the quality of the extrapolation method starting from only one \mathbf{k}_0 point we calculate the DOS of SiC in the 512-atom cell with a 64-tetrahedra resampling. This is a very good indicator of the quality of the energy extrapolation because it involves only the energies, but not the transition matrix elements. It is clearly demonstrated in Fig. 3.2 that our method of using only one \mathbf{k}_0 point in the IBZ is capable of yielding excellent results for spectral properties.

3.4.6 Spurious transitions

In general, as a consequence of the fact that states belonging to different \mathbf{k} points in the BZ of the initial structure are folded onto the same \mathbf{k} point, spurious optical transitions occur. These transitions are, however, strictly forbidden in the BZ of the ideal crystal. The number n_{spurious} of spurious transitions in relation to the real ones n_{real} is easily seen to be $n_{\text{spurious}}/n_{\text{real}} = n_{\text{cb}}n_{\text{vb}}16N^3$ where n_{cb} and $n_{\text{vb}} = 4$ are the numbers of conduction bands and valence bands related to the initial primitive cell of the fcc structure. Although the respective transition probabilities vanish, there had been some concern whether the numerically non-zero transition probabilities due to inaccuracies might create a computational problem. We found that the values of the transi-

tion matrix elements of a typical spurious transition is smaller by a factor of 10^{-6} than those representing real transitions. Thus, for the supercells considered in the present work one can ignore the influence of spurious transitions. However, it should be kept in mind for the future application of the method to even larger supercells.

This has been supported also by a discussion of the JDOS which allows us to separate the influence of the matrix elements and energies. While the meaning of the DOS is and remains clear, the JDOS incurs arbitrariness in the case of large supercells, i.e., a nonprimitive unit cell. Depending upon how often the BZ has been folded, the JDOS fully counts the spurious transitions, i.e., seemingly direct transitions which, however, represent transitions between states at different points of the BZ before folding. They do not influence the computation of the dielectric function because the contribution of each optical transition in eq. (2.72) is weighted by the oscillator strength $f_{cv}^{\alpha\alpha}(\mathbf{k})$ of expression (2.74). On the other hand, the spurious transitions count fully for the JDOS. Therefore, as long as one does not restrict the treatment to primitive unit cells, one is faced with ambiguity in the JDOS treatment. The problem persists as long as one considers supercell arrangements without any disturbance of the ideal crystal structure. While the physical properties approach those of the pure bulk material, the JDOS obviously does not. It is clear from that argument that the JDOS is not to be counted among the observable quantities like the DOS and the dielectric function.

This raises the question if there is a way to recover the original "true" JDOS of the ideal crystal from the supercell description. To achieve this, one has to disregard those spurious transitions. As the parameter to decide whether or not a contribution of an electron-hole pair at a certain \mathbf{k} point is to be counted for the JDOS we insert the requirement that the oscillator strength of a given transition is larger than some cutoff strength f_0 . Results for SiC are shown in Fig. 3.3 where the JDOS calculated for a two-atom cell is compared to that from the 512-atom cell. Evidently the procedure has at least some merit. There is a broad region of the cutoff parameter for which the spectra do not change remarkably.

3.4.7 Matrix element extrapolation

Until now, we have taken the transition matrix elements according to eq. (2.81) at \mathbf{k}_0 and assumed them constant over the IBZ for a fixed band pair. To refine this treatment we need the matrix elements at all the tetrahedron corners. According to the $\mathbf{k}\cdot\mathbf{p}$ -perturbative representation, the wave functions at \mathbf{k} can be extrapolated using only the momentum matrix elements at \mathbf{k}_0 . These are the same matrix elements which occur in the equation of the dielectric function eq. (2.71) and in the energy extrapolation eq. (3.17) and have been calculated anyway. Thus we can calculate the matrix elements of the momentum operator at the tetrahedron corners using the first-order $\mathbf{k}\cdot\mathbf{p}$ -perturbed states

$$|v\mathbf{k}\rangle^1 = |v\mathbf{k}_0\rangle + \frac{\hbar}{m}(\mathbf{k} - \mathbf{k}_0) \cdot \left\{ \sum_{\mu \neq \nu} \frac{\langle \mu\mathbf{k}_0 | \mathbf{p} | v\mathbf{k}_0 \rangle}{(\varepsilon_\nu(\mathbf{k}_0) - \varepsilon_\mu(\mathbf{k}_0))} |\mu\mathbf{k}_0\rangle \right\}. \quad (3.21)$$

In this way (neglecting second-order terms in \mathbf{k}) the first-order matrix elements at the corners are expressed as sums of momentum matrix elements at \mathbf{k}_0 ,

$$\begin{aligned}
{}^1 \langle \nu \mathbf{k} | \mathbf{p} | \mu \mathbf{k} \rangle^1 &= \langle \nu \mathbf{k}_0 | \mathbf{p} | \mu \mathbf{k}_0 \rangle \\
&+ \frac{\hbar}{m} (\mathbf{k} - \mathbf{k}_0) \cdot \left\{ \sum_{\lambda \neq \nu} \frac{\langle \lambda \mathbf{k}_0 | \mathbf{p} | \nu \mathbf{k}_0 \rangle}{(\varepsilon_\mu(\mathbf{k}_0) - \varepsilon_\lambda(\mathbf{k}_0))} \langle \nu \mathbf{k}_0 | \mathbf{p} | \lambda \mathbf{k}_0 \rangle \right\} \\
&+ \frac{\hbar}{m} (\mathbf{k} - \mathbf{k}_0) \cdot \left\{ \sum_{\gamma \neq \nu} \frac{\langle \gamma \mathbf{k}_0 | \mathbf{p} | \nu \mathbf{k}_0 \rangle^*}{(\varepsilon_\nu(\mathbf{k}_0) - \varepsilon_\gamma(\mathbf{k}_0))} \langle \gamma \mathbf{k}_0 | \mathbf{p} | \mu \mathbf{k}_0 \rangle \right\}.
\end{aligned} \tag{3.22}$$

Again the sum over the bands has to be treated as a principal-value integral as discussed in section 3.4.5. The variation of the matrix elements can now be included into the method using the formulas of Ren and Harrison [183] or by using different averaged values for the different tetrahedra after the resampling procedure. Otherwise, the advantage of the better description at the corners is lost because the linear inclusion of matrix-element variations amount to averaging in the case when \mathbf{k}_0 lies at the center of the region under consideration.

We included the matrix elements in this way but found that this does not change the results for the optical absorption appreciably. Since it is very time consuming (due to the triple sum over all bands), and in view of the quality of the results without it, we conclude that for practical purposes it is reasonable to dispense with the extrapolation of the matrix elements. Any further effort to refine the method should be directed at the band structure, not at the matrix elements.

3.5 Results for Constituents

In order to relate the results of our NC calculations to the properties of the NC's constituents we review briefly the results that our numerical setup yields for the pure materials of which we compose our nanostructured systems. Using the PAW data sets we obtain theoretical lattice constants as indicated in table 3.5. At the theoretical lattice constants the band structures as shown in Fig. 3.26 and 3.27 are obtained with the gaps as indicated in table 3.5. The lattice constants are, as usual in LDA, slightly underestimated. The gaps exhibit the DFT-LDA underestimate as discussed in section 2.2.1.

The calculations treating the nanocrystals rely necessarily on the relaxed structures. For that reason, and unlike in the treatment of bulk spectra, there is no possibility to decide between using the theoretical or the experimental lattice constants. The values given here are, consequently, obtained for the bulk materials at their theoretical lattice constants. Apart from the closing of the gap, germanium is particularly interesting because the small difference between the experimental and the theoretical lattice constant can – in LDA – induce the change between direct- and indirect-gap behavior [129].

In Fig. 3.26 and 3.27 the band structures of the materials which the nanostructures are composed of are shown. Two situations are treated: The theoretical lattice constant and, for

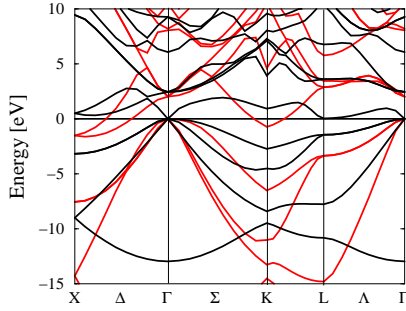


Figure 3.26 Band structure of Ge obtained with the present numerical setup. Shown are the bands at the theoretical lattice constant (black), as well as at the SiC lattice constant (red), corresponding to very high compressive strain.

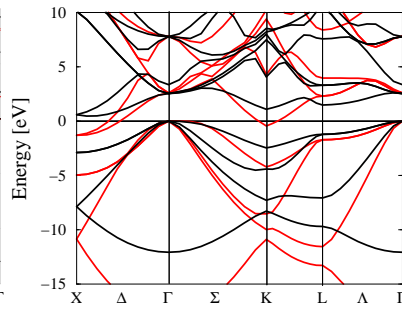


Figure 3.27 Same as Fig. 3.26 for Si.

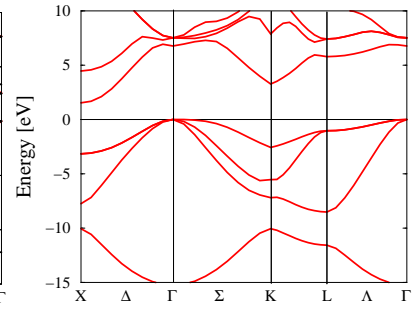


Figure 3.28 Band structure for SiC obtained using the theoretical lattice constant.

	Lattice constants		Indir. gap		Γ-Γ gap	
	LDA-PAW	Experiment	LDA-PAW	Experiment	LDA-PAW	Experiment
Ge	5.647 Å	5.658 Å	0.31 eV (Γ-L)	0.76 eV	0.	0.80 eV
Si	5.404 Å	5.431 Å	0.47 eV (Γ-Δ)	1.17 eV	2.54 eV	4.18 eV
SiC	4.330 Å	4.360 Å	1.55 eV (Γ-X)	2.42 eV	6.74 eV	6.00 eV

Table 3.1 Theoretical values compared to experimental results from Ref. [185]

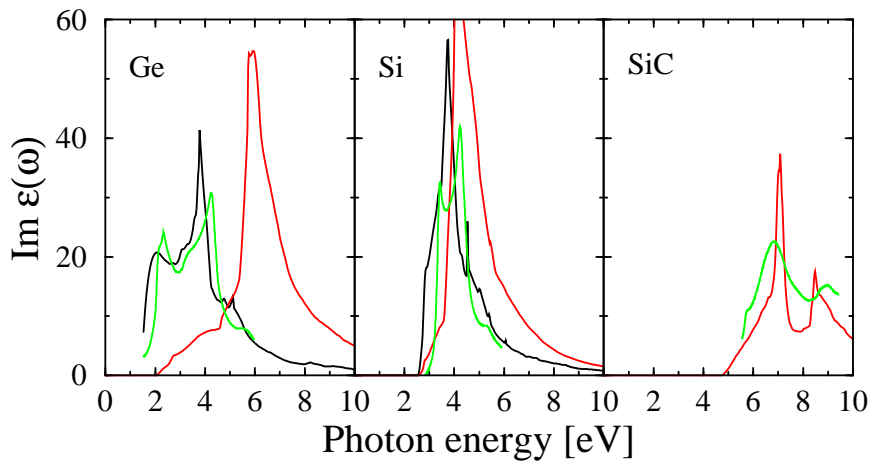


Figure 3.29 Imaginary part of the dielectric function of the materials which have been used for the modeling of the NCs. Shown are again the results calculated using the equilibrium lattice constant (black) and, second, the spectra of the material compressed to the SiC lattice parameter (red). Experimental results (green) are from Ref. [21] (Ge) and (Si), and Ref. [186] (SiC).

comparison, the SiC lattice constant. This is due to the fact that both the Si and the Ge are treated embedded in SiC, which in our model (see. section 3.1) means that they are strongly compressed.

Similarly, in Fig. 3.29 the spectra obtained for the respective bulk materials are shown along with experimental results. For a thorough discussion of the differences see Refs. [162] and [139] which present results obtained by roughly the same numerical “set up”. It should be noted that the shift between the DFT-LDA spectra and the experimental spectra is smaller than the shifts expected due to the quasi-particle correction Δ as discussed in section 2.2.1. According to Ref. [162] this may be attributed to the neglect of excitonic effects as well as to the use of the theoretical lattice constants. Moreover, the strong underestimate of the E_1 peak especially in Si is due to neglecting excitonic effects. Further effects contributing to the differences are local-field effects which are neglected in our theoretical results, as well as the limited resolution of the measurements.

Chapter 4

Results

4.1 Free, H-terminated Nanocrystals

4.1.1 Structure and importance of relaxation

Relaxation starting from the ideal bulk fragments as described in section 3.1 changes the bond lengths and bond angles; no bonds are broken. The average bond lengths are shown in Fig. 4.1 as a function of the NC diameter. Here and in the following we focus on the Ge-Ge and Si-Si bonds but disregard the Ge-H and Si-H bonds of the hydrogen saturation. For the ground-state geometry, the average bond lengths are consistently shorter than the respective bulk values. Similar contraction effects have been observed experimentally in porous silicon [187] and in Ge NCs [188]. The theoretical study of Pizzigalli *et al.* [189] agrees roughly with our findings. However, under oxygen exposure this contraction turns into an expansion [187]. The effect is obviously dependent on the surface saturation. Annealing of porous silicon also leads to nanostructured Si with shortened bonds [190]. It has traditionally been explained as a consequence of the surface stress [187], but our results show that this cannot fully account for the effect. The effect is much stronger in the Ge than in the Si NCs. While the average Si interatomic distances have already reached their bulk limit for NCs with diameters of about 20 Å, the bond-length reduction is still substantial (0.35%) for Ge NCs of the same size.

For the excited-state geometry calculated with an electron-hole pair in the crystallite but keeping T_d symmetry, the situation is more complex. The picture suggests that there might be two mutually counteracting effects on the bond lengths in Fig. 4.1. The first one is the general bond-length reduction as for the ground state. The second, however, is a tendency of increasing bond lengths with electronic excitation, increasing with decreasing NC size. For the Ge NCs, this leads to a consistent picture. For Si, however, the results with respect to the excitation effect are not so uniform. This might be partly due to the stronger bonds in Si as compared to Ge. Moreover, the symmetry of the LUMO state in the Si NCs is different from that of the Ge NCs, reflecting the strong contributions from the X points of the bulk Si band structure. Thus the symmetry of the lowest pair excitation and, hence, its effect on the structural relaxation, is different in Ge and Si NCs. Special care has to be taken in the discussion of the results for the smallest NCs of 5 and 17 atoms. These represent molecule-like structures rather than

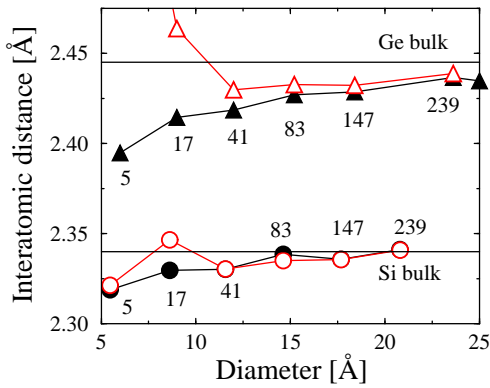


Figure 4.1 Interatomic distances in the Ge (triangles) and in the Si (circles) NCs. Filled symbols: ground-state results, empty symbols: results of the (T_d) relaxation with one electron-hole pair present. The numbers of Ge (Si) atoms in the crystallites are indicated. The horizontal lines show the calculated bulk interatomic distances.

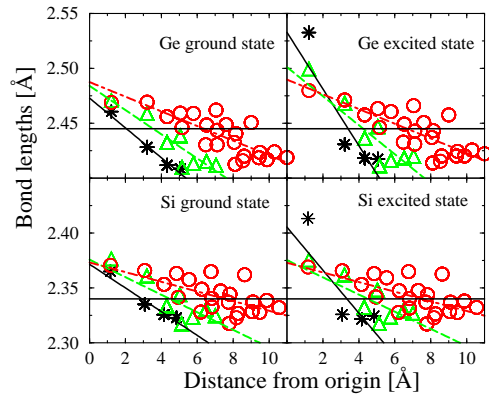


Figure 4.2 Individual bond lengths in the NCs plotted against the distance from the center. Asterisks: 41-atom NCs, triangles: 83-atom NCs, circles: 239-atom NCs. The linear fits are given in the respective colors. The horizontal lines are the calculated bulk interatomic distances.

NCs and might be governed by completely different mechanisms [189] which can change their symmetry entirely [191]. In the present work we have always kept the T_d symmetry constraint, except where indicated otherwise.

The complexity of the bond-length distribution of the NCs as shown in Fig. 4.2 cannot be represented by the average values of Fig. 4.1. In general, the bond lengths are longest near the center of the NC, while they decrease further away from the center. Surprisingly, the bonds at the center are longer than the respective bulk interatomic distances, i.e., there is an expansion of the material inside the NC. Near the surface of the NCs, the bonds are shorter than the respective bulk lengths. While the latter compression might be caused by surface-tension-like effects, the expansion at the center cannot. The latter expansion has been related to the Si-H bonds [1], but this does not appear to provide a complete answer. For oxidized Si particles, Hofmeister *et al.* [192] find from their TEM studies an expansion for small sizes, while for larger particles they report a contraction. It is thus conceivable that the overall situation is a combination of the surface-stress-like effect inducing contraction, while another effect causes the expansion at the center or the expansion of the whole NC when the surface-stress is reduced, e.g., by oxidation. This is corroborated by the fact that many groups have found strong influences of the surface saturation on the NC properties [43, 44, 46, 187].

The straight lines in Fig. 4.2 are linear fits of the respective data. However, two remarks are in order. First, due to the symmetry of the NCs, each of the data points in Fig. 4.2 represents many bonds of the same length. No attempt has been made to show this multiplicity in the figure. Second, even though we use a linear fit, we do not claim that the dependence is in fact linear. We merely demonstrate the general trend. The slope of the lines decreases with increasing NC size. However, the results show that the bulk limit (zero slope at the bulk bond lengths) has not even nearly been reached for even the largest Si crystallites. That means that

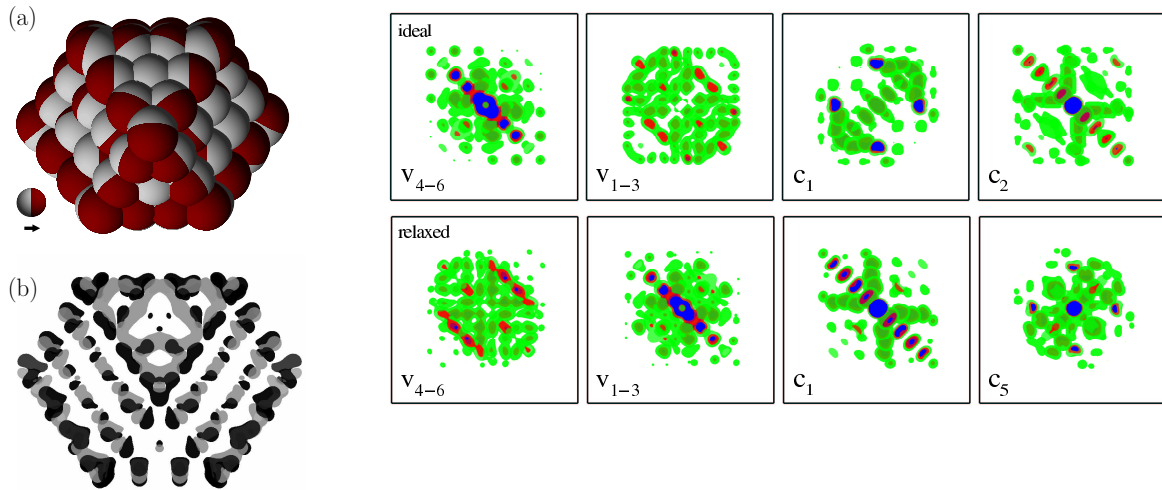


Figure 4.3 (a) Schematic view of the NC of 239 Ge atoms. The direction of the displacement during the relaxation is indicated as shown in the legend. (b) Difference of the electron densities before and after the relaxation. Electron transfer takes place from the grey (negative difference) to the black (positive difference) regions.

Figure 4.4 Plots of the electronic states close to the HOMO-LUMO gap for the ideal (upper panels) and the relaxed (lower panels) Ge crystallite of 83 atoms ($d=15.2$ Å). The notation v_{1-3} means that the highest three valence states are degenerate and, therefore, represented by their average. Partly transparent isosurfaces of the probability density are shown. The resulting shape has been sectioned along the midplane through the NC and is viewed from the z -direction. Thus, besides the contour plot of the values in the midplane, the parts of the distribution below that plane are also shown. A triply degenerate state c_{2-4}^{rel} for the relaxed crystallite has not been shown.

the apparent convergence towards the bulk interatomic distance of the larger Si NCs of Fig. 4.1 is an effect of the averaging rather than real convergence.

For the excited-state relaxed systems, the situation is not very different. The slope of the decrease of the bond lengths with increasing radial distance becomes steeper. However, the general effects found for the ground-state geometries are not changed. We note that the discussion of only the average bond lengths can be misleading. For instance, the 41-atom Si NC which does not show any change in the average bond length with the excitation, exhibits changes in the individual bond lengths comparable to the changes in the other NCs. The influence of the T_d symmetry for the excited system will be discussed in section 4.4.2.

The rectangular facets of the largest NC of the present work consist of 20 atoms (cf. section 3.1). In general, the atoms along the edges and at the corners move outward (though not necessarily radially) with respect to the ideal positions, whereas the atoms on the surface facets move inward or, for the larger NCs, move hardly at all. The relaxation thus increases the deviations from the spherical shape which indicates that surface stress alone cannot be responsible for the surface relaxation. The displacements are shown in Fig. 4.3 (a) where a schematic view of the 239-atom Ge NC is presented.

The atomic relaxation is accompanied by a change of the electrostatic energy. In Fig. 4.3 (b) the difference between the total electron densities for the ideal and the relaxed NCs is plotted. Electron transfer takes place from the gray to the black areas. It can be seen that the largest changes take place at the surface, and, especially, along the edges of the facets.

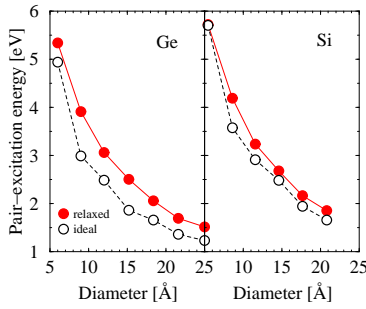


Figure 4.5 Pair excitation energies of Ge and Si NCs for the ideal (empty symbols) and the relaxed (filled circles) geometries.

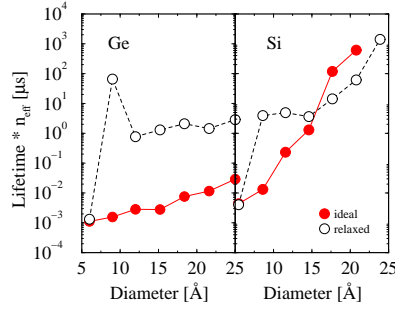


Figure 4.6 Radiative lifetimes of Ge and Si NCs at room temperature for the ideal (empty) and the relaxed (filled circles) geometries. The refractive index n_{eff} remains unspecified.

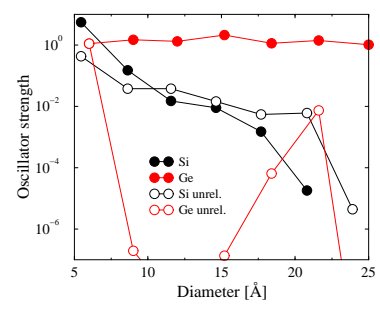


Figure 4.7 Effect of relaxation on oscillator strengths of lowest transitions.

The conclusion that electrostatic forces play some role for the surface relaxation, in particular the inward relaxation on the facets, is supported by analogies to free surfaces. Inward relaxation effects have been found for both Ge and Si (111):H-2x1 surfaces [193, 194] and for many low-index surfaces of metals, e.g., the W(100) surface [195]. By analogy to H-saturated surfaces [193] it is conceivable that a charge transfer towards the H atoms in the Ge-H and Si-H bonds causes a repulsion between the now positively charged Ge or Si atoms, thus contributing to the outward relaxation of the edge and corner atoms.

The effect of the structural relaxation on the lowest pair excitation energies is shown in Fig. 4.5. The energies have been calculated according to eq. (2.55). The results themselves will be discussed in section 4.1.2. The pair excitation energies shift to higher energies when the ionic relaxation is taken into consideration. They do so stronger for Ge than for Si. This is probably connected to the lesser overall reduction of the average bond lengths in Si (cf. Fig. 4.1). As the wave functions spread over the entire crystallite (see Fig. 4.4) it is very likely that they experience such an average effect. It will be shown in section 4.4.1 below that the band gap of Ge NCs increases with increasing hydrostatic pressure, i.e., with shortened bonds, which is consistent with the above interpretation. However, test calculations showed that this is not the case for Si where an increase of hydrostatic pressure causes an decrease in the gap energy, cf. section 4.4.1. Thus the increase in the pair excitation energies for the Si NCs cannot be explained simply by the average reduction of the bond lengths. Surprisingly, the excitation energies for the (relaxed) Ge and the Si NCs are almost equal.

The atomic relaxation influences the energetic ordering of the single-electron states. We consider the corresponding one-particle states near the HOMO and the LUMO states of the 83-atom Ge NC. Their respective probability densities are plotted in Fig. 4.4 for the ideal and the relaxed geometry. The HOMO-LUMO transitions of the unrelaxed Ge NCs are forbidden [144]. However, just above the HOMO-LUMO gap, there are very strong optical transitions. In the 83-atom Ge NC they correspond to a transition between the states v_{4-6}^{ideal} and c_1^{ideal} with oscillator strength 0.22 and between the states v_{4-6}^{ideal} and c_2^{ideal} with a value of 0.38. The notation means that the state v_{4-6}^{ideal} is triply degenerate (without spin) and comprises the 4th-, 5th-, and 6th-highest valence states. Accordingly, c_1^{ideal} is the (non-degenerate) lowest unoccupied state. In addition, each state is doubly degenerate because of the spin.

For the relaxed NC, the energetic ordering is changed. While the electronic states are not, strictly speaking, the same as for the unrelaxed system, at least some of them change only very little. Comparison shows that the triply degenerate second-highest state v_{4-6}^{ideal} of the unrelaxed system becomes the HOMO state v_{1-3}^{relaxed} of the relaxed system, thereby remaining almost unchanged. Moreover, the former second-lowest unoccupied state c_2^{ideal} becomes, with slight modifications, the LUMO state c_1^{relaxed} . We mention that there is a state c_{2-4}^{relaxed} (not shown) which is not among those shown for the ideal system.

The situation for the other Ge NCs is very similar. In contrast to the ideal geometries, strong HOMO-LUMO transitions have been found for all the relaxed Ge NCs. Test calculations treating a non- T_d Ge NC of somewhat arbitrary shape, which have reproduced the strong transitions at the HOMO-LUMO gap, will be discussed on page 76.

The strong HOMO-LUMO transitions in the relaxed Ge NCs reduce the radiative lifetimes drastically compared to those of the ideal structures. This effect is shown in Fig. 4.6. The lifetime τ has been calculated using eq. (2.73) which assumes completely thermalized distributions of the excited electrons and holes [125]. Consequently, due to the occupation, the lifetimes (or their inverse, the radiative transition probabilities) are governed by the lowest few transitions. For Ge NCs with their change in the energetic order of the states this manifests an extreme influence of the structural relaxation on the lifetimes, changing them by more than two orders of magnitude. For all the larger NCs, beginning with the 41-atom NC, this result is consistent. Fig. 4.7 shows the strengths of the lowest transitions.

For Si NCs, on the other hand, the result is not as uniform. In contrast to Ge, Si NCs have no single strong transitions of particular importance. Therefore we did not attempt to identify individual transitions before and after the relaxation. However, also here substantial changes are found. Figure 4.6 shows that they are smaller than for the Ge crystallites. Moreover, unlike for the Ge crystallites, the lifetimes are not always reduced. In general, apart from the smallest crystallites of only a few atoms, the radiative lifetimes of the Si NCs are much larger than those of the Ge crystallites. This is in agreement with the trend of measurements of the radiative lifetimes for $\text{Si}_{1-x}\text{Ge}_x$ alloy NCs [22, 196].

4.1.2 Excitation energies

In Fig. 4.8 and 4.11 we present the pair-excitation energies E_g^{opt} calculated according to eq. (2.55) for the ground-state geometries along with other theoretical and with experimental results. For both Si and Ge the calculated pair excitation energies show the well-known approximate $1/d$ (d -diameter) dependence [23, 144]. For small crystallite sizes ($\lesssim 1$ nm) our results for Si NCs in Fig. 4.8 agree well with the pair excitation energies obtained within the time-dependent local density approximation (TDLDA) [14]. In the intermediate range of crystallite diameters of 1–2 nm the ΔSCF energies lie below the TDLDA results. It seems that the vertex corrections, i.e., the direct Coulomb attraction of electrons and holes, are underestimated in the XC kernel of the TDLDA whose validity is recognized in particular for confined systems [19]. For larger NCs (>2 nm) there is an indication that both the TDLDA and the ΔSCF approach yield excitation energies which are too small because the crystallites are already too

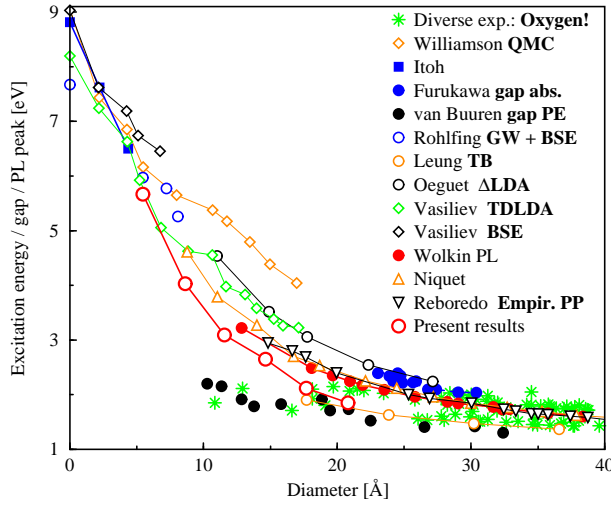


Figure 4.8 Lowest electron-hole-pair excitation energies of Si NCs. The empty symbols are theoretical results while the filled symbols indicate experimental values. Besides the present results we show the results of absorption measurements of Itoh *et al.* [80] and Furukawa *et al.* [197], PL of Wolkin *et al.* [46], and the combined photoemission and core-level absorption spectra of van Buuren *et al.* [198]. Theoretical results are GW+BSE of Rohlfling *et al.* [32], Δ LDA according to eq. (2.50) of Ögüt *et al.* [28], empirical-pseudopotential of Reboredo *et al.* [39], time-dependent density-functional theory and Bethe-Salpeter-equation results of Vasiliev *et al.* [14] and quantum Monte Carlo of Williamson *et al.* [107]. For one Si atom, $d = 0$ has been chosen in accordance with other publications.

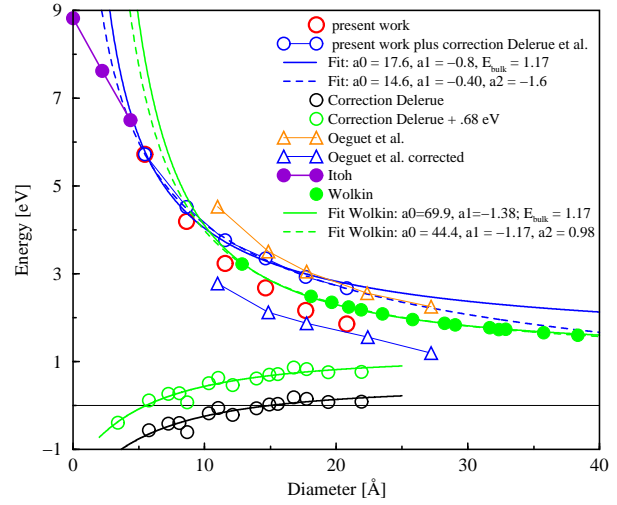


Figure 4.9 Different fits to the data of fig 4.8 and the visualization of the different corrections. Black circles: correction $\delta\Sigma - \delta\Sigma_{\text{bulk}} - E_{\text{coul}}$ of Delerue *et al.* [29], cf. eq. (2.2), along with a numerical fit. Green circles and fit: The same quantity but without subtracting $\delta\Sigma_{\text{bulk}}$. This is added to the present results (red circles) to get the “corrected” values (blue circles), yielding fits according to eq. (4.1) with fixed bulk limit (blue, solid) or free parameter a_2 (blue, dashed). This is compared to the PL data of Wolkin *et al.* [46] and fits according to eq. (4.1) with fixed bulk limit (green, solid) or free parameter a_2 (green, dashed). The optical gaps as calculated by Ögüt *et al.* are shown as well as the corrected data using the Coulomb energy of Delerue *et al.* [29].

large. As mentioned in section 2.2.3.1, in the bulk limit neither theory gives the correct excitation energies. The energies resulting from a solution of the Bethe-Salpeter equation [14] are somewhat larger and, hence, probably indicate a weaker effective electron-hole attraction. The energies obtained by Ögüt *et al.* using the other Δ SCF method eq. (2.50) and reduced by their screened Coulomb energy [28], cf. eq. (2.51) are larger. As the two approaches are similar in their interpretation, we compare $E_g^{\text{QP}} - E_{\text{coul}}$ of Ögüt *et al.* and $E_N^{(\text{e+h})} - E_N$ of the present work in Fig. 4.9. The fact that Ögüt *et al.*’s values are larger throughout is, at first sight, surprising. However, analysis of the data shows that it seems to be caused mainly by a deficiency of the approximate Coulomb term employed in eq. (2.50): If starting from the quasiparticle gaps of Ögüt *et al.* one calculates the optical gap not using their Coulomb energies but the energies of the BSE calculations of Delerue *et al.* [29], a much better agreement is obtained, as shown in Fig. 4.9. This indicated that the problematic part is the Coulomb term, not so much the calculation of E_g^{QP} . This again shows the superiority of the present method, because here the Coulomb interaction is included *en passant*; see also section 2.2.3.1). Two semi-empirical calculations are available: Tight-binding of Niquet *et al.* [199] and semi-empirical pseudopotential results of Reboredo *et al.* Owing to their construction, both lead to the correct result in the large-NC limit. Consequently, they agree well in this range. However, with smaller radii the justification becomes less and less strict. The fact that our values lie below these results is not surprising

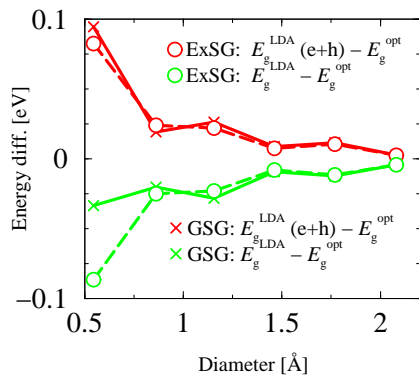


Figure 4.10 Difference of Δ SCF excitation energies E_g^{opt} for excited-state and ground-state electronic relaxation, and LDA HOMO-LUMO gap E_g^{LDA} for Si NCs. We compare values for both the fixed excited-state-relaxed geometry (ExSG) and the ground-state-relaxed (GSG) geometry. Terminology is like in Fig. 2.3, (e+h) indicates that the E_g^{LDA} has been calculated with an electron-hole pair present.

after the above discussion. Recent Quantum Monte Carlo results [107] differ distinctively from all the other results in the intermediate size range.

The comparison with experimental data is difficult, despite the huge amount of excitation energies measured in photoluminescence and absorption experiments. The majority of these data sets does not describe quantized electronic states localized in the interior of the NCs. Many data sets are related to defect states or interface states localized in the interface region between crystallite and matrix material. There is now agreement in the literature that the surface termination, in particular oxidation, changes the excitation energies decisively [41–46]. The data of diverse experiments involving oxygen are, therefore, only indicated collectively by the green stars. However, the PL peak positions measured by Wolkin *et al.* [46] for the samples without oxygen are certainly due to confinement effects. Moreover, they have been shown to change strongly after exposure to oxygen [46] which indicates that the results reproduced in Fig. 4.8 are due to largely oxygen-free samples.

Similar conclusions hold for the absorption data of Furukawa *et al.* [197]. The agreement of our calculated pair energies and the experimental data, in particular with the PL values [46], is good. The difference for the largest NCs considered may indicate that the validity of the Δ SCF method underestimates the excitation energy for the larger radii [30]. On the other hand, the gap energies inferred from the measurements of van Buuren *et al.* [198] fall below the calculated and measured values. This may be essentially a consequence of the large core-exciton binding energies occurring in the X-ray absorption of the underlying combined experiments [39]. At the other end of the size range, our values are in excellent agreement with the absorption data of Itoh *et al.*

In general, compared to all the other results our values seem to be correct for the intermediate and small size range, while they are slightly too small for the largest crystallites. In order to check the suggestion Godby and White [30] of the additive, weakly d -dependent contribution and the finding of Delerue *et al.* in Fig. 2.2, we take the latter values of $\Delta - \Delta_{\text{bulk}} - E_{e-h}$ and fit some convenient function to get a representation of all sizes. If our values were correct up to that correction, and if the latter were correct, adding this quantity should give the correct excitation energies. Fig. 4.9 shows that now the values lie above the experimental values of Wolkin *et al.* The small-size limit remains unchanged.

We conclude this discussion with a comparison between the LDA HOMO-LUMO gaps and the our pair excitation energies in Fig. 4.10. On the energy scale of Fig. 4.8, the two

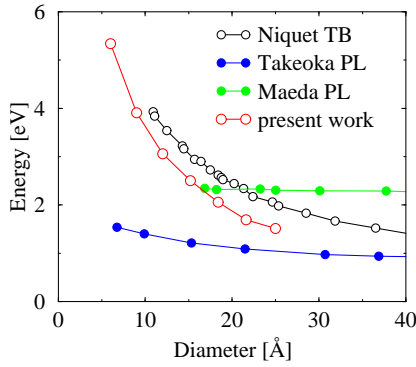


Figure 4.11 Pair-excitation energies of Ge. The present results are compared to those of Niquet *et al.* [204]. PL data are from Takeoka *et al.* [2] and Maeda *et al.* [201].

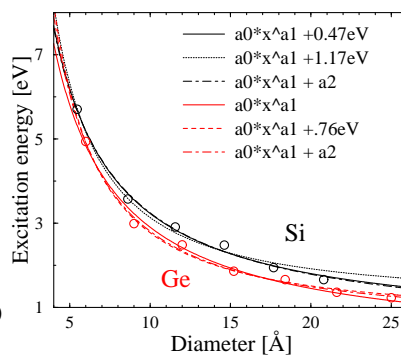


Figure 4.12 Pair excitation energies of ideal Si and Ge NCs. The fits according to eq. (4.1) are given solid for fixed LDA bulk limit, dotted for fixed experimental bulk limit, and dot-dashed for free parameters a_2 . The fit parameters are given in table 4.1.

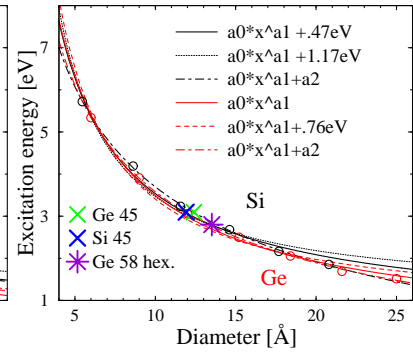


Figure 4.13 Same as Fig. 4.12 but for the relaxed structures. In addition we show the values for non-spherical Ge and Si NCs of cubic structure, as well as of a 58-atom Ge NCs of hexagonal structure. The latter structures are hydrogenated.

quantities are indistinguishable. However, for extreme localization differences occur, as has also been pointed out by Degoli *et al.* [200]. In general, for a ground-state calculation, the LDA HOMO-LUMO gap is smaller than the excitation energy. The contrary holds for an excited-state relaxation. An explanation has not yet been found.

In conclusion, our results tend to underestimate the excitation energies for the larger crystallites. However, using the correction due to Delerue *et al.*, the values seem to be slightly overestimated.

In contrast to luminescence from silicon NCs, there are, to the best of our knowledge, no experimental results for Ge which can be clearly attributed to the recombination of quantum-confined excitons. Neither the results of Takeoka *et al.* [22] nor of Maeda *et al.* [201] show the expected size dependence for luminescence from quantum-confined systems. For that reason, our excitation energies for Ge NCs shown in Fig. 4.11(b) are considered a prediction. They are compared to the tight-binding result of Niquet *et al.* [199]. Assuming that the cancellation effects and, therefore, our results for the Ge NCs are similar to those of Si (cf. Ref. [29]) we conjecture that our values might be too small for the larger sizes, while they should be correct for the smaller NCs. This would be in agreement with the assumption that the TB results, while valid in for $d \rightarrow \infty$, will not be correct for the smaller sizes. It has been claimed that the excitation energies in Ge NCs are larger than those in Si NCs in the intermediate size range [202,203]. Our results show no indication of such an effect.

Different functional dependencies are conceivable for a description of the gaps. Especially the limits for $d \rightarrow \infty$ and $d \rightarrow 0$ have to be considered. In the following we show that, while they are useful, fits of the excitation energies can only be considered valid within some limited range.

Two effects are considered in the d -dependence of the excitation energies. First, there is the part which is due solely to the confinement. On the other hand, the structural relaxation which

induces inhomogeneous strains in the NC, will also contribute to the energies. For this reason it is instructive to consider both the relaxed and the ideal structures.

Effective-mass theory predicts for a 3- d spherical quantum well a diameter dependence of $1/d^2$ [92]. In Figs. 4.9,4.12, and 4.13 we show the energies along with fits according to

$$E_{\text{fit}} = a_0 d^{a_1} + a_2 \quad (4.1)$$

where a_2 can be either fixed to (a) the experimental bulk gap, (b) the DFT-LDA bulk gap, or else can be (c) considered a free parameter. Along with the very bold assumption that the fits be valid when going from the NC size range to the bulk limit, this assumes that (a) the self-energy effects are fully contained in the excitation energies, or (b) that the bulk limit of the fit is the DFT-LDA gap. However, when used for the energies obtained for a limited number of relatively small NCs, this **assumes** the validity of the functional dependence throughout the whole size range, cf. discussion in section 2.2.3.2. It is this functional dependence which corresponds to the weakly R -dependent extra self-energy contribution as discussed in section 2.2.3.2. If this is true, the fit function will vary according to how many of the NCs are considered for the fit, because the added contribution is going to be smaller or zero for the smallest NCs, cf. Fig. 2.2. This is actually the case, as shown in table 4.1.

Si	size range	Si ideal			Si relaxed			bulk limit
		a_0	a_1	a_2	a_0	a_1	a_2	
$a_0 d^{a_1} + E_{\text{g}}^{\text{LDA}}$	5–239	30.9	-1.05	–	25.6	-0.92	–	$E_{\text{g}}^{\text{LDA}} = 0.47 \text{ eV}$
	17–239	27.9	-1.01	–	47.6	-1.15	–	
	41–239	45.9	-1.19	–	79.3	-1.33	–	
$a_0 d^{a_1} + E_{\text{g}}^{\text{exp.}}$	5–239	48.3	-1.39	–	34.6	-1.18	–	$E_{\text{g}}^{\text{exp.}} = 1.17 \text{ eV}$
	17–239	60.0	-1.48	–	150.7	-1.74	–	
	41–239	189.9	-1.90	–	586.3	-2.22	–	
$a_0 d^{a_1} + a_2$	5–239	29.2	-1.00	0.33	18.5	-0.41	-3.4	a_2
	17–239	79.8	-0.03	-71.3	17.8	-0.34	-4.5	
	41–239	27.2	-0.11	-18.0	296.7	-1.93	1.0	
Ge	size range	Ge ideal			Ge relaxed			bulk limit
		a_0	a_1	a_2	a_0	a_1	a_2	
$a_0 d^{a_1}$	5–239	29.0	-1.0	–	25.2	-0.86	–	$E_{\text{g}}^{\text{LDA}} = 0.0 \text{ eV}$
	17–239	21.0	-0.88	–	29.9	-0.92	–	
	41–239	27.3	-0.97	–	34.7	-0.97	–	
$a_0 d^{a_1} + E_{\text{g}}^{\text{exp.}}$	5–239	53.3	-1.42	–	35.2	-1.12	–	$E_{\text{g}}^{\text{exp.}} = 0.76 \text{ eV}$
	17–239	49.3	-1.39	–	55.9	-1.30	–	
	41–239	122.3	-1.71	–	90.8	-1.47	–	
$a_0 d^{a_1} + a_2$	5–239	44.7	-1.3	.6	19.4	-0.58	-1.5	a_2
	17–239	22.4	-0.11	-0.98	20.1	-0.62	-1.3	
	41–239	91.3	-1.6	0.67	21.5	-0.67	-1.02	

Table 4.1 Fit parameters for different fits according to eq. (4.1), either fixing the parameter a_2 to the experimental or the LDA bulk limit, or else leaving it a free parameter. Included in the respective fits are the NCs as indicated in the column *size range*. The units of the parameters are $[a_0] = \text{\AA}^{-1}$, $[a_1] = 1$, $[a_2] = \text{eV}$.

From this table it is clear that the question after the functional dependence of the excitation energies does not have a clear answer. Independently of the additional complication that the geometry is not strictly spherical, there is the ill-defined limit of $d \rightarrow 0$. While the NC radius and the localization radius can be considered reasonably equivalent for the NCs, in this limit

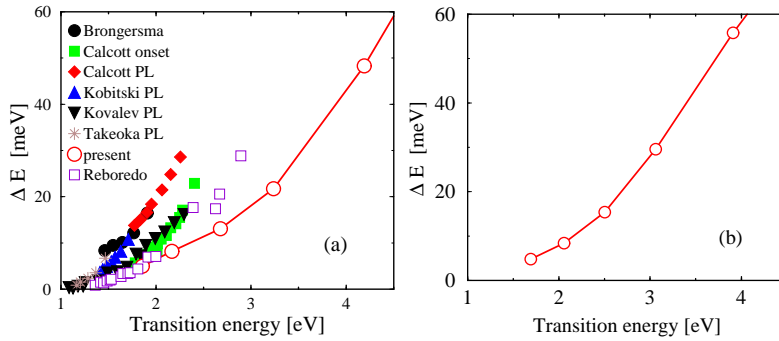


Figure 4.14 Spin-exchange splitting between singlet and triplet exciton: (a) Si, (b) Ge. Besides calculated values (circles) we show results of empirical-pseudopotential calculations of Reboredo *et al.* [39], the absorption measurements of Calcott *et al.* [108] and the PL data of Calcott *et al.* [108], Brongersma *et al.* [109], Kobitski *et al.* [110], Kovalev *et al.* [208] and Takeoka *et al.* [22] for oxidized Si NCs or porous Si.

the localization is that of an atomic or molecular orbital. All the fits suggested above will go to infinity for $d \rightarrow 0$. Thus the fits will be of limited value here for the discussion of the energies.

Moreover, when going from the NC size range to the bulk, the localization mechanism changes: While for NC radii smaller than the free-exciton radius the confinement is the primary localization cause, in the bulk the relative localization between electron and hole is caused by the Coulomb attraction. For that reason it would be surprising if a simple fit comprising both ranges gave a correct, unified description.

This is evidenced by the values in table 4.1. The fits differ depending on which bulk limit is chosen, and depending on how many NCs are included. The qualitative conclusion is that in the intermediate size range, an approximate $1/d$ -dependence prevails, the exponent of d lying between $a_1 = -0.8$ and $a_1 = -1.2$. Available experimental data for Si are Wolkin *et al.*, $a_1 \approx -1.4$ [46], Matsumoto *et al.*, $a_1 \approx -1.6$ [205], and Ledoux *et al.*, $a_1 \approx -1.4$ [206]. Slightly smaller values have been measured by Heitmann *et al.* [207].

No strong differences are found between Ge and Si NCs. This appears reasonable in view of two simple examples. For a particle in a harmonic potential the diameter dependence is $1/d$. The effective-mass approximation obtains for a particle in a square-well potential a dependency like $1/d^2$. It is reasonable to assume that the actual local potential for an electron in the NC has a shape in between these two examples. Hence the result of $a_1 \approx -1.0 \dots -1.4$ seems reasonable.

4.1.3 Exchange splitting

Spin-polarized (LSDA) calculations have been carried out to calculate the exchange splitting between singlet and triplet exciton within the present Δ SCF method as discussed in section 2.2.5. The LDA-relaxed ground-state geometries have been used. The splitting calculated according to eq. (2.59) is shown in Fig. 4.14 in dependence on the singlet pair-excitation energy. There is an approximately quadratic relationship between spin-exchange splitting and pair excitation energy. The splittings for Ge are similar, perhaps slightly larger.

The calculated splittings are compared in Fig. 4.14 (a) with experimental data [108–110, 208] and calculated values of other authors [39] for Si NCs. For smaller transition energies, i.e., for larger sizes, the agreement between the calculated data is good. With increasing transition energies, however, the Δ SCF values tend to underestimate the spin-exchange splitting. In prin-

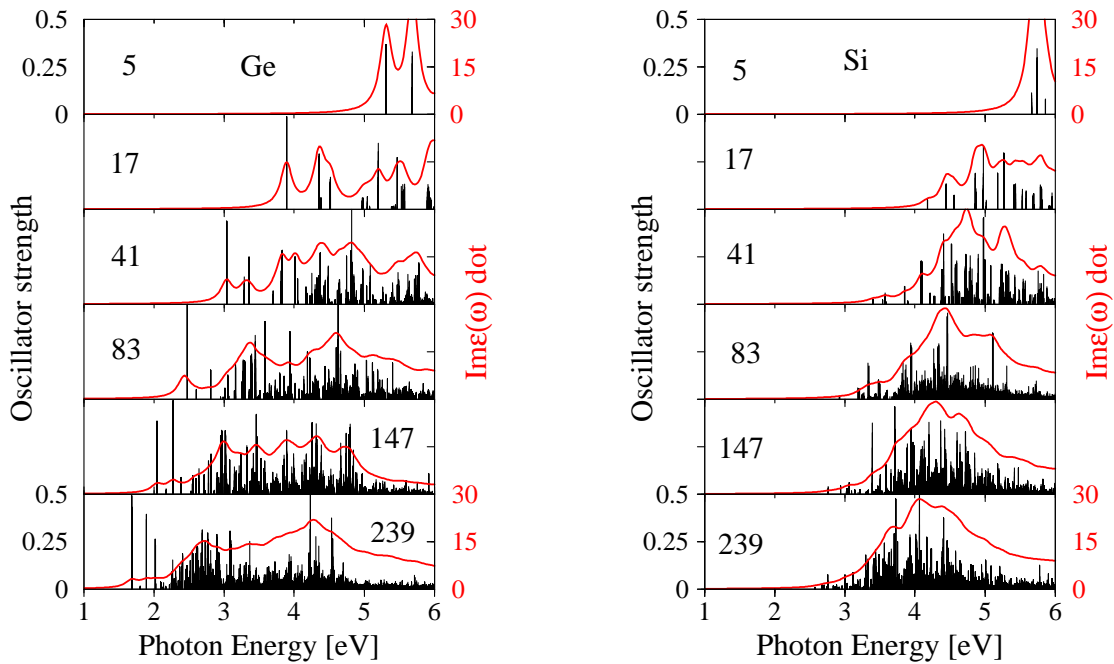


Figure 4.15 Oscillator strengths of the optical transitions (vertical lines) versus the transition energies for Ge and Si crystallites with varying size. The normalized absorption spectrum $\text{Im}\epsilon(\omega)/f$ (solid line) is plotted to envelope the oscillator strengths. The number of atoms is indicated for each crystallite.

principle, this is also true for the comparison with the experimental data. However, this comparison is questionable for two different reasons. First, all the experimental samples involve oxygen. However, unlike for the PL energies [46], so far it seems not clear how the splitting is influenced by the oxygen. Probably, in the experiments the exciton energies are partially related to defect states or interface states. Second, the DFT-LSDA [55] used here is not able to describe pure multiplets. This is a general problem [111]. A rigorous description of multiplets requires symmetry-adapted exchange-correlation functionals, which are not available [112]. In the spin-polarized approach one can only fix the projection M_S of the total spin S but not the total spin itself. One describes actually a high-spin state with $S = 1$, $M_S = \pm 1$ (which is a triplet state) and a low-spin state with $M_S = 0$ (which is probably a mixture of spin states). Consequently, this approach tends to underestimate the spin splitting and gives a lower limit.

4.1.4 Transition probabilities

The NC size influences not only the energetic positions of the optical transitions but also their oscillator strengths as shown in Fig. 4.15. The oscillator strengths $f_{cv}^{\alpha\alpha}(\mathbf{k})$ of eq. (2.74) are plotted as vertical lines against the transition energies, along with the imaginary part of the corresponding (normalized) dielectric function. For Si NCs (Fig. 4.15b) with diameters above 1.5 nm a tail of weak transitions appears above the HOMO-LUMO gap. The oscillator strengths of these transitions are much smaller than the maximum oscillator strengths of about 0.4. This is due to the fact that the LUMO is primarily determined by states corresponding to the X point

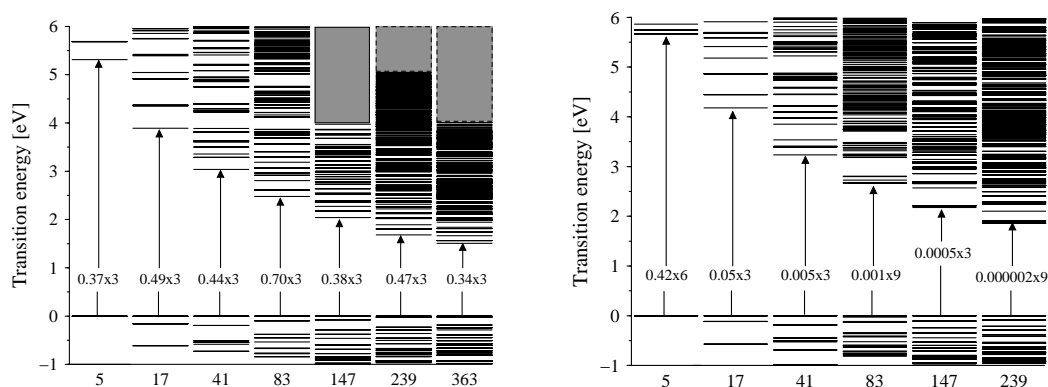


Figure 4.16 Level scheme of Ge (left) and Si (right) NCs. The HOMO level defines the energy zero. The lowest optical transitions are indicated by vertical arrows, the numbers indicate oscillator strength and the degeneracy.

in bulk Si, the HOMO by states corresponding to the zone-center states. Therefore the indirect-gap behavior of the bulk carries over to NCs down to fairly small sizes. This will be detailed in section 4.4.1. On the other hand, the large oscillator strengths at energies above 3 eV in the Si NCs with 83, 147, and 239 atoms correspond to the strong direct high-energy transitions in bulk silicon.

The behavior near the HOMO-LUMO transitions in Ge NCs is completely different. Very strong transitions occur close to the absorption edge, even for clusters with a diameter of about 2.2 nm. These transitions appear to be related to the formation of an E_0 -like absorption feature in the more extended Ge NCs. The occurrence of these strong transitions might explain the differences in the luminescence behavior of nm-sized Si and Ge NCs. A strong near-infrared luminescence has been observed for Ge NCs in a SiO_2 matrix [2], although the role of the oxygen is not clear. In section 4.4.1 below, these differences will be related to the fact that in bulk Ge the strong direct E_0 transition occurs close to the indirect gap. In bulk Si the E_0 transition and the indirect gap are separated by about 2.5 eV. As a consequence, the radiative lifetimes of Ge NCs are much shorter than those in the Si crystallites. This is illustrated by the level schemes in Fig. 4.16. The oscillator strengths of the lowest transitions in the Si NCs reduce strongly when the size increases, while in Ge they remain approximately constant. In general, Ge NCs are predicted to be more suitable for light-emitting devices than Si NCs where the radiative recombination of electrons and holes must be phonon or defect assisted. Similar conclusions have been drawn by Kholod *et al.* [209, 210] for Ge nanosheets.

4.1.5 Radiative lifetimes

The global, spectrally integrated PL behavior is determined by the recombination rate or its inverse, the radiative lifetime τ . We calculate τ according to eq. (2.73) which assumes completely thermalized distributions of the excited electrons and holes [125]. Room temperature is assumed. The calculations are performed for the ground-state geometries. Test calculations for the 83-atom Ge crystallite have shown that the influence of the modification of the geometry due to the excitation is weak, at least as long as the symmetry constraint is used, cf. the discussion

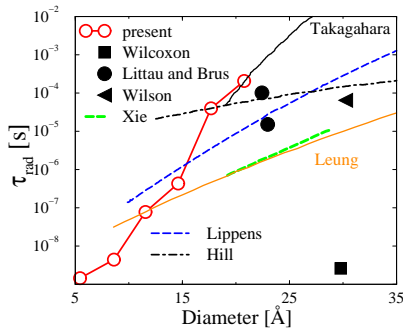


Figure 4.17 Radiative lifetimes for Si NCs vs. diameter. Beside the present results (circles) we show the calculated values of Lippens *et al.* [211], Takagahara *et al.* [212], and Hill *et al.* [24] as well as tight-binding results of Niquet *et al.* [204]. Experimental results are shown of Wilcoxon *et al.* [213], Xie *et al.* (taken from reference [213]), Littau *et al.* [4], Wilson *et al.* [214] and Kanemitsu *et al.* [215].

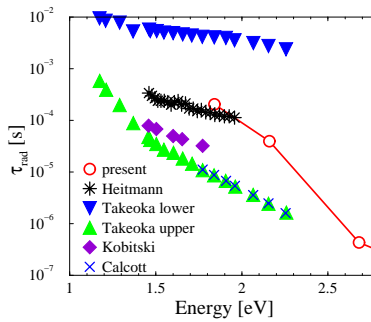


Figure 4.18 Radiative lifetimes for Si NCs vs. excitation energy. We compare the calculated values (circles) with the PL results of Heitmann *et al.* [216], Takeoka *et al.* [22] for their lower and their upper transition, those of Kobitski *et al.* [110], those of Calcott *et al.* [108], and those of Kanemitsu *et al.* [215] for α -Si and c-Si.

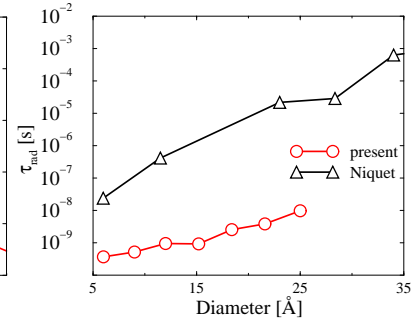


Figure 4.19 Radiative lifetimes of Ge NCs. The present results are compared to the TB values of Niquet *et al.* [199].

below of the Stokes shifts in section 4.4.2. The radiative lifetime is reduced by about 5 %. Our results are presented in Figs. 4.17 and 4.19 in dependence on the NC diameter (for Si and Ge) and on the pair-excitation energy (for Si) in Fig. 4.18. The results for Si and Ge are qualitatively different. In the size range of 1 – 2 nm crystallite diameter the Si radiative lifetime is changed by more than five orders of magnitude. For the Ge crystallites this variation is less than one order of magnitude. The different radiative behavior of Si and Ge NCs is a consequence of the qualitative differences in their oscillator strengths.

For the Si NCs in Fig. 4.18 we compare our results with experimental results and with results based on different semi-empirical descriptions of the electronic structure [24,100,211,212]. The trend of increasing lifetimes with the diameter is reproduced by all the theoretical approaches. For small diameters the various theories (with the exception of Ref. [24]) seem to approach extremely small values. On the other hand, for large diameters the *ab initio* results seem to approach the lifetimes calculated within the effective-mass approximation (EMA) [212]. All the other approaches underestimate the radiative lifetime in this size region. Unlike the calculations which assume defect-free crystallites with defined and saturated surfaces, the experimental samples are highly irregular and contain defects, reconstructed surfaces, and interfaces. Nonetheless, the agreement of our lifetimes with the experimental values is fair, despite the complications concerning the experimental determination of the diameter and the uncertainty as to precisely which physical system has been investigated by the measurements. In particular, the agreement with the measurements of Littau and Brus [4] for colloidal NCs is excellent. The values measured by Wilcoxon *et al.* [213] are, however, smaller by orders of magnitude in comparison to all theoretical values. It is, therefore, apparent that a different physical mechanism has been measured.

There are more experimental data of radiative lifetimes for Si NCs. However, these are data given in terms of the PL energies rather than in terms of the diameters. The corresponding comparison for the Si lifetimes given versus PL energies is shown in Fig. 4.18. In general, our lifetimes agree well with some of the experimental results. The agreement with the data of Heitmann *et al.* [216] is excellent, whereas the other experimental values envelope our theoretical lifetimes. However, the measurements of Heitmann *et al.* [216] have been performed at a temperature of 100 K. With the lowering of the temperature one expects an increase of the lifetimes as also shown experimentally [212]. Moreover, the measurements of Takeoka *et al.* [22] are not directly related to quantum-confined states of the NCs. Rather, these authors have measured luminescence in which different defect or interface states are involved.

Again, there are no experimental data for Ge NCs with different diameters or excitation energies. Therefore, the results for the Ge crystallites in Fig. 4.18 remain predictive. There is only another calculation of Niquet *et al.* [204] based on the electronic structure and optical transition matrix elements from a semi-empirical tight-binding method. We point out that the lifetimes calculated within our *ab initio* method are shorter by two orders of magnitude than the results obtained from the TB calculations [204]. The main difference, however, is probably related to the transition matrix elements which are considerably underestimated in the TB method. Single rough experimental values are also reported which are close to our findings. Takeoka *et al.* [217] reported the lifetime of Ge NCs to be shorter than 40 ns. Moreover, the PL intensity variation of Takeoka *et al.* [2] is very similar to the (inverse) lifetime dependence of our results in the same size range. Aoki *et al.* [20], on the other hand, do not find a ns PL lifetime component.

4.1.6 Spectra

Figs. 4.20 and 4.21 show optical spectra of Ge and Si NCs, calculated using the independent particle approach, cf., eq. (2.71). The absorption spectrum for the smallest Si cluster of 5 atoms shows the same basic features as obtained in a more sophisticated calculation [32]. However, the model atomic structure used is somewhat unrealistic, and important many-body effects are not included. For that reason, we focus our attention on the larger NCs which, despite their different numbers of atoms, exhibit similar spectra. The principal spectra resemble those found within an empirical pseudopotential approach for Si [23].

The spectra in Figs. 4.20 and 4.21 are strongly influenced by quantum confinement effects. The absorption threshold moves to lower energies with increasing NC size. Different effects of spatial quantization are observable for the main absorption structures, shoulders or peaks, for energies below 5 (6) eV for Ge (Si) as NC material. In the case of Ge, the shoulder at the low-energy side close to the HOMO-LUMO gap shifts strongly towards smaller energies with increasing crystallite size. This shoulder seems to be a consequence of the strong optical transitions which develop into the E_0 structure in the bulk limit. The first direct E_0 transition in Ge bulk crystals lies energetically only slightly above the indirect energy gap [218]. The first peak in the 3 eV range, which also varies with the size, develops into the bulk E_1 structure. Its oscillator strength is probably underestimated because excitonic effects are neglected in the independent-particle approach. The peak shifts from 3.6 eV (41-atom cluster) to 2.6 eV (363-

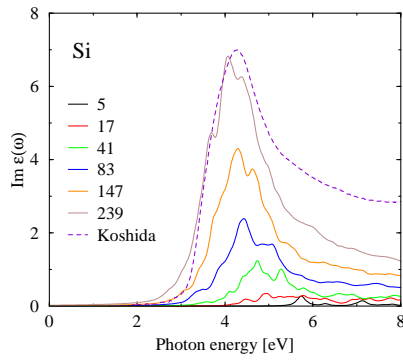


Figure 4.20 Dielectric functions of Si NCs with a varying number N of Si atoms as indicated. Values for 1000-atom-equivalent cell. The experimental spectrum is taken from Koshida *et al.* [35] and has been scaled accordingly, cf. eq. (4.2). The NC size of the sample of Ref. [35] is unknown.

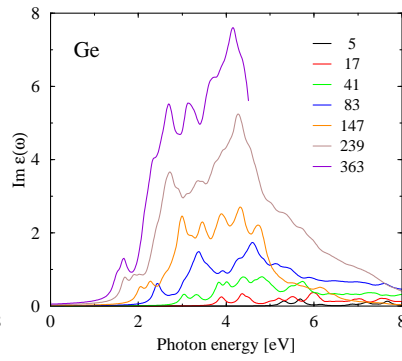


Figure 4.21 Spectra as in Fig. 4.20 for Ge NCs.

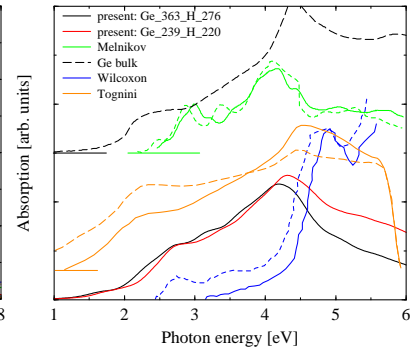


Figure 4.22 Absorption Ge: Comparison with experiment and other authors. NCs in sapphire of Stella *et al.* [220] and of colloidal NCs of Wilcoxon *et al.* [3], together with LDA spectra of Melnikov *et al.* [221] and the absorption spectrum of bulk Ge [185]. The relative strengths are not related, the curves are offset along the y -axis as indicated.

atom cluster). The main peak with a maximum around 4 eV shifts much less towards smaller photon energies and develops into the E_2 structure of the bulk spectra. There is a weaker peak or shoulder at the high-energy side at about 6 eV. In the bulk case it corresponds to a structure that appears only weakly in the experimental spectra. Commonly it is related to different transitions, e.g. $\Lambda_{3v} \rightarrow \Lambda_{3c}$ and $\Delta_{5v} \rightarrow \Delta_{2'c}$ [219].

The imaginary part of the dielectric function of Si NCs is shown in Fig. 4.20. Only one broad structure appears with a maximum between 5 and 6 eV. It shifts towards smaller photon energies with increasing NC size. The structure seems to develop into the bulk E_2 peak. In the case of the largest NCs we considered, the almost complete absence of the E_1 structure may be related to neglecting the excitonic effects. The Coulomb effects enhance the oscillator strength of the E_1 peak but reduce the strength of the E_2 peak [90]. The overall shape of the spectra in Fig. 4.20 is similar to that observed for oxidized Si nanoparticles [35]. We observe that the spectra calculated for Si using the empirical-pseudopotential scheme [23] or, for Ge, using the semiempirical tight-binding method [34], are similar.

Until now we have considered the properties of the supercell arrangement, i.e., of the composite medium of NCs and vacuum. In order to extract the dielectric function $\varepsilon_{\text{nc}}(\omega)$ pertaining to the NCs we use the simple superposition formula

$$\varepsilon(\omega) = f\varepsilon_{\text{nc}}(\omega) + (1 - f)\varepsilon_{\text{host}}(\omega). \quad (4.2)$$

The quantity $\varepsilon_{\text{nc}}(\omega)$ represents the optical properties of an effective bulk material which also reflects the quantum size effects characterized by a fixed NC radius R . Therefore, $\varepsilon_{\text{nc}}(\omega)$ obtains its meaning only with respect to embedment in surrounding materials with possibly different filling factors but fixed NC radius. According to the independent-particle expression (2.71) of the dielectric function, formula (4.2) should be nearly exact as long as the wave functions of the electrons of the NC and the host material are strongly localized. This should be fulfilled

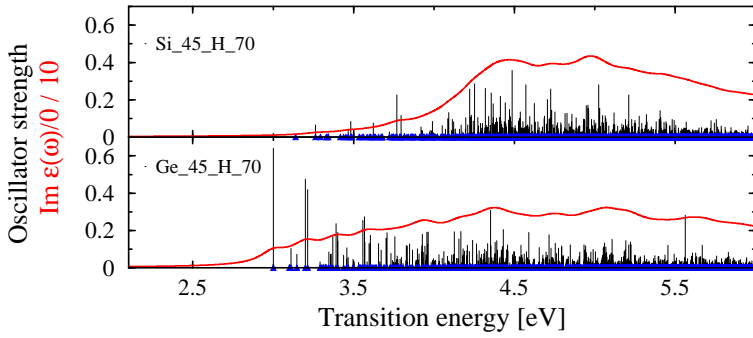


Figure 4.23 Spectra and transition probabilities: nonsymmetric Ge and Si NCs. The spectra and the oscillator strengths have been averaged over the Cartesian directions.

in the case of vacuum as the host material. In fact, expression (4.2) has been found to yield excellent and reproducible results. We have tested eq. (4.2) by deriving $\varepsilon_{\text{nc}}(\omega)$ for NCs from different supercells. The corresponding dielectric functions of the composite materials have been calculated for one and the same NC but using supercells of different size. The crystallite-dielectric function $\varepsilon_{\text{nc}}(\omega)$ has been extracted using expression ((4.2)). We do not present the spectra because the curves are virtually indistinguishable. This result indicates both the validity of eq. ((4.2)) and the fact that our supercell treatment's spectra are converged with respect to the cell size. Since $\varepsilon_{\text{host}}(\omega) = 1$, formula ((4.2)) amounts to a simple scaling of the imaginary parts with the filling factor f .

While for the Si NCs the good agreement with the dielectric function of Koshida *et al.* has been found, most experimental spectra for Ge NCs are absorption spectra. We find good agreement of our results with the absorption of Ge in sapphire of Stella *et al.*, while there is an energetic difference between these and the spectra of colloidal Ge NCs of Wilcoxon *et al.* [3] which exhibit also different relative peak heights. The reasons for this are unknown. The remaining discrepancy between our result and that of Stella *et al.* is, in part, due to the different matrix (instead of vacuum). This can be taken care of by means of effective-medium theory [48, 144] which is beyond the scope of the present presentation. We note that our spectra closely resemble the absorption spectra of bulk Ge. But the question remains unsolved as to how much of this might be due to a cancellation between the confinement-related shifts of the structures and the underestimate of the higher absorption energies. Finally we note that our results have been corroborated by a later publication of Melnikov *et al.* who presented similar absorption spectra [221].

Occasionally, concerns have been raised as to the influence of the T_d symmetry on our results. We have, therefore, calculated the spectra of two highly non-symmetric NCs of somewhat arbitrary shape, which are shown in Fig. 4.23. From this we conclude that the main quantities, while modified, do not change qualitatively. In particular the strong transitions at the HOMO-LUMO gap of the Ge crystallite remain in place, whereas the Si NC shows the typical behavior of the Si NCs in Fig. 2.74. The excitation energies are included in Fig. 4.13 and do not deviate strongly from those of the NCs of T_d symmetry. The radius has again been chosen according to the volume, cf. page 40. Finally, a test calculation has been carried out for a free hexagonal Ge NC. Its excitation energy is also contained in Fig. 4.13. We conclude that the specific shape and the structure of the NCs is of relatively little importance for the excitation energies, at least as compared to the confinement.

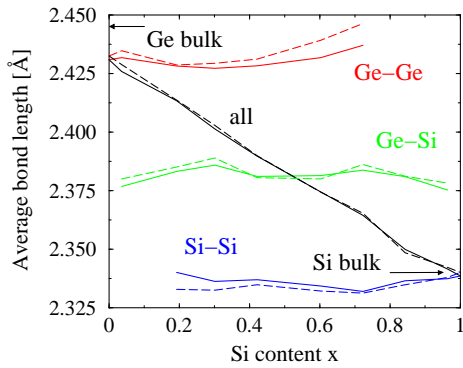


Figure 4.24 Average bond lengths in relaxed $\text{Ge}_{1-x}\text{Si}_x$ crystallites. Solid lines: ground-state, dashed lines: excited NC with one electron-hole pair. The arrows indicate the bond lengths in bulk Ge and Si.

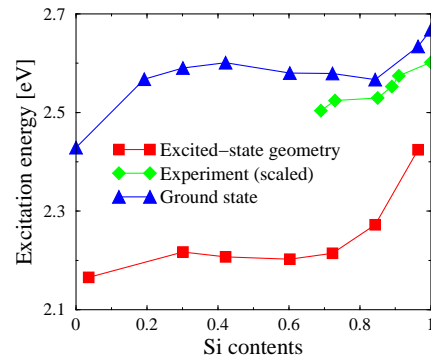


Figure 4.25 Lowest electron-hole pair excitation energies calculated for the ground-state geometry (triangles) and the geometry of the excited state (squares) as well as the rescaled experimental PL peak energies [22] (diamonds).

The comparison with the experimental results shows that the main features of the absorption can already be described well, in spite of the simplicity of our structural model and of neglecting important effects like quasiparticle corrections and excitonic effects. Moreover, we have not attempted to model the size distribution of the nanoparticles in the samples studied experimentally.

4.2 Alloying: Germanium and Silicon

The optical properties of alloy NCs depend on the composition x as well as on the particle size. This has been demonstrated by studies of nanometer-sized $\text{Ge}_{1-x}\text{Si}_x$ quantum dots in mesoporous silica [222] or in an amorphous SiO_2 matrix [22]. One observes a redshift of the PL peak with increasing Ge content. At the same time, the radiative lifetime decreases dramatically. The peak shift may be related to the nearly linear composition variation of the interband transitions in bulk $\text{Ge}_{1-x}\text{Si}_x$ crystals [218]. However, the substantial shortening of the exciton lifetime needs a deeper understanding. In general, both properties are influenced by the unknown interplay of confinement and alloying effects.

Alloying is introduced by randomly replacing Ge atoms by Si. Ionic relaxation is carried out both for the ground state and the excited state. The majority of the calculations has been performed for crystallites with 83 group-IV atoms and a diameter of about 1.5 nm. These are large enough to exhibit the characteristic features of a NC [144], but are still feasible for *ab initio* ionic relaxation.

We have studied NCs with 16 Si and 67 Ge atoms for about 10 different atomic configurations. Those with nearly uniformly distributed atoms possess the lowest total energies and nearly equal excitation energies. Nanocrystals with deliberately clustered Si atoms and, hence, rather different excitation energies give rise to total energies deviating by up to 10 eV from the average. According to the quasi-chemical approximation [223], their probability of occurrence

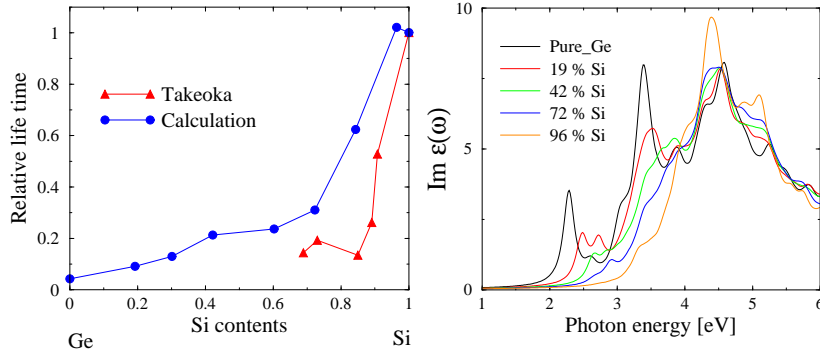


Figure 4.26 Relative radiative lifetime vs. composition. The values are normalized to those of the pure Si NCs. The experimental values of Takeoka *et al.* have been measured for larger NCs [22].

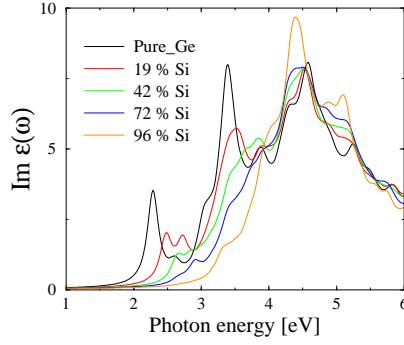


Figure 4.27 Dielectric function of GeSi NCs of variable composition.

is small. Consequently, the configurational average has been replaced by the study of one NC with nearly uniformly distributed Si and Ge atoms for each composition x .

10 test calculations have been performed for smaller crystallites of 41 atoms, for each of the two compositions $x = .29$ and $x = .73$. The variations of the pair-excitation energies for the ground-state geometry are small; we find ratios of $\Delta E_g^{\text{opt}} / \bar{E}_g^{\text{opt}} = .0065$ and 0.02 for the two compositions, ΔE_g^{opt} being the standard deviation from the mean value \bar{E}_g^{opt} . The variations for excited NCs are somewhat larger. The radiative lifetimes are much more sensitive to changes in the atomic configuration. We find variations of $\Delta\tau/\bar{\tau} = 0.55$ and 0.70 for the ground-state. For larger crystallites they will be smaller. The variations are largest near the pure ends of the composition spectrum, for the situation there is better characterized as a few impurities inside a Ge or Si crystallite rather than as an alloy.

The average lengths of the Ge-Ge, Ge-Si, and Si-Si bonds are shown in Fig. 4.24 and compared with the averages of all bonds. The trimodal distribution of the average lengths of the chemically different bonds is similar to that observed for bulk crystalline and amorphized $\text{Ge}_{1-x}\text{Si}_x$ alloys [224]. Besides the ground state, also the excited state with one electron-hole pair is studied. Optical excitation does not change the symmetry significantly within our static relaxation approach; no bonds are broken. The Ge(Si)-dominated bonds are slightly increased (decreased) with respect to the ground-state values. The opposite direction of the effect is apparently a consequence of the different symmetry of the wave functions of the electrons in the excited pairs, as it is known for bulk Ge and Si. The Ge-Ge, Ge-Si, and Si-Si bond lengths are nearly independent of the composition, corresponding to roughly the sum of the respective covalent radii. Like the bulk bond lengths, the bond lengths of the alloy NCs are closer to the Bragg-Pauling limit than to the Vegard limit [224]. However, the average bond lengths are smaller than the corresponding lengths in the bulk systems. Similar effects have been found experimentally [187, 192]. The average over the three types of bonds roughly follows Vegard's rule with respect to the reduced Ge-Ge and Si-Si bond lengths.

Results for the two types of pair energies are plotted in Fig. 4.25. As expected, the variations are rather large near the pure ends of the composition spectrum. The composition dependence of the energy E_g^{opt} of the ground-state geometry shows an S -shaped behavior resembling the familiar gap variation of bulk $\text{Ge}_{1-x}\text{Si}_x$ [223]. However, the difference between the pure-Ge and the pure-Si values is smaller than in the bulk, which is probably due to the lattice relaxation, cf. Figs. 4.12 and 4.13. We interpret this fact as an indication that the confinement does not

interfere strongly with the alloying effects. Comparison with the known bulk behavior shows that despite the confinement and, hence, uncertain \mathbf{k} vectors, the character of the indirect ΓX gap on the Si-rich side and the mixed character of the indirect ΓL and $\Gamma\Gamma$ gap for small Si molar fractions persist, as well as a gap crossing near $x=0.3$ [218]. The difference between the pair-excitation energies of Ge and Si is smaller than the difference of the bulk gaps, which is related to the bond-lengths reduction. Unlike for E_g^{opt} for the ground-state geometry, the composition dependence of E_g^{opt} for the excited-state geometries is non-monotonous. The Stokes shift has a nearly constant value of about 0.4 eV for NCs with a composition $x = 0.3 \dots 0.8$. As in bulk $\text{Ge}_{1-x}\text{Si}_x$ the change from a Ge-like gap to a Si-like situation occurs at about $x = 0.3$, we conjecture that the reason for this behavior is a change in the gap character as well. This will be corroborated in section 4.4.1 below.

The calculated pair energies in Fig. 4.25 can be compared with values measured in absorption or emission spectroscopy. Composition-dependent PL studies have been done only for $\text{Ge}_{1-x}\text{Si}_x$ NCs with average diameters between 3.8 and 4.7 nm [22]. The presence of oxygen is not expected to alter the results in this size range [45,46]. In order to compare with experiment, the PL positions have been rescaled using the approximate $1/d$ variation of the excitation energies with the diameter d found for both Ge and Si, cf. section 4.1.2. The rescaled experimental values agree well with the ground-state excitation energies rather than with the excited-state-geometry excitation energies due to the strong size dependence of the Stokes shift. While the latter is appreciable for our crystallites, it should already be negligible for the measured samples. Several arguments can be given to explain the remaining small discrepancies, in particular the validity of the assumed $1/d$ scaling law and the experimental determination of the NC diameter. In any case, the good agreement of the calculated energies and the rescaled measured PL positions indicates once more that the effects of composition and size are approximately independent; the measured redshift of the PL energy with the Ge content reflects the gap narrowing caused by the alloying [22].

We calculate the radiative lifetime τ , again by means of eq. (2.73). The results are plotted in Fig. 4.26 for various compositions and room temperature. The calculated values are compared with those measured for NCs with $x = 0.0 \dots 0.3$ and diameters between 3.8 and 4.7 nm [22]. In order to approximately separate the composition dependence from the size dependence, the values are normalized to that of the Si crystallite.

As mentioned above, the variations are rather large. Nonetheless, a roughly exponential behavior can be observed. The lifetime is longest for pure Si crystallites, reflecting the main contribution of bulk indirect-gap states to the optical transitions near the absorption edge. Consequently, with increasing Ge molar fraction the radiative lifetimes decrease strongly. The main reason is of intrinsic nature. Strong optical transitions corresponding to the allowed direct E_0 transitions in Ge crystals contribute and determine the radiative lifetime. The agreement with the experimental results is good despite the larger radii of the measured samples. As the radiative lifetime is strongly size-dependent, this is another indication that the size effect and the effect of the alloying act independently, at least in the range of Si molar fractions between $x = 0.0$ and 0.3. Takeoka *et al.* [22] conjecture that the decrease in the PL lifetime is caused by either an increasing density of defects or by the Ge-Si alloying. The agreement with our re-

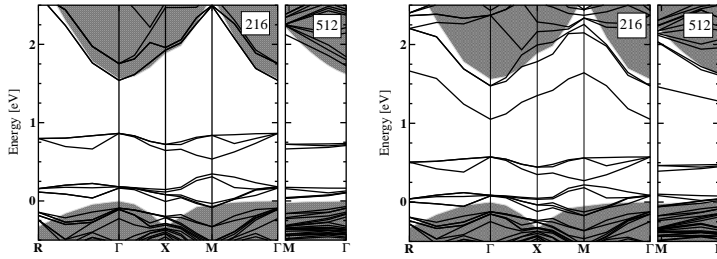


Figure 4.28 a) Band structure of the 41-atom Ge NC in a 216-atom cell, b) that of the same NC in a 512-atom cell. The host material is cubic SiC, the crystallite-host interface is Ge-C. The folded bands of the pure host material, SiC, are represented by the shaded regions.

Figure 4.29 a) Band structure of the 41-atom Si NC in a 216-atom cell, b) that of the same NC in a 512-atom cell. The host material is cubic SiC.

sults indicates that the alloying is the dominating effect. Nonetheless, additional effects have to be discussed. The ratio of the lifetimes of Ge and Si is strongly size dependent for diameters between 5 Å and 25 Å. The end points of the lifetime curve are expected to be further apart for bigger crystallites, making the curve steeper. On the other hand, a constant background of defect recombinations would render it less steep. Besides, an x -dependent defect density would lead to unpredictable results.

4.3 Embedment of the NCs

4.3.1 Electronic properties

The effect of the insertion of a Ge or Si NC into the SiC host material on the electronic structure is demonstrated in Figs. 4.28 and 4.29 for the 41-atom structures. For both group-IV materials, NC-induced occupied states arise in the lower part of the energy gap of the host material. Due to the supercell description, these states are not really dispersionless. They show a behavior similar to that of the defect bands in supercell calculations. While exhibiting the highest degeneracy at the Γ point, they split even along the high-symmetry directions into several bands according to their s - or p -like orbital character. The main structures of the SiC DOS have been used for the alignment of the band structures.

Since the interaction between adjacent crystallites decreases with decreasing spatial separation, the crystallite-induced bands become more dispersive. A comparison of results obtained for 216-atom and 512-atom supercells in Figs. 4.28 a) and b) shows that this is indeed the case. Clearly, the main features of the band structure close to the valence-band maximum (VBM) of SiC are the same for the 41-atom crystallite in the two different cells. This is a consequence of the strong Ge contributions to the corresponding wave functions which are, therefore, rather strongly localized. Comparing Figs. 4.28 and 4.29 we find that Ge and Si NCs behave differently in cubic SiC. For germanium, NC-induced states only occur as occupied valence states in the lower part of the fundamental gap, not, however, as empty conduction states closer to the conduction band minimum of SiC. The situation is radically different for silicon. There are empty crystallite-induced bands within the host band gap. They exhibit a dispersion similar to that of the folded lowest conduction band of bulk SiC. Within a simple quantum-confinement model this result may be interpreted such that confined holes arise in both the Ge and the Si NCs, while confinement of electrons takes only place in the latter system. Therefore, the system Ge

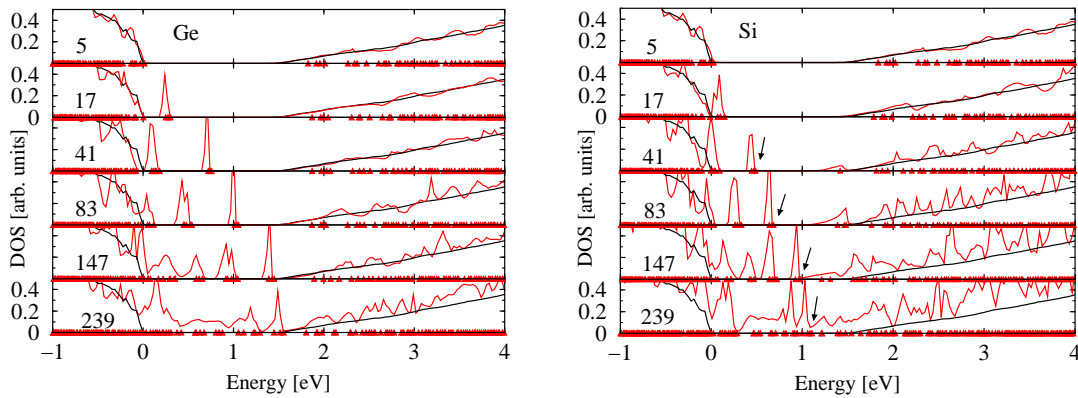


Figure 4.30 Density of states for NCs in SiC, as calculated in the 512-atom simple cubic cell for Ge NCs (with Ge-C crystallite-host interfaces) and Si NCs. Red line: NC-host supercell system, black: pure cubic SiC. The triangles indicate the electronic energies at the \mathbf{k} point used in the electronic structure calculation. The arrows point to the highest occupied states. The energy zero is defined by the VBM of SiC. The DOS has been calculated according to eq. (3.2) using the tetrahedron integration discussed in section 3.4.

in 3C-SiC is of a type-II heterostructure character, whereas Si in 3C-SiC is type-I. However, due to the low barrier and the small sizes of the NCs and of the supercells, the localization is by no means complete. Sizable portions of the Si-related wave functions extend into the host material. The corresponding bands are dispersive, indicating that the crystallite-matrix system acts more as a composite material. The strong mixing of Si and SiC states induces the splitting and shift of conduction-band states into the fundamental gap. The observed heterostructure character is, in principle, in agreement with results of Harrison's tight-binding model [225]. The conduction-band minima of the two materials give rise to a nearly flat band line-up.

Looking at the electronic density of states (DOS) one finds that the results for the 41-atom inclusions are representative for the other NCs that we have studied. The one-particle DOS for both Ge and Si crystallites in the 512-atom cells are plotted in Fig. 4.30. For comparison, the DOS of the pure host SiC is also shown. The main SiC-related peaks have been used for the energy alignment. The spectra depend on the number of atoms, which can be represented by a filling factor f , i.e., the ratio of the number of embedded atoms and the total number of atoms. Up to a crystallite size of 83 atoms, corresponding to a filling factor of $f = 0.162$, the DOS of the host material is conserved with regard to its main features. The ragged shape of the DOS indicates the transition from a system with extended states to one with partially localized states.

The DOS of Ge crystallites (with Ge-C interface) are shown in Fig. 4.30. The Ge-crystallites induce additional occupied states within the fundamental gap of the host close to its VBM. The number of these states increases with the crystallite size. Their positions shift to higher energies. This is in complete agreement with the prediction of a type-II heterostructure behavior. On the other hand, the DOS of the Si crystallites shows unoccupied states near the conduction band minimum, thereby verifying the type-I behavior. For the largest crystallites we have studied, those of 147 and 239 atoms representing filling factors of $f = 0.287$ and $f = 0.467$, the main bulk features of the host disappear; the gap is not clearly recognizable and filled with states, both occupied and unoccupied. Therefore it is not possible to draw simple comparisons between extended and localized states as in the case of the smaller crystallites. This is not surprising. For the large filling factors of the order of 0.5 it is clearly not a good model to think

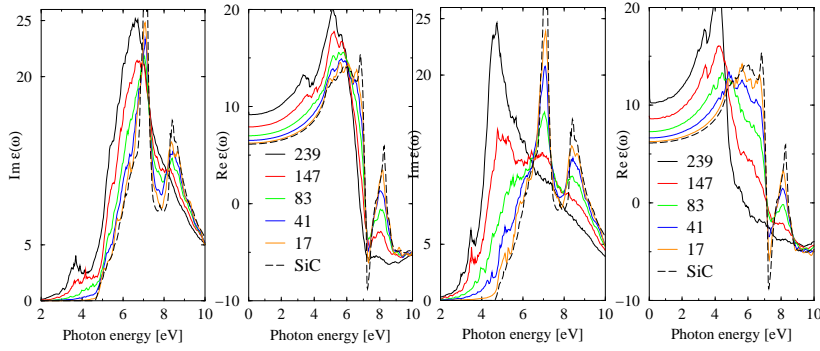


Figure 4.31 Dielectric function $\epsilon(\omega)$ of Ge embedded in cubic SiC with Ge-C crystallite-host interface in a 512-atom cell. The respective number of Ge atoms is as indicated.

Figure 4.32 Dielectric function $\epsilon(\omega)$ of Si embedded in cubic SiC in a 512-atom cell. The respective number of Si atoms is as indicated.

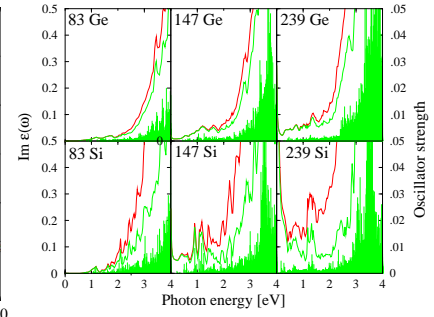


Figure 4.33 Contribution of the *occupied* gap states to the imaginary part of the dielectric function of Ge crystallites with Ge-C crystallite-host interface and of Si NCs embedded in cubic SiC in a 512-atom cell. Green line: gap-state contribution; red line: imaginary part of the total dielectric function. The oscillator strengths of the optical transitions involving the gap states are indicated by vertical lines.

of the crystallites as being embedded in some host material without changing its properties. Rather, the systems under consideration represent composite materials with an inhomogeneous distribution of the atomic species.

Recently, Luppi *et al.* have applied a similar model for embedment of strained Si clusters in SiO_2 [42, 226, 227]. Their results are similar to ours with respect the band structures, although their localized states show less dispersion due to the larger gap of SiO_2 .

4.3.2 Optical spectra

The dielectric function of the supercell systems obtained by means of the tetrahedron integration discussed in section 3.4 are shown in Figs. 4.31 ff. With increasing size of the NCs there is a significant deviation from the spectra of the pure cubic SiC [162]. The high-energy SiC peak with mixed E'_1 , E'_0 , and $E_2 + \delta$ character, located at about 9 eV in the DFT-LDA absorption spectrum, is strongly reduced. For the larger crystallites of 147 and 239 atoms it vanishes altogether. This is in agreement with the result that the DOS loses its clearly recognizable host bulk features for these filling factors. Despite the difference in their heterostructure behavior, the spectra of Ge and Si crystallites develop similarly with varying crystallite size. The difference spectra (not shown) for both types show strong negative peaks at about 7 and 8.5 eV which do not change their energetical position with increasing crystallite size. We attribute these peaks to the vanishing of the SiC bulk properties discussed above. A deeper discussion and effective-medium treatment can be found in Weissker *et al.* [48].

The lower-energy SiC peak at about 7 eV decreases and shifts to smaller photon energies. It does so more strongly for Si than for Ge. For the largest crystallites the absorption tends to become similar to results found for compressed Ge and Si, cf. page 58. Comparing the shifts and the difference spectra for the Ge crystallites it can be seen that the main structure between about 5 and 8 eV is attributable to the increasing amount of crystallite material. Its shift seems

to be unaffected by spatial confinement and corresponds to the spectrum of the compressed Ge in Fig. 3.29.

The most interesting part of the spectra lies below the main structures discussed above. Below 4 eV there are additional shoulders developing into peaks which are strongly affected by quantum confinement effects. In the Ge case, a more or less monotonous shift to lower energies can be found with increasing crystallite size. The peak positions are 4.1, 3.8, and 3.7 eV for the crystallites of 83, 147, and 239 atoms, respectively. This peak might become the E_1 structure in unstrained bulk Ge. For Ge such a shift has been predicted [228, 229]. For the Si crystallites, on the other hand, no simple description of the low-energy shoulders and peaks can be given.

In order to understand these features in more detail we study the influence of the gap states. In Fig. 4.33 the contribution of the occupied gap states to the dielectric function within the optical gap of the host are presented. In order to do this we have restricted the summation over the valence states in expression ((2.71)) to a summation over the gap states. Below 4.5 eV for Ge and 4 eV for Si NCs, the spectral properties are determined solely by the gap states. Fig 4.33 shows the oscillator strengths of the transitions against the respective transition energies. For Si the transitions between the highest occupied valence states and the lowest conduction states (cf. Fig. 3.2) have only very low oscillator strengths. However, they give rise to a structure at a photon energy of about 1eV. The imaginary part of the dielectric function below 2 eV is at most of the order of 1% of the maximum. Even though the Si crystallites in cubic SiC tend to constitute a type-I system, the transition probabilities of the lowest transitions remain small. This is the reason why the overall dielectric function in Fig. 4.32 does not strongly reflect the different heterostructure character as compared to Ge. We note that the transitions from the gap states do not occur into the CB edge but much higher into the CB. The effect on the luminescence properties might, at this point, only be conjectured at. However, it could be worthwhile to search for an infrared emission after illuminating Si / cubic SiC systems.

4.3.3 Hexagonal matrix and NCs

As shown above, embedding Ge in cubic SiC results in a type-II heterostructure. Hexagonal SiC has a larger gap than the cubic polytype. Therefore, embedding Ge in hexagonal 4H-SiC is expected to produce localization for both holes and electrons. From the calculations of the free, hydrogen-terminated NCs we know that Ge has strong transitions at the bottom of the spectrum. This leads to the expectation that Ge embedded in hexagonal SiC should give rise to a heterostructure suitable for luminescence.

In Fig. 4.34 we show that, in fact, Ge in 4H-SiC is a type-I system. The density of states shows both occupied and unoccupied localized states. However, in spite of the resulting overlap, these states do not appreciably contribute to the absorption spectrum in Fig. 4.35. In view of the results for the free hydrogen-terminated crystallites with their strong transitions at the HOMO-LUMO gap, these results are surprising at first. Considering the differences between the two systems it becomes clear that the strain in the NCs plays an important role.

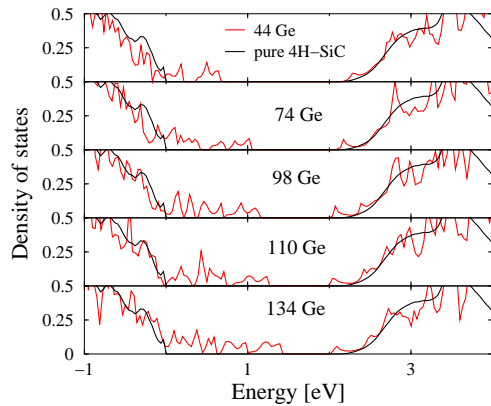


Figure 4.34 Density of states of Ge NC in hexagonal (4H) SiC. The cell contains 576 atoms.

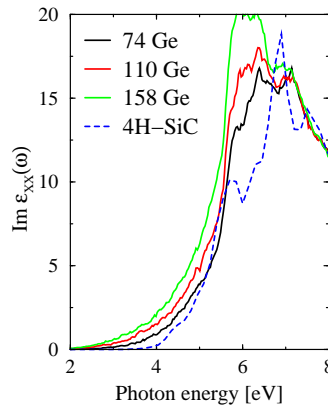


Figure 4.35 Dielectric function of Ge NCs embedded in hexagonal SiC, compared with the spectrum of the pure host material.

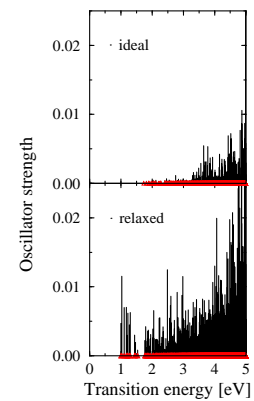


Figure 4.36 Oscillator strengths of a 17-atom Ge NC in cubic SiC for ideal and relaxed structure. (216-atom cell.)

4.3.4 Influence of relaxation

As a first step to understand the influence of the strain we relax the model structures. The possibility to "switch on" structural relaxation and to compare the results of the respective calculations with those of the ideal structures permits to infer quantitatively the influence of the relaxation on the optical properties. While it is intuitively clear that the compressed Ge will expand and compress the host material in its vicinity, it is not *a priori* clear at what lattice constant of the supercell system the relaxation should be done. The system which one seeks to describe is the isolated Ge crystallite in an infinitely large matrix. The choice of supercells of a certain size is dictated by methodological necessity. The imposition of the host lattice constant as the lattice constant of the supercell system is unphysical because it neglects the expansion of the material, leaving it only free to relax within the supercell whose dimensions are, however, arbitrary and only dictated by numerical limitations. On the other hand, a calculation of the supercell system's equilibrium lattice constant is unphysical for the same reasons. Therefore we restrict ourselves at this point to a presentation of the results for the unrelaxed structure and for the structure relaxed at the host material's lattice constant and the equilibrium lattice constant of the supercell system.

The structural relaxation pattern of NCs is complex. In Fig. 4.37 the individual bond lengths are shown in dependence on their distance from the center of the crystallites. Trivially, the compressed Ge-Ge bonds are shorter than their bulk values. Interestingly, however, the bonds are shortest at the center of the crystallite, while their lengths increase towards the crystallite-host interface. This is the opposite behavior as for the free NCs, cf. Fig. 4.2. The bonds between Ge and the host (in this case, these are Ge-C bonds) have lengths intermediate between the host-host and the Ge-Ge bonds. The host-host bonds are shorter compared to their bulk lengths because of the compression. The situation is not significantly different for the relaxation at the equilibrium lattice constant, except for larger bond lengths in general.

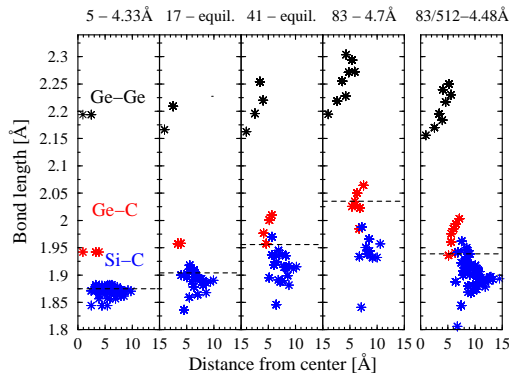


Figure 4.37 Bond lengths after relaxation at equilibrium lattice constant: Ge in SiC, 216-atom cell. The horizontal lines indicate the bulk interatomic distances. Last panel: 512-atom cell.

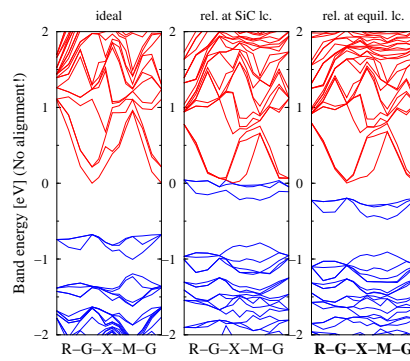


Figure 4.38 Influence of relaxation on band structure: 41-atom Ge NC in SiC, 216-atom cell. Blue: occupied, red: unoccupied bands.

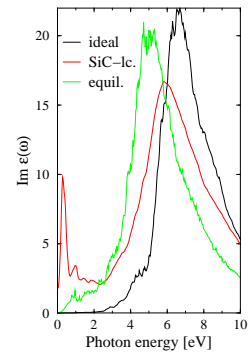


Figure 4.39 Influence of relaxation on spectra: 83-atom Ge NC in 3C-SiC, 216-atom cell.

However, the electronic properties change strongly. In Fig. 4.38 we present the band structures for the ideal and the two relaxed geometries. Obviously, the gap states show strong dispersion. Hence the NCs in different cells interact; the calculations are not converged with respect to the amount of surrounding matrix material. However, the trends for all quantities presented here are similar for all the systems, and cell sizes, which have been investigated. Therefore we chose the present system which shows the effects particularly strongly because of the high filling factor. Moreover, the problems in the present form of the modeling are particularly clearly understandable. In the larger cells, the dispersion of the gap states is strongly reduced.

The relaxation at the host material's lattice constant shifts the (occupied, cf. Ref. [143]) gap states of the crystallite to higher energies. In the present system this goes as far as to make the system metallic, as can be seen from the band structure of Fig. 4.38. If, however, we change the lattice constant to the equilibrium value, the gap states shift down again in energy, not, however, as far as to re-attain their old energetical positions.

We alert the reader to the fact that there is, at this point, no basis for an alignment with the bulk band structure of the host material. As can be inferred from Fig. 4.37, due to the large filling factor there is nowhere in the system unstrained host material. On the other hand, all the band structures are pressure dependent. The relative energetic positions of the bands are undefined between the three systems in Fig. 4.38. The bottom of the conduction band has been chosen as the energy zero for all three panels.

The optical properties of any system are, for the largest part, determined by the band structure. Hence the changes in the bands will translate into effects in the optical spectra which are presented in Fig. 4.39. Here we do not have any alignment problem because we treat only energy differences. In accordance with Fig. 4.38, the onset of the absorption is drastically reduced for the relaxed structure with respect to the ideal-structure result. The behavior at energies close to zero reflects the fact that the system becomes essentially metallic for the relaxation at imposed host lattice constant. As the cell is allowed to expand to its equilibrium lattice constant, the onset of the absorption is blue-shifted. The shape of the whole spectrum is also changed.

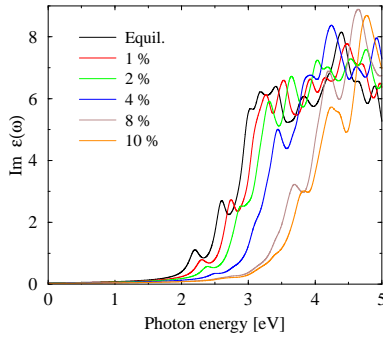


Figure 4.40 Imaginary part of the dielectric function calculated for the 83-atom hydrogen-terminated Ge crystallite for strain values as indicated. A broadening of 0.1 eV has been applied.

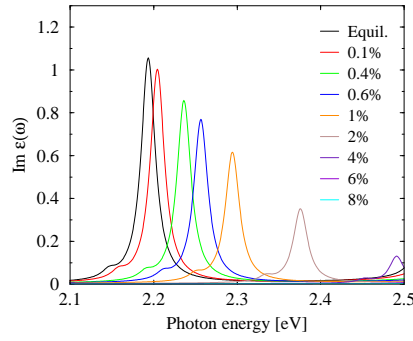


Figure 4.41 Blow-up of the region of the first peak in Fig. 4.40.

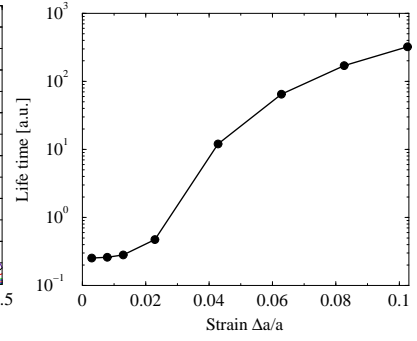


Figure 4.42 Radiative lifetimes for the 83-atom hydrogen-terminated crystallite as a function of the compressive strain.

The influence of the relaxation on the oscillator strengths is shown in Fig. 4.36. Due to the distortions as compared to the ideal structure, the transitions become stronger. However, they remain very small as compared to the transitions relevant to the optical properties, cf. Fig. 2.74. Thus the relaxation alone cannot yet explain the difference between the behavior of the free and the embedded NCs.

4.4 Beyond the Ground-State Equilibrium

4.4.1 Pressure/Strain

While the simple relaxation of the embedded model structures gives some indication of the importance of the strain, it does not resolve the discrepancy between the results for the free and the embedded Ge NCs. Therefore we consider now explicitly the pressure (or strain) dependence of the Ge NCs.

In Fig. 4.40 the imaginary part of the dielectric function of the hydrogenated cubic Ge NCs is shown for different hydrostatic pressures. Pressure (or hydrostatic strain $\Delta a/a$) is modeled by reducing the interatomic distances a . For zero pressure the spectrum shows the familiar strong feature at the absorption onset. However, with increasing pressure this part decreases rapidly. Correspondingly, the radiative lifetimes eq. (2.73) will increase strongly. This is shown in Fig. 4.42.

The high hydrostatic pressure means that the radii of the crystallites become smaller. Taking into account the fact that the lifetimes become shorter with decreasing NC size it is clear that there is some contribution to the lifetime curve in Fig. 4.42 which is due to the size effect. The pure pressure dependence separated from this effect is an even stronger increase in the lifetimes.

In order to explain the pressure dependence of the optical properties we turn to the pressure dependence of the HOMO-LUMO gap. Shown in Fig. 4.43 (b) it includes again contributions from both the pressure and the size dependence. Similar to the procedure for the GeSi alloy

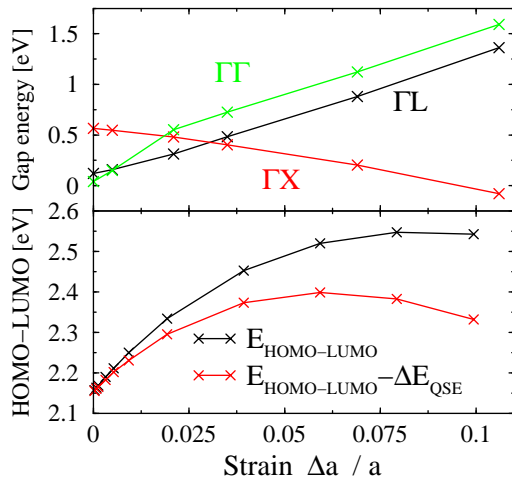


Figure 4.43 (a) Strain dependence of the different gaps in cubic bulk Ge. The crosses represent the calculated values. The values are taken from Raffy *et al.* [230]. (b) Strain dependence of the HOMO-LUMO gap calculated for the 83-atom Ge crystallite. The black line gives the energies as calculated, the red line those corrected for the size effect as explained in the text. Note the different energy scales.

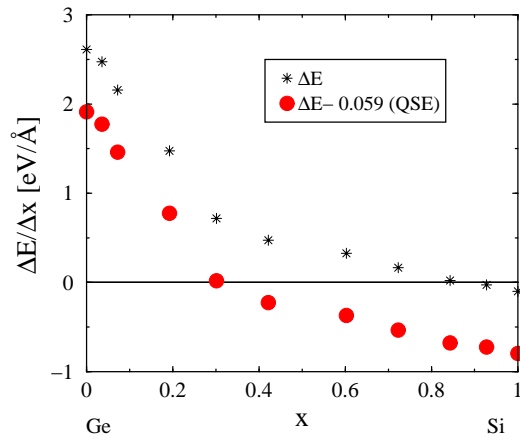


Figure 4.44 Pressure dependence: Excitation energies of GeSi alloy NCs. The black stars give the values as indicated, the red circles the values corrected for the quantum-size effect (QSE) due to the change in volume.

NCs, the curve is, at least approximately, corrected by subtracting the energy difference found from the size dependence of the unstrained crystallites [144] between the gap energies of the unstrained radius and the radius reduced by the pressure. The corrected curve is also shown in Fig. 4.43 (b). After increasing with increasing pressure it reaches a maximum at about $\Delta a/a=6\%$ compressive strain and then decreases. This can be explained as follows. Both the pressure and the quantum size effect will change the contributions from the different bulk states. We can compare our HOMO-LUMO gaps of the crystallite of $R=15 \text{ \AA}$ to the pressure-dependent gaps of bulk germanium in Fig. 4.43 (a) [230]. Assuming that the differences between the bulk and the NC gap behavior are not extreme we get the following picture. At zero pressure, the Γ - Γ gap and the Γ -L gap lie very close in energy. Hence, the states relevant to the LUMO state will correspond mainly to the Γ and L bulk states. With increasing pressure the Γ - Γ gap increases above the Γ -L gap but remains at roughly constant energetic separation from the Γ -L gap up to very high pressures. However, at about $\Delta a/a=3\%$ the Γ -X gap becomes the smallest, lying increasingly below the Γ -L and Γ - Γ gaps. This means that, in the high-pressure regime, conduction band states from the X-point will contribute most to the LUMO state of the NC energy scheme, while the Γ -contribution decreases due to the increasing energetic separation. The vanishing contribution of the Γ - Γ -transition makes the HOMO-LUMO transitions very weak and results in the strong increase of the radiative lifetimes. The situation is very similar for hexagonal Ge [230].

Most interestingly, also the difference between Si and Ge NCs can be explained in this way. The Γ -X-gap which corresponds to the low-probability transitions in Ge at high pressure is the lowest gap in Si for the whole pressure range (not shown). From Fig. 4.43 we predict the pressure coefficient of the HOMO-LUMO gap for Ge crystallites in the considered size

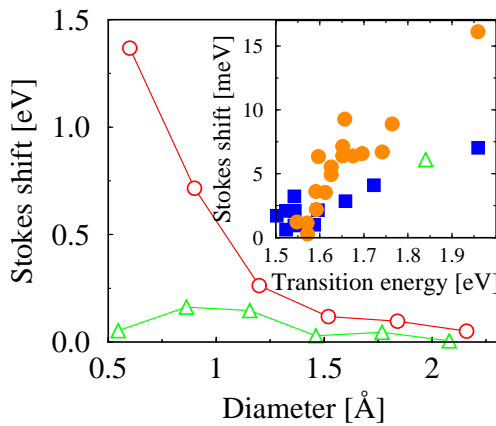


Figure 4.45 Structural contribution (see text) of the luminescence Stokes shift for Si (triangles) and Ge (circles). The inset shows shifts measured for resonant excitation versus excitation energy for H-terminated porous Si (filled squares) and surface-oxidized Si NCs (filled circles) [116], along with the calculated value for the largest NC (triangle). T_d symmetry is stipulated.

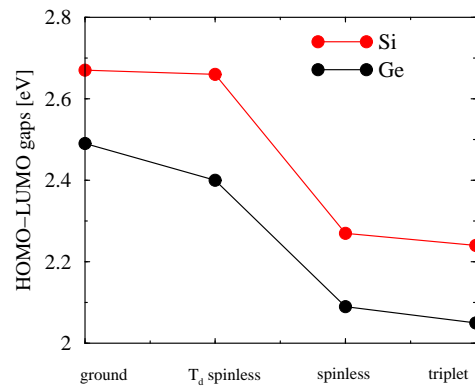


Figure 4.46 HOMO-LUMO gap of Ge and Si NCs: Influence of the symmetry lowering by the excitation. Shown are the HOMO-LUMO gaps for the ground-state relaxation and the T_d relaxation without spin polarization. Free symmetry gives a larger Stokes shift for the structural relaxation with both a “spinless”, i.e., non-spin-polarized, and a triplet excitation. The influence of the spin polarization is weak.

range to be positive. This result disagrees with the findings of reference [39]. While perhaps in our approach we overestimate the contribution of the Γ - Γ -transition, the transferability of the empirical pseudopotentials down to NC sizes of 1-2 nm seems questionable and should be considered with care [231].

After these findings and the experience with the alloy NCs in section 4.2 we corroborate our interpretations by considering the pressure dependence of the HOMO-LUMO gap of GeSi alloy NCs. Changing the interatomic distances, again there is the change of the NC volume and the corresponding confinement-related positive shift. After subtracting this, the result as shown in Fig. 4.44 is obtained. The behavior changes smoothly from the pure-Ge to the pure-Si behavior, with the crossover at about $x = 0.3$. The negative pressure dependence of the PL peak energies for Si NC samples has been measured by Cheong *et al.* [232].

This shows, once more, that the confinement and the alloying act approximately independently. Moreover, also the pressure dependence can be considered separately. The change of the gap character is also another corroboration of the interpretation as given in section 4.2.

4.4.2 Stokes shifts

The Stokes shifts are calculated according to equation (2.61) in section 4.4.2. The contribution due to the structural relaxation encompasses two different effects. There is the volume-like structural relaxation which is consistent with the assumption of T_d symmetry. This part of the effect is similar to the breathing mode in defect physics. Second, there is the effect which is due to a possible symmetry break after the excitation, as recently discussed by Puzder *et al* [233]. Of course, both effects are not independent. The fixed-symmetry structural contribution

to the Stokes shift represents the lower limit of the Stokes shifts. Additional non-symmetry-conserving relaxations further lower the total energies. As the size of the crystallites increases, the crystallite will be increasingly better described as having a bulklike interior and a surface governed by surface phenomena.

Moreover, the hydrogenated crystallites have always been thought of as a model for both free crystallites (which they really are) as well as for crystallites embedded in a matrix with a very large gap. In the latter case, there will be some symmetry stabilization, depending on the interface region. In dependence of this, the value of the real structural contribution to the Stokes shift will lie between the free-symmetry and the symmetry-restrained results.

The difference between the energies of the ground-state and the excited-state geometry, i.e., the structural contribution to the Stokes shift, is shown in Fig. 4.45. No attempt has been made to model the contribution related to the size distribution of the NCs. The contribution plotted in Fig. 4.45 is, therefore, only directly measurable in resonance experiments, in which only NCs with a definite size are excited.

Unfortunately, direct comparison with experimental Stokes shifts is difficult because measured values contain all the discussed effects, in particular the contribution due to the size distribution of the NCs. Nonresonantly measured Stokes shifts can be as large as 1 eV for Si NCs in a SiO₂ matrix [234]. For a resonant excitation of Si NCs, much smaller Stokes shifts of the order of a few meV and up to 50 meV are observed [116]. The inset of Fig. 4.45 with Stokes shifts as a function of the excitation energies demonstrates that our calculated Stokes shifts for the largest NCs are close to values measured resonantly for H-terminated porous Si. The shifts for surface-oxidized Si NCs are only slightly larger than the calculated value for the NCs corresponding to this transition energy.

In order to go beyond the symmetry-constrained calculations we did tests shown in Fig. 4.46 which indicated the following: For the 83-atom NC, the T_d Stokes shift is particularly small with 0.03 eV. This might be a consequence of the model of the particular crystallite.

An excited-state relaxation of the same NC but without the symmetry constraint yielded a pair excitation energy of 2.1 eV, making the Stokes shift about 0.4 eV. Hence this crystallite has not yet reached the size regime where the symmetry-keeping volume contribution is dominant. This is shown in Fig. 4.46 and in rough agreement with very recent results of Franceschetti *et al.* [115]. However, the fact that the Stokes shift of our largest crystallite agrees fairly well with experiment seems to be an indication that in this size regime (about 2.5 nm diameter) the symmetry break is already supplanted by the fixed-symmetry contribution as the main cause of the structural part of the Stokes shift.

Over the whole range of sizes, the fixed-symmetry structural Stokes shift is much larger for Ge than for Si. While for Ge even for the diameter of 2 nm the shift is appreciable, for the corresponding Si crystallite it has the tiny value of 5 meV. The differences between Ge and Si are a consequence of the different symmetries of the electron-hole pairs in Ge and Si crystallites due to the different physical character of the contributing single-particle states, especially to the LUMO states due to the different bulk band structures. Moreover, the bonding in Ge NCs is weaker than that in Si. Consequently, the geometrical changes due to the electron-hole pair

can induce larger changes in the excitation energies. Thus it is no surprise that the structural contributions to the Stokes shift are different for the two materials.

It is clear from the foregoing discussion that the description of the excited-state structural effects will be an important field of research in the future.

Chapter 5

Conclusion and Prospectives

The present work provides contributions to both fundamental and practical questions. We have investigated the structural, electronic, and optical intrinsic properties of Ge and Si nanocrystals. Using bulk-fragment-like, H-terminated model structures, we have focused our attention on the mechanisms and properties due to intrinsic effects. The work aims at the general tendencies and dependencies in NCs. In particular, we have been able to describe the interconnection (or, more precisely, the mutual independence) of different effects like strain, alloying, and confinement.

The modeling of NCs is not yet a very evolved field, though the results of the last few years give many indications as to the direction in which the development will lead. Most practically relevant systems treat NCs embedded in some crystalline, amorphous, or maybe fluid surrounding. Depending on the height of the potentials as well as on the line-up, different heterostructures are created, with confinement of either both the excited electrons and the holes, or just one of them. Our H-terminated model structures are considered both a model of NCs embedded in some matrix with a large gap, and, second, free NCs *per se*. We have investigated the structural relaxation pattern of the NCs. By considering the influence of the relaxation on our target quantities we have shown that ionic relaxation is an indispensable part of NC modeling. Especially the radiative lifetimes proved highly sensitive to the relaxation. This is a technical point, important though it is. The answers given here will aid future modeling, but are not, by themselves, a description of actual physical effects.

Using the relaxed structures, we calculated the transition probabilities and, closely connected, the radiative lifetimes as relevant for a PL experiment or application. It has been shown, in agreement with related results of other groups [209] that Ge nanostructures appear to be better suited for light emission than Si NCs, at least as long as quasi-direct transitions are the main contributors. We were able to explain this in terms of the composition of the HOMO and the LUMO states with respect to the bulk band structures. Comparison with experimental values revealed, once more, a large spread of the measured values. Future work will have to explain why, at least until now, luminescence has been achieved more readily from Si NCs, rather than from Ge NCs. This might be explicable by the fact that most of the transitions in Si are phonon or defect assisted. Lately it has been shown for small NCs that the heterostructure picture is to be, if not supplanted at least complemented, by interface-, reconstruction-, and defect-related

effects. All comparison between experimental and theoretical results suffers from the strongly varying properties of the experimental samples.

One of the main points of this work has been the calculation of excitation energies. While the description of excitations in bulk systems is already rather sophisticated, it is still not completely clear what the “correct” description of NC excitations is. Available theoretical data spread over a band of about 3 eV — on the scale of 10 eV in total! Unfortunately, the experimental situation is no different. Very few results are available where the assignment of particular properties to particular effects or structures is corroborated beyond reasonable doubt. Thus, to date, the theoretical results for NCs in the intermediate size range remain often predictive and can only be discussed in term of their advantages and drawbacks. We have calculated the excitation energies by means of a Δ SCF method using an occupation constraint. This method is superior to the older Δ SCF method used for Si NCs for physical as well as for purely practical reasons which include the simultaneous description of electron and hole, as well as the faster convergence with respect to the cell size. In the last two years, this approach has become widely used. Our method is known to underestimate the excitation energies in the bulk limit.

Frequently excitation energies are discussed in terms of some functional dependence on the diameter of the NC. For instance the somewhat archaic effective-mass approximation yields, for a spherical square-well potential, excitation energies proportional to d^{-2} . There is agreement now in the literature that the exponent is smaller. We obtained values of about -1.0 for both Si and Ge. However, careful consideration of the limits $d \rightarrow 0$ and $d \rightarrow \infty$, or of different choices of the size range of NCs taken into account, shows that a simple fit cannot account completely for the true relation. The reason for this is unknown, but it appears likely that in particular the transition from spatial confinement to bulk-like relative localization of electron and hole changes the respective dependencies.

The results of our Δ SCF method have been found to be extremely close to the LDA eigenvalue differences, deviations becoming important, if at all, only for the smallest localization radii. While this is, in general, explained by the cancellation of the Coulomb interaction and the self-energy effects, a tentative correction of our values using the correction as calculated by Delerue *et al.* gave a rather clear overestimate of the values for larger radii. At present it seems that only the explicit incorporation of at least the self-energy effects and the electron-hole interaction will be able to finally settle the questions about the excitation energies in NCs of intermediate size. Until then our method provides a rather well investigated tool for the practical calculation of excitation energies.

Using spin-polarized calculations, we have been able to calculate the exchange splitting between the singlet and the triplet excitons. The calculated values agree rather well with available experiment, although for small radii the splitting is underestimated, likely due to the incapability of the employed LSDA exchange-correlation potential to describe pure multiplets.

Experimental PL results are easier to come by, but they are most strongly influenced by defects, dangling bonds, etc. Experimental absorption spectra are few and far between, as they are harder to obtain. Their advantage is that they are less sensitive to the aforementioned

effects. Therefore they account more easily for the quantum-confined optical transitions. Good qualitative agreement has been found between our *ab initio* results and experimental spectra.

Test calculations using NCs of arbitrary shape have shown that the main results of this work are not valid only for the crystallites of T_d symmetry, but are general. This holds in particular for the strong lowest transitions in Ge NCs.

For the first time an *ab initio* method has been applied to an alloy on a nm length scale. We have shown that the alloying of Ge and Si leads to effects which act – at least approximately – independently from the confinement. The electronic and optical properties change smoothly for changing composition, and the change reflects the change in gap character between Γ - Γ and Γ -L for Ge NCs, and Γ -X for Si. This has been corroborated using the pressure dependence of the excitation energies for alloy crystallites. Calculated lifetimes showed that the changes as found in experiment are due to intrinsic effects rather than to defects, clarifying the experimentalists' interpretation. The structural relaxation of the GeSi alloy NCs takes place such as to roughly follow Vegard's rule.

In order to improve upon the H-saturated model for embedded NCs, we embedded Ge and Si NCs in a crystalline matrix using a simple replacement of atoms resulting in strongly strained structures. This has been the first *ab initio* calculation for such a structure. Recently, a similar model has been used by Luppi *et al.*, suffering from a similar strain problem as ours. This is the only other *ab initio* treatment of embedded NCs besides our work. The heterostructure character especially of Ge NCs in cubic SiC has been determined to be type II.

A description of the properties of the composite system NC plus matrix has been possible using an extrapolative version of the tetrahedron method. For this we implemented an extrapolation using second order $\mathbf{k}\cdot\mathbf{p}$ -theory and a subsequent resampling, applicable for supercell systems. The number of \mathbf{k} points could be reduced to just one, at least for T_d cubic supercells. The method has been used in the description of the spectral properties of the embedded systems. Embedment of Ge in hexagonal SiC with a large gap resulted in a type-I heterostructure, but, contrary to expectation, no strong transitions between the band edges were found; the influence of the NCs on the dielectric function was minimal. However, ionic relaxation of the strained systems slightly improved the transition probabilities, leading to the understanding that the strain or pressure dependence of the material's properties was the reason: Our embedded model structures were not able to reproduce the experimental situation in terms of strain and, therefore, neither the optical and luminescence properties. Tentative steps in order to obtain a better model have shown that this improvement is a highly non-trivial task.

Subsequently, the pressure dependence of Ge NCs' properties has been found to be determined by a bulk-like pressure dependence of the direct and indirect gaps, leading to a strong change in the respective contributions to the composition of the NC states. Under high pressure, Ge NCs become Si-like, i.e., in the experimentalists' language: indirect. The change under pressure remains valid independently of alloying as well, corresponding to the different contributions. From our results we conclude that also the pressure dependence and the confinement

act approximately independently, as does the alloying. We were able to explain our results in terms of a unified and consistent picture of these effects.

Finally, we have carried out excited-state ionic relaxations using a T_d symmetry constraint. Rather small Stokes shift contributions have been obtained in this way. On the other hand, discarding the symmetry restraint we obtained much larger shifts, in agreement with recent publications of other groups. Real embedded systems will experience some restraint due to the interface or surrounding. Our values thus indicate the lower bound for the shifts, for larger NCs, however, the main contribution. Hence it is necessary to consider the embedment and the interface structure in order to describe a given system's Stokes shift correctly. The change due to an inclusion of spin-polarization has been found to be small.

* * *

For many quantities, there is a lack of experimental results, in particular for Ge. Measurements of life times, spin splittings, excitation energies of quantum-confined excitons, etc. would be desirable. For this reason the present dissertation also hopes to raise the interest of the experimentalists in those questions. As especially Ge is a difficult case for the pseudopotential description, a corroboration (or, for that matter, also a refutation) of the present results would be valuable. Moreover, it must be finally found out why, until now, Si has been used more successfully to produce light emission than Ge. This might lead to new questions like the influence of doping in Si NCs [203, 235], or of electron-phonon coupling.

Until now, experiment has been simply described by using the electronic states in the model NC and transitions between them. A more specific description of experiments would be useful. For instance, for the the description of the Stokes shifts one will have to start from asking the question as to which experiment is to be described, involving which effects on which time scales, etc. Electron-phonon coupling will be needed in order to describe and explain many of the relevant optical effects, in particular in Si NCs.

As the experimental samples will continue to be diverse, a better insight into different effects having different signatures in the optical spectra or other properties is desirable. "Nano-science" will have to create some sort of data base in order to describe a given sample: Many effects occurring with a certain statistical likelihood make up the properties of a real system. If theory can supply an according description, it will also be successful in the *prediction* of material properties.

In order to achieve this, better growth models and more specific characterization methods have to be developed, comparable to those in surface physics: Highly sophisticated fabrication of a clean surface with a controlled number of controlled defects or reconstructions enables a detailed comparison with the theoretical description of a given effect. In particular, the model for embedding NCs in a host material has to be developed, especially for the interfaces. The available *ab initio* results suffer from serious drawbacks of the model. This is mainly due to the lattice mismatch of the constituent atomic species and the resulting compressive strain, as exemplified by the discussion of this thesis. The highly non-trivial task of constructing realistic models for the interfaces will has to be solved. It is likely that combined methods of empirical-potential molecular-dynamics and subsequent *ab initio* determination of the electronic and op-

tical properties will be used, the feasibility of which we have already started to investigate. This could involve partial melting of surfaces or interfaces, and subsequent cooling. The treatment of dangling bonds will be one of the key questions, both in theory and experiment.

This will be particularly helpful for the Ge/Si heterostructures which are of paramount importance for technology. Here, *ab initio* calculations are still rare because, as preliminary results have shown, the strain fields extend very far, requiring huge supercells (if the present approach is to be employed), and an intermixing has to be included almost certainly. Moreover, the alignment of the bands or the electronic potential between the strained supercell system and the practically infinite bulk must be enabled.

Another relevant question would be the development of a description of the mechanism of annealing after ion implantation, e.g., for Ge in SiC. This would be possible by the consideration of the mobility of the surplus atoms in the crystal lattice. As oxygen has proven to be very important, the modeling of structures including oxygen will also be pursued further, as will be the modeling of defects and surface reconstructions in NCs.

In the next years, there will be definitely further development of the tool box of condensed-matter physics, including application to NCs. Apparently, this will definitely include the electron-hole interaction in an appropriate manner, as well as local-field effects. The approaches will most likely include many-body perturbation theory based on GW + Bethe-Salpeter equation calculations, Time-Dependent DFT, and quantum-Monte-Carlo methods. This avenue of development should conclusively terminate the discussion about the excitation energies of NCs, the contribution of the self-energy effects depending on the radius, and also explain in better than heuristic terms the cancellation between self-energy effects and the Coulomb energy. In any case, the treatment of excitations will continue to be central to the field, among them the topic of Stokes shifts, and maybe also photo-induced chemical reactions including NCs.

In any case it is desirable to create some overlap for the scales on which the semi-empirical pseudopotential methods and the *ab initio* approach yield reliable results on a routine basis. No one method will be able, at least in the foreseeable future, to handle the systems over the whole size range. Neither is that necessary. For small sizes, *ab initio* techniques are applicable, and questions due to the confinement are the most relevant — among them Stokes shifts, etc. The latter necessitate the fully quantum-mechanical approach. For “very large” nanostructures, the empirical and semi-empirical approaches provide a reliable description of the properties.

It appears likely that a further separation between applied and fundamental nano-research takes place in the NC field. Theoretical research will continue to create better models for the description, along with experiment which will continue to create better and better defined crystallites. Applied research will, on the other hand, use its natural “engineering-type” of approach and work closely focused on practical results. In doing so it will use the results of fundamental science. (Here acts a peculiar feedback mechanism – the development of computer technique has greatly accelerated especially the progress in the field of computer simulation which in turn fosters the technological development.)

* * *

On a broader perspective, it is very likely that the overlap between organic chemistry and condensed-matter physics will increase. The systems treated using the methods developed in the context of NCs will include the interaction of nanocrystalline material with biological molecules and maybe surfaces and tissues. This will, on the one hand, depend on the present focus of publishing and funding agencies on what came to be curiously termed “life sciences;” on the other hand, however, on the marketability of respective research results. The latter effect extends into the realm of scientific publications, where a marketing-type style of presentation of scientific results is now not uncommon. Besides, the direction of the technological development will also be largely determined by considerations like availability of certain techniques, cost, funding of research, etc.

The focus in the field of computational materials science will in part continue to be on the “traditional” questions like device fabrication. On the other hand, it will likely embrace the field of medical and biological applications – implying all its promises and dangers and, therefore, questions of responsibilities.

* * *

Acknowledgments

I would like to thank all those who have, directly or indirectly, contributed to the present work.

First and foremost, I am grateful to my supervisor Prof. Friedhelm Bechstedt, whose ideas and motivation were vital to the present work, and whose support has greatly helped the positive outcome and the large amount of results. The many discussions about the work have helped to shape my physical understanding and the approach to the very topic of my thesis. Especially his openness and accessibility have been of great value, both with respect to the atmosphere and the results of the work.

Furthermore, I would like to thank my second supervisor Jürgen Furthmüller for his help in particular with the VASP package.

On the official side, I thank the respective funding agencies for the financial support which has made this dissertation possible. The present work was supported within the Sonderforschungsbereich 196, Project No A8, and, later, within the Project No. Be1346/12-1 by the Deutsche Forschungsgemeinschaft, as well as within the Training Research Network (Contract No. CT-2000-00167) of the European Community.

Moreover, it is a pleasure to acknowledge the technical support I have received from the institute's system administrator, Marion Fiedler. For the last years I also shared the office with her, which made up one important part of the pleasant working atmosphere. Likewise, I would like to thank Sylvia Hofmann for her help over the years, typing manuscripts from my illegible handwriting.

I would like to thank Birgit Adolph for introducing me to the basics of the optical properties calculations at the beginning of my work. Moreover, I gladly mention helpful discussions with my colleagues at the IFTO, in particular with Jan-Martin Wagner who's help with L^AT_EX and related questions has proven invaluable.

At the *Laboratoire des Solides Irradiés* of the *École Polytechnique* in Paris, where I spent 6 months during my PhD work, I was warmly welcomed, and I received kind help and support from the whole Solid State Theory Group. In particular, I would like to thank Lucia Reining for providing excellent ideas and support, as well as personal motivation.

I am deeply obliged to Peter Gulden, Jan-Martin Wagner, and Grit Kunert for critically proof-reading the manuscript at very short notice.

Finally, I would like to cordially thank Grit Kunert for the lasting support over the years during which the work contained in this thesis has been done.

Palaiseau, 7th December 2004

Bibliography

- [1] O. Bisi, S. Ossicini, and L. Pavesi, *Surf. Sci. Rep.* **38**, 1 (2000).
- [2] S. Takeoka, M. Fujii, S. Hayashi, and K. Yamamoto *Phys. Rev. B* **58**, 7921 (1998).
- [3] J.P. Wilcoxon, P.P. Provencio, and G.A. Samara, *Phys. Rev. B* **64**, 035417 (2001).
- [4] K.A.Littau, P.J. Szajowski, A.J. Muller, A.R. Kortan, and L.E. Brus, *J. Phys. Chem.* **97** 1224 (1993).
- [5] Ch. Schubert, U. Kaiser, A. Hedler, W. Wesch, T. Gorelik, U. Glatzel, J. Kräusslich, B. Wunderlich, G. Hess, K. Goetz, *J. Appl. Phys.* **91**, 1520 (2002).
- [6] L. Kronik, R. Fromherz, E. Ko, G. Gantefo, J.R. Chelikowsky, *nature mat.* **1**, 1 (2002).
- [7] A. Fissel, K. Pfennighaus, and W. Richter, *Appl. Phys. Lett.* **71**, 2981 (1997).
- [8] A. Zunger, *phys. stat. sol. (b)* **224**, 727 (2001).
- [9] C. Delerue, M.Lannoo, and G. Allan, *phys.stat.sol.(b)* **227**, 115 (2001).
- [10] J. Tersoff, *Phys. Rev. B* **38**, 9902 (1988).
- [11] C. Noguez and S.E. Ulloa, *Phys. Rev. B* **56**, 9719 (1997).
- [12] A.A. Shvartsburg, B. Liu, Zhong-Yi Lu, Cai-Zhuang Wang, Martin F. Jarrold, and Kai-Ming Ho, *Phys. Rev. Lett.* **83**, 2167 (1999).
- [13] J Wang, G. Wang, and J. Zhao, *Phys. Rev. B* **64**, 205411 (2001).
- [14] I. Vasiliev, S. Ögüt and J.R. Chelikowsky, *Phys. Rev. Lett.* **86**, 1813 (2001).
- [15] E.W. Draeger, J. C. Grossman, A.J. Williamson, and G. Galli, *Phys. Rev. Lett.* **90**, 167402 (2003).
- [16] Y. Zhao, Y.-H. Kim, and S.B. Zhang, *Phys. Rev. Lett.* (submitted).
- [17] J.K. Bording and J. Taftø, *Phys. Rev. B* **62**, 8098 (2000).
- [18] L. Pavesi, L. Dal Negro, C. Mazzoleni, G. Franzo, and F. Priolo, *Nature* **408**, 440 (2000).
- [19] G. Onida, L. Reining, and A. Rubio, *Rev. Mod. Phys.* **74**, 601 (2002).
- [20] T. Aoki, S. Komodoori, S. Kobayashi, C. Fujihashi, A. Ganjoo, and K. Shimakawa, *J. Non-Cryst. Sol.* **299**, 642 (2002).
- [21] D.E. Aspnes and A.A. Studna, *Phys. Rev. B* **27**, 985 (1983).
- [22] S. Takeoka, M. Fujii, and S. Hayashi, *Phys. Rev. B* **62**, 16820 (2000).
- [23] L.-W. Wang and A. Zunger, *Phys. Rev. Lett.* **73**, 1039 (1994).
- [24] Nicola A. Hill and K.B. Whaley, *Phys. Rev. Lett.* **75**, 1130 (1995); **76**, 3039 (1996).
- [25] M. Lannoo, C. Delerue, and G. Allan, *Phys. Rev. Lett.* **74**, 3415 (1995); G. Allan, C. Delerue, M. Lannoo, and E. Martin, *Phys. Rev. B* **52**, 11982 (1995).
- [26] S. Ossicini, *phys. stat. sol. a* **170**, 377 (1998).

- [27] B. Delley and E.F. Steigmeier, Phys. Rev. B **47**, 1397 (1993); Appl. Phys. Lett. **67**, 2370 (1995).
- [28] S. Ögüt, J.R. Chelikowsky, and S. Louie, Phys. Rev. Lett. **79**, 1770 (1997).
- [29] C. Delerue, M. Lannoo, and G. Allan, Phys. Rev. Lett. **84**, 2457 (2000).
- [30] R.W. Godby and I.D. White, Phys. Rev. Lett. **80**, 3161 (1998) (Comment on Ögüt *et al.*, ref. [28]).
- [31] A. Franceschetti, L.W. Wang, and A. Zunger, Phys. Rev. Lett. **83**, 1269 (1999) (Comment on Ögüt *et al.*, ref. [28]).
- [32] M. Rohlfing and S. G. Louie, Phys. Rev. Lett. **80**, 3320 (1998).
- [33] R.J. Baierle, M.J. Caldas, E. Molinari, and S. Ossicini, Solid State Comm. **102**, 545 (1997).
- [34] M. Palummo, G. Onida, and R. Del Sole, Phys. Stat. Sol. A **175**, 23 (1999).
- [35] N. Koshida, H. Koyama, Y. Suda, Y. Yamamoto, M. Araki, T. Saito, K. Sato, N. Sata, and S. Shin, Appl. Phys. Lett. **63**, 2774 (1993).
- [36] C.E. Bottani, C. Mantini, P. Milani, M. Manfredini, A. Stella, P. Tognini, P. Cheyssac, and R. Kofman, Appl. Phys. Lett. **69**, 2409 (1996).
- [37] P. Tognini, L.C. Andreani, M. Geddo, A. Stella, P. Cheyssac, R. Kofman, and A. Migliori, Phys. Rev. B **53**, 6992 (1996).
- [38] P. Tognini, A. Stella, S.D. Silvestri, M. Nisoli, S. Stagira, P. Cheyssac, and R. Kofman, Appl. Phys. Lett. **75**, 208 (1999).
- [39] F.A. Reboredo, A. Franceschetti, and A. Zunger, Phys. Rev. B **61**, 13073 (2000).
- [40] A.B. Filonov, A.N. Kholod, V.E. Borisenko, A.L. Pushkarchuk, V.M. Zelenkovskii, F. Bassani, and F. Arnaud d'Avitaya, Phys. Rev. B **57**, 1394 (1998).
- [41] M. Luppi and S. Ossicini, J. Appl. Phys. **94** 2130 (2003).
- [42] M. Luppi and S. Ossicini, Phys. Stat. Sol. A **197** 251 (2003).
- [43] A. B. Filonov, S. Ossicini, F. Bassani, and F.A. d'Avitaya, Phys. Rev. B **65**, 195317 (2002).
- [44] F.A. Reboredo and A. Zunger, Phys. Rev. B **63**, 235314 (2001).
- [45] A. Puzder, A.J. Williamson, J.C. Grossman, and G. Galli, Phys. Rev. Lett. **88**, 097401 (2002).
- [46] M.V. Wolkin, J. Jorne, P.M. Fauchet, G. Allan, and C. Delerue, Phys. Rev. Lett. **82**, 197 (1999).
- [47] A.D. Yoffe, Adv. Phys., **50**, 1 (2001).
- [48] H.-Ch. Weissker, J. Furthmüller, and F. Bechstedt, Phys. Rev. B **67**, 165322 (2003).
- [49] J. Furthmüller, G. Cappellini, H.-Ch. Weissker, F. Bechstedt, Phys. Rev. B **66**, 045110 (2002).

- [50] G. Cappellini, H.-Ch. Weissker, D. De Salvator, J. Furthmüller, F. Bechstedt, G. Satta, F. Casula, L. Colombo, *J. Phys. C*, submitted.
- [51] M. Born and R. Oppenheimer, *Ann. d. Physik* **84**, 457 (1927).
- [52] M. Born and K. Huang, *Dynamical Theory of Crystal Lattices* (Oxford University Press; Oxford, 1954), Appendix VIII.
- [53] R.M. Dreizler, E.K.U. Gross, *Density Functional Theory*, Springer, Berlin-Heidelberg (1990).
- [54] H. Eschrig, *The Fundamentals of Density Functional Theory*, Teubner Verlagsgesellschaft, Leipzig (1996).
- [55] U. von Barth and L. Hedin, *J. Phys. C* **5**, 1629 (1972).
- [56] J.P. Perdew and A. Zunger, *Phys. Rev. B* **23**, 5048 (1981).
- [57] D.M. Ceperley and B.J. Alder, *Phys. Rev. Lett.* **45**, 566 (1980).
- [58] H. Hellmann, *Einführung in die Quantenchemie* (Deuticke, Leipzig 1937).
- [59] R.P. Feynman, *Phys. Rev.* **56**, 340 (1939).
- [60] F. Bechstedt, *Dichtefunktionaltheorie und ihre Anwendungen in der Festkörpertheorie*. Lecture notes, Friedrich-Schiller-Universität Jena (1997).
- [61] Documentation of the VASP package: <http://cms.mpi.univie.ac.at/vasp/vasp/vasp.html>
- [62] R. Car and M. Parrinello, *Phys. Rev. Lett.* **55**, 2471 (1985).
- [63] L.D. Landau, *Sov. Phys. JETP* **3**, 920 (1957), *Sov. Phys. JETP* **5**, 101 (1957); *Sov. Phys. JETP* **35**, 70(1959).
- [64] R.D. Mattuck, *A Guide to Feynman Diagrams in the Many-Body Problem*, McGraw-Hill, New York (1976).
- [65] R.W. Godby, M. Schlüter, and L.J. Sham, *Phys. Rev. B* **37**, 10159 (1988).
- [66] L.J. Sham, *Phys. Rev.* **150**, 720 (1966).
- [67] L.J. Sham and M. Schlüter, *Phys. Rev. B* **32**, 3883 (1985).
- [68] L.J. Sham and M. Schlüter, *Phys. Rev. Lett.* **51**, 1888 (1983).
- [69] J.P. Perdew and M. Levy, *Phys. Rev. Lett.* **51**, 1884 (1983).
- [70] L. Hedin and S. Lundqvist, in *Solid State Physics*, edited by H. Ehrenreich, F. Seitz, and D. Turnbull (Academic, New York, 1969), Vol. 23, p. 1.
- [71] A. Görling, *Phys. Rev. A* **54**, 3912 (1996); *Phys. Rev. Lett.* **85**, 4229 (2000).
- [72] L. Hedin, *J. Phys. Cond. Mat.* **11** R489 (1999).
- [73] F. Bechstedt and R. Del Sole, *Phys. Rev. B* **38**, 7710 (1988).
- [74] O. Pulci, F. Bechstedt, G. Onida, R. Del Sole, and L. Reining, *Phys. Rev. B* **60**, 16758 (1999).

- [75] H.-Ch. Weissker, J. Furthmüller, and F. Bechstedt, Phys. Rev. B **69**, 115310 (2004).
- [76] G. Onida, L. Reining, R.W. Godby, R. Del Sole, and W. Andreoni, Phys. Rev. Lett. **75**, 818 (1995).
- [77] N.F. Mott, *Metal-Insulator Transitions*, (Barnes and Noble, New York, 1974).
- [78] S. Ögüt, J.R. Chelikowsky, and S. Louie, Phys. Rev. Lett. **80**, 3162 (1998) (Reply to Franceschetti, Wang, and Zunger, ref. [31].)
- [79] S. Ögüt, J.R. Chelikowsky, and S. Louie, Phys. Rev. Lett. **83**, 1270 (1999). (Reply to Godby and White, ref. [30]).
- [80] U. Itoh *et al.*, J.Chem.Phys. **85**, 4867 (1986).
- [81] B.P. Pullen, T.A. Carlson, W.E. Moddeman, G.K. Schweiz, W.E. Bull, F.A. Grimm, J. Chem. Phys. **53**, 768 (1970).
- [82] L. Ramos, private communication.
- [83] P. Rinke, private communication.
- [84] K. Tonokura, T. Murasaki, and M. Koshi, J. Phys. Chem **106**, 555 (2002).
- [85] S. Ögüt, R. Burdick, Y. Saad, and J. R. Chelikowsky, Phys. Rev. Lett. **90**, 127401 (2003).
- [86] M. Preuss, W.G. Schmidt, K. Seino, J. Furthmüller, and F. Bechstedt, J. Comp. Chem., **25**, 112 (2003).
- [87] R.O. Jones and O. Gunnarsson, Rev. Mod. Phys. **61**, 689 (1989).
- [88] L. Hedin and A. Johansson, J. Phys. B, **2**, 1336 (1969).
- [89] J.P. Perdew and M. Levy, Phys. Rev. B **31**, 6264 (1985).
- [90] S. Albrecht, L. Reining, R. Del Sole, and G. Onida, Phys. Rev. Lett. **80**, 4510 (1998).
- [91] J. M. Luttinger and W. Kohn, Phys. Rev. **97**, 869 (1955).
- [92] G. Bastard, *wave mechanics applied to semiconductor heterostructures*, les éditions de physique, Les Ulis Cedex, 1992.
- [93] H. Fu, L.W. Wang, and A. Zunger, Phys. Rev. B **57**, 9971 (1998).
- [94] L.W. Wang, A.J. Williamson, A. Zunger, H. Jiang, and J. Singh, Appl. Phys. Lett. **76**, 339 (2000).
- [95] M.L. Cohen and T.K. Bergstresser, Phys. Rev. **141**, 789 (1966).
- [96] A.J. Williamson, A. Franceschetti, and A. Zunger, Europhys. Lett. **53**, 59 (2001).
- [97] F.A. Reboredo, A. Franceschetti, and A. Zunger, Phys. Rev. B **75**, 2972 (1999).
- [98] H.-Ch. Weissker, J. Furthmüller, and F. Bechstedt, Mat. Sci. Eng. B **101**, 39 (2003).
- [99] F.A. Reboredo and A. Zunger, Phys. Rev. B **62**, R2275 (2000).
- [100] K. Leung and K.B. Whaley, Phys. Rev. B **56**, 7455 (1997).

- [101] E. Runge, and E.K.U. Gross, Phys. Rev. Lett. **52**, 997 (1984).
- [102] E.K.U. Gross and W. Kohn, Phys. Rev. Lett. **55**, 2850 (1985).
- [103] I. Vasiliev, S. Ögüt, and J. R. Chelikowsky, Phys. Rev. Lett. **82**, 1919 (1999).
- [104] V.I. Gavrilenko, and F. Bechstedt, Phys. Rev. B **54**, 13416 (1996).
- [105] F. Jensen, *Introduction to Computational Chemistry*, (Wiley, Chichester, England), Chap. 4.
- [106] W.M.C. Foulkes, L. Mitas, R.J. Needs, and G. Rajagopal, Rev. Mod. Phys. **73**, 33 (2001).
- [107] A.J. Williamson, J.C. Grossman, R.Q. Hood, A. Puzder, and Giulia Galli, Phys. Rev. Lett. **89**, 196803 (2002).
- [108] P.D.J. Calcott, K.J. Nash, L.T. Canham, M.J. Kane, D. Brumhead, J. Phys. Cond. Mat. **5**, L91 (1993).
- [109] M.L. Brongersma, P.G. Kik, A. Polman, K.S. Min, and H. Atwater, Appl. Phys. Lett. **76**, 351 (2000).
- [110] A.Y. Kobitski, K.S. Zhuravlev, H.P. Wagner, and D.R.T Zahn, Phys. Rev. B **63**, 115423 (2001).
- [111] A. Zywietz, J. Furthmüller, and F. Bechstedt, Phys. Rev. B **62**, 6854 (2000).
- [112] U. von Barth, Phys. Rev. A **20**, 1693 (1979).
- [113] M. Gurioli, A. Vinattieri, J. Martinez-Pastor, and M. Colocci, Phys. Rev. B **50**, 11817 (1994).
- [114] A. Patane, A. Levin, A. Polimeni, L. Eaves, P. C. Main, M. Henini, and G. Hill, Phys. Rev. B **62**, 11084 (2000).
- [115] A. Franceschetti and S.T. Pantelides, Phys. Rev. B **68**, 033313 (2003).
- [116] Y. Kanemitsu and S. Okamoto, Phys. Rev. B **58**, 9652 (1998).
- [117] H. Ehrenreich und M.H. Cohen, Phys. Rev. **115**, 786 (1959).
- [118] V. Ambegaokar und W. Kohn, Phys. Rev. **117**, 423 (1960).
- [119] R. Del Sole und E. Fiorino, Phys. Rev. B **29**, 4631 (1984).
- [120] B. Adolph, *Zur ab-initio-Beschreibung der optischen Eigenschaften von Halbleitern, insbesondere von SiC-Polytypen*, PhD thesis (Dissertation), Friedrich-Schiller-Universität Jena, (1998).
- [121] R. Del Sole and R. Girlanda, Phys. Rev. B **48**, 11789 (1993).
- [122] D. Pines, *Elementary Excitations in Solids* (Addison-Wesley, New York, 1963).
- [123] A.L. Fetter and J.D. Walecka, *Quantum Theory of Many-Particle Systems* (McGraw-Hill, New York, 1971).
- [124] D.L. Dexter, Solid State Phys. **6**, 360 (1958).

- [125] C. Delerue, G. Allan, and M. Lannoo, *Phys. Rev. B* **48**, 11024 (1993).
- [126] W. Brauer and H.-W. Streitwolf, *Theoretische Grundlagen der Halbleiterphysik*, Akademie-Verlag Berlin (1973).
- [127] W.E. Pickett, *Comput. Phys. Rep* **9**, 115 (1989).
- [128] U. von Barth and C.D. Gelatt, *Phys. Rev. B* **21**, 2222 (1980).
- [129] H.-Ch. Weissker unpublished.
- [130] J.C. Phillips and L. Kleinman, *Phys. Rev.* **116**, 287 (1959).
- [131] G.B. Bachelet, D.R. Hamann, M. Schlüter, *Phys. Rev. B* **26**, 4199 (1982).
- [132] D.R. Hamann, *Phys. Rev. B* **40**, 2980 (1989).
- [133] N. Toullier and J.L. Martins, *Phys. Rev. B* **43**, 1993 (1991).
- [134] D. Vanderbilt, *Phys. Rev. B* **41**, 7892 (1990).
- [135] J. Furthmüller, P. Käckell, F. Bechstedt, and G. Kresse, *Phys. Rev. B* **61**, 4576 (2000).
- [136] M. Fuchs, M. Scheffler, *Computer Physics Communications* **119**, 67 (1999).
- [137] L. Kleinman and D.M. Bylander, *Phys. Rev. Lett.* **48**, 1425 (1982).
- [138] P. Monachesi, A. Marini, G. Onida, M. Palumbo, and R. Del Sole, *phys. stat. sol. (a)* **184**, 101 (2001).
- [139] B. Adolph, J. Furthmüller, and F. Bechstedt, *Phys. Rev. B* **63**, 125108 (2001).
- [140] P. Blöchl, *Phys. Rev. B* **50**, 17953 (1994).
- [141] G. Kresse and D. Joubert, *Phys. Rev. B* **59**, 1758 (1999).
- [142] H. Kageshima and K. Shiraishi, *Phys. Rev. B* **56**, 14986 (1997).
- [143] H.-Ch. Weissker, J. Furthmüller, and F. Bechstedt, *Phys. Rev. B* **65**, 155327 (2002).
- [144] H.-Ch. Weissker, J. Furthmüller, and F. Bechstedt, *Phys. Rev. B* **65**, 155328 (2002).
- [145] U. Kaiser, private communication.
- [146] G. Kresse and J. Furthmüller, *Comput. Mater.Sci.* **6**, 15 (1996); *Phys. Rev. B* **54**, 11169 (1996).
- [147] J.P. Perdew and A. Zunger, *Phys. Rev. B* **23**, 5048 (1981).
- [148] S.G. Louie, S. Froyen, and M.L. Cohen, *Phys. Rev. B* **26**, 1738 (1982).
- [149] <http://www.abinit.org/>
- [150] M.P. Teter, M.C. Payne and D.C. Allan, *Phys. Rev. B* **40**, 12255 (1989).
- [151] D.M. Bylander, L. Kleinman and S. Lee, *Phys Rev. B* **42**, 1394 (1990).
- [152] see: D. M. Wood and A. Zunger, *J. Phys. A* **18**, 1343 (1985).
- [153] P. Pulay, *Chem. Phys. Lett.* **73**, 393 (1980).
- [154] D.D. Johnson, *Phys. Rev. B* **38**, 12 087 (1988).

- [155] S. Blügel, PhD Thesis, RWTH Aachen (1988).
- [156] A. Baldereschi, Phys. Rev. B **7**, 5212 (1973).
- [157] H.J. Monkhorst and J.B. Pack, Phys. Rev. B **13**, 5188 (1976).
- [158] D.J. Chadi and M.L. Cohen, Phys. Rev. B **8**, 5747 (1973).
- [159] G. Gilat and L.J. Raubenheimer, Phys. Rev. **144**, 390 (1966).
- [160] G. Lehmann and M. Taut, Phys. Stat. Sol. B **54**, 469 (1972).
- [161] D. J. Moss, J.E. Sipe, and H.M. van Driel, Phys. Rev. B **36**, 1153 (1987).
- [162] B. Adolph, V. I. Gavrilenko, K. Tenelsen, F. Bechstedt, and R. Del Sole, Phys. Rev. B **53**, 9797 (1996).
- [163] O. Pulci, G. Onida, A.I. Shkrebtii, and R. Del Sole, Phys. Rev. B **55**, 6685 (1997).
- [164] J.E. Müller and J.W. Wilkins, Phys. Rev. B **29**, 4331 (1984).
- [165] H. Bross, phys. stat. sol. (b) **179**, 429 (1993).
- [166] M. Taut, Phys. Rev. B **57**, 2217 (1998).
- [167] C.S. Wang and J. Callaway, Phys. Rev. B **9**, 4897 (1974).
- [168] G. Gilat, Phys. Rev. B **7**, 891 (1973).
- [169] P.E. Blöchl, O. Jepsen, and O.K. Andersen, Phys. Rev. B **49**, 16223 (1994).
- [170] O. Pulci, B. Adolph, U. Grossner, and F. Bechstedt, Phys. Rev. B **58**, 4721 (1998).
- [171] D.M. Newns and P.C. Pattnaik, Phys. Rev. B **54**, 16313 (1996).
- [172] J. Rath and A.J. Freeman Phys. Rev. B **11**, 2109 (1975).
- [173] G. Gilat and N.R. Bharatiya, Phys. Rev. B **12**, 3479 (1975).
- [174] M.H. Boon, M.S. Methfessel, and F.M. Müller, J. Phys. C **19**, 5337 (1986).
- [175] G.L. Bir, G.E. Pikus, *Symmetry and Strain-induced Effects in Semiconductors*, John Wiley & Sons, Jerusalem 1974; russ. Original: Moskau 1972.
- [176] C.J. Pickard and M.C. Payne, Phys. Rev. B **59**, 4685 (1999).
- [177] C.J. Pickard and M.C. Payne, Phys. Rev. B **62**, 4383 (2000).
- [178] H.-Ch. Weissker, J. Furthmüller, F. Bechstedt, Phys. Rev. B **64**, 035105 (2001).
- [179] L. Kleinman, Phys. Rev. B **28**, 1139 (1983).
- [180] O. Jepsen and O.K. Andersen, Phys. Rev. B **29**, 5965 (1984).
- [181] M. Hanke, W. Kühn, R. Strehlow, phys. stat. sol. (b) **123** K39 (1984).
- [182] J. Hama, M. Wanatabe, and T. Kato, J. Phys.: Cond. Mat. **2**, 7445 (1990).
- [183] S.Y. Ren and W.A. Harrison, Phys. Rev. B **23**, 762 (1981).
- [184] J.P. Loehr, Phys. Rev. B **52**, 2374 (1995).

- [185] *Semiconductors: group-IV elements and III-V compounds*, O. Madelung (ed.), Springer (1991).
- [186] J. Petalas, S. Logothetidis, M. Gioti, and C. Janowitz, *phys. stat. sol. (b)* **209**, 499 (1998).
- [187] D. Buttard, G. Dolino, C. Faivre, A. Halimaoui, F. Comin, V. Formoso, and L. Ortega, *J. Appl. Phys.* **85**, 7105 (1999).
- [188] A. Cheung, G. de M. Azevedo, C.J. Glover, D.J. Llewellyn, R.G. Elliman, G.J. Foran, and M.C. Ridgeway, *Appl. Phys. Lett.* **84**, 278 (2004).
- [189] L. Pizzagalli, G. Galli, J.E. Klepeis, and F. Gygi, *Phys. Rev. B* **63**, 165324 (2001).
- [190] Y.H. Ogata, N. Yoshimi, R. Yasuda, T. Tsuboi, T. Sakka, and A. Otsuki, *J. Appl. Phys.* **90**, 6487 (2001).
- [191] L. Reining, O. Pulci, M. Palumbo, G. Onida, *Int.J. Quantum Chem.* **77**, 951 (2000).
- [192] H. Hofmeister, F. Huiken, B. Kohn, *Eur. Phys. J. D* **9**, 137 (1999).
- [193] W. Mönch, *Semiconductor surfaces and interfaces*, 2nd ed. (Springer, Berlin 1995).
- [194] E. Kaxiras and J.D. Joannopoulos, *Phys. Rev. B* **37**, 8842 (1987).
- [195] E. Wimmer, A.J. Freeman, in: *Handbook of Surface Science*, Vol. 2, *Electronic Structure*, ed. by K. Horn and M. Scheffler (Elsevier, Amsterdam 2000), p.1.
- [196] H.-Ch. Weissker, J. Furthmüller, and F. Bechstedt, *Phys. Rev. Lett* **90**, 085501 (2003).
- [197] S. Furukawa, T. Miyasato, *Phys. Rev. B* **38**, 5726 (1988).
- [198] T. van Buuren, L. N. Dinh, L. L. Chase, W. J. Siekhaus, and L. J. Terminello, *Phys. Rev. Lett.* **80**, 3803 (1998).
- [199] Y.M. Niquet, C. Delerue, G. Allan, and M. Lannoo, *Phys. Rev. B* **62**, 5109 (2000).
- [200] E. Degoli, G. Cantele, E. Luppi, R. Magri, D. Ninno, O. Bisi, and S. Ossicini, *Phys. Rev. B* **69**, 155411 (2004).
- [201] Y. Maeda, *Phys. Rev. B* **51**, 1658 (1995).
- [202] A. Puzder, private communication.
- [203] D.V. Melnikov and J.R. Chelikowsky, *Phys. Rev. Lett.* **92**, 046802 (2004).
- [204] Y.M. Niquet, G. Allan, C. Delerue, and M. Lannoo, *App. Phys. Lett.* **77**, 1182 (2000).
- [205] T. Matsumoto, J. Suzuki, M. Ohnuma, Y. Kanemitsu, and Y. Masumoto, *Phys. Rev. B* **63**, 195322 (2001).
- [206] G. Ledoux, J. Gong, F. Huisken, O. Guillois, and C. Reynaud, *Appl. Phys. Lett.* **80**, 4834 (2002).
- [207] J. Heitmann, F. Müller, L. Yi, and M. Zacharias, to be published.
- [208] D. Kovalev, H. Heckler, G. Polisski, and F. Koch, *phys. stat. sol. (b)* **215**, 871 (1999).

- [209] A.N. Kholod, S. Ossicini, V.E. Borisenko, and F. Arnaud d'Avitaya, *Phys. Rev. B* **65**, 115315 (2002).
- [210] A.N. Kholod, A. Saúl, J.D. Fuhr, V.E. Borisenko, and F.A. d'Avitaya, *Phys. Rev. B* **62**, 12949 (2000).
- [211] E.E. Lippens and M. Lannoo, *Phys. Rev.* **B39**, 10935 (1989).
- [212] T. Takagahara and K. Takeda, *Phys. Rev.* **B46**, 15578 (1992).
- [213] J.P. Wilcoxon, G.A. Samara, P.N. Provencio, *Phys. Rev. B* **60**, 2704 (1999).
- [214] W.L. Wilson, P.J. Szajowski, and L.E. Brus, *Science* **262**, 1242 (1993).
- [215] Y. Kanemitsu, Y. Fukunishi, and T. Kushida, *Appl. Phys. Lett.* **77**, 211 (2000).
- [216] J. Heitmann, M. Schmidt, L. Yi, R. Scholz, and M. Zacharias, *Proc. ICPS, Edinburgh 2002*.
- [217] S. Takeoka, M. Fujii, S. Hayashi, and K. Yamamoto, *Appl. Phys. Lett.* **58**, 1558 (1999).
- [218] P.Y. Yu and M. Cardona, *Fundamentals of Semiconductors* (Springer, Berlin 1995).
- [219] C.S. Wang and B.M. Klein, *Phys. Rev.* **B24**, 3417 (1981).
- [220] A. Stella, P. Tognini, P. Cheyssac, R. Kofman, M. Palumbo, G. Onida, and R. Del Sole, *Proc. 25th Internat. Conf. Phys. Semiconductors, Osaka 2000*, Eds. N. Miura and T. Ando (Springer, Berlin 2001), p. 1283.
- [221] D.V. Melnikov, J.R. Chelikowsky, *Solid state comm.* **127** 361 (2003).
- [222] Y.S. Tang, S. Cai, G. Jin, J. Duan, K.L. Wang, H.M. Soyes, and B.S. Dunn, *Appl. Phys. Lett.* **71**, 2448 (1997).
- [223] A.-B. Chen and A. Sher, *Semiconductor Alloys* (Plenum Press, New York 1995).
- [224] M.C. Ridgway, K.M. Yu, C.J. Glover, G.J. Foran, C. Clerc, J.L. Hansen, and A.N. Larsen, *Phys. Rev.* **B60**, 10831 (1999).
- [225] W.A. Harrison, *Electronic Structure and the Properties of Solids* (Dover Publ., New York 1989).
- [226] M. Luppi, S. Ossicini, *Mat. Sci. Eng. B* **101**, 34 (2003).
- [227] N. Daldosso, M. Luppi, S. Ossicini, E. Degoli, R. Magri, G. Dalba, P. Fornasini, R. Grisenti, F. Rocca, L. Pavesi, S. Boninelli, F. Priolo, C. Spinella, and F. Iacona, *Phys. Rev. B* **68**, 085327 (2003).
- [228] K.L. Teo, S.H. Kwok, P.Y. Yu, and S. Guha, *Phys. Rev. B* **62**, 1584 (2000).
- [229] C.S. Johnson and L.G. Pedersen, *Problems and Solutions in Quantum Chemistry and Physics* (Dover, New York, 1986), p. 122.
- [230] C. Raffy, J. Furthmüller, and F. Bechstedt, *Phys. Rev. B* **66**, 075201 (2002).
- [231] F. Reboredo, private communication.

- [232] H.M. Cheong, W. Paul, S.P. Withrow, J.G. Zhu, J.D. Budai, C.W. White, and D.M. Hembree, Jr., *Appl. Phys. Lett.* **68**, 87 (1996).
- [233] A. Puzder, A.J. Williamson, J.C. Grossman, and G. Galli, *J. Am. Chem. Soc.* **125**, 2786 (2003).
- [234] K. Shiba, K. Nakagawa, M. Ikeda, A. Kohno, S. Miyazaki and M. Hirose, *Jpn. J. Appl. Phys.* **36**, L1279 (1997).
- [235] M. Fujii, A. Mimura, S. Hayashi, Y. Yamamoto, and K. Murakami, *Phys. Rev. Lett.* **89**, 206805 (2002).

Deutsche Zusammenfassung

Die vorliegende Arbeit betrachtet die intrinsischen optischen Eigenschaften von Germanium- und Siliziumkristalliten im Rahmen der Dichtefunktionaltheorie (DFT) in Lokaldichtenäherung. Ihre Ergebnisse liefern Beiträge sowohl zum grundlegenden physikalischen Verständnis der Effekte in Nanokristalliten (NCs) als auch zu praktischen Aspekten.

Zu Beginn der Arbeit lag eine Vielzahl von unterschiedlichen theoretischen Arbeiten vor, die insbesondere für den mittleren Größenbereich der Kristallite zumeist semiempirischer Natur waren. Deren Anwendbarkeit auf die Kristallite im nm-Bereich ist jedoch nicht *a priori* gesichert. Außerdem machen eine Vielzahl von Effekten aufgrund ihrer Natur *ab-initio*-Berechnungen nötig. Als Beispiel seien die strukturellen Beiträge zur Stokes-Verschiebung von Emissionslinien gegenüber der Absorption genannt.

Der Stand der Literatur bezüglich der experimentellen Charakterisierung ist relativ unüberschaubar. Das liegt darin begründet, daß die verschiedenen Herstellungsmethoden für Nanokristalle sehr unterschiedliche Strukturen mit folglich ebenfalls sehr unterschiedlichen Eigenschaften hervorbringen. Aus diesem Grund liegt für einen großen Teil der Ergebnisse noch keine eindeutige und gesicherte Interpretation vor. Damit wird ein enges Zusammenspiel von Theorie bzw. Modellierung und Experiment notwendig. Im Fall der vorliegenden Arbeit war es notwendig, experimentelle Resultate zu finden, die möglichst eindeutig auf die räumlichen Quantisierungseffekte zurückzuführen sind und nicht durch Defekte oder oberflächenchemische Effekte beeinflusst sind.

In der vorliegenden Arbeit wurden Modellstrukturen benutzt, die Fragmenten der Volumenhalbleiter Silizium und Germanium mit Wasserstoffabsättigung der äußeren Bindungen entsprechen. Das Hauptaugenmerk lag dabei auf den allgemeinen Tendenzen und Effekten. Insbesondere waren wir in der Lage, das Zusammenspiel bzw. die gegenseitige Unabhängigkeit der Effekte des räumlichen *Confinement* und von Mischungseffekten und Druckabhängigkeiten zu beschreiben. Die Rechnungen wurden mit Hilfe des Programmpaketes VASP durchgeführt, das eine Ebene-Wellen-Entwicklung der Kohn-Sham-Eigenfunktionen benutzt. Die Modellstrukturen wurden deswegen im Rahmen der Superzellenmethode beschrieben. Um die für diese Strukturen notwendigen großen Zellen behandeln zu können, kam die *Projector-augmented-wave*- (PAW-) Methode zum Einsatz. Neben den geringen Anschneideenergien, die ähnliche Werte wie jene für die „ultra-soften“ Pseudopotentiale besitzen, werden bei dieser Methode Allelektronenwellenfunktionen erzeugt. Damit kann die Berechnung der Übergangsmatrixelemente erfolgen, die für die Berechnung der optischen Eigenschaften notwendig sind.

Die ionische Relaxation und die Bestimmung der elektronischen und optischen Eigenschaften für sowohl die ideale als auch die relaxierte Struktur von freien Nanokristallen haben gezeigt, daß die Relaxation für die Modellierung unabdingbar ist. Insbesondere die strahlenden Lebensdauern sind aufgrund der energetischen Umordnung der Zustände nahe des obersten besetzten und des untersten unbesetzten Zustandes sehr empfindlich.

Weiter ergab die ionische Relaxation ein komplexes strukturelles Muster. Die interatomaren Abstände an der Oberfläche der Kristallite sind geringer als jene im entsprechenden Volumenmaterial, während im Zentrum eine Expansion stattfindet. Die durchschnittlichen Bindungslängen sind geringer als im Volumenmaterial.

Ein zentraler Punkt der Arbeit bestand in der Berechnung der Anregungsenergien von Nanokristallen. Wir haben eine sogenannte Δ -self-consistent-field-Methode (Δ SCF) benutzt, um die gesuchten Anregungsenergien aus den Gesamtenergien zweier selbstkonsistenter Rechnungen zu bestimmen. Anders als bei der bisher gebräuchlichen Δ SCF-Methode, die Paar Anregungsenergien aus den Einteilchenanregungen zu berechnen sucht, konnten wir mit Hilfe von Besetzungszahlvorgaben eine gleichzeitige Beschreibung von Elektron und Loch im Nanokristalliten vornehmen. Damit wird eine Elektron-Loch-Anregung modelliert, wobei sowohl die Coulomb- als auch Selbstenergieeffekte eingeschlossen sind. Diese Methode, welche eine Reihe von Vorteilen gegenüber der „konventionellen“ Δ SCF-Methode besitzt, ergibt für kleinere Kristallite Werte, die den Resultaten der zeitabhängigen Dichtefunktionaltheorie gleichen. Die Streuung der zum Vergleich verfügbaren experimentellen und theoretischen Resultate ist groß. Deswegen kann eine abschließende Bewertung der einzelnen Methoden noch nicht erfolgen. Es stellt sich jedoch heraus, daß eine einfache funktionelle Abhängigkeit der Anregungsenergien vom Kristallitdurchmesser nicht angegeben werden kann. Die verschiedenen angepaßten Funktionen mit $1/d^a$ -Abhängigkeiten ergeben jedoch grob Werte zwischen 1.0 und 1.4 für den Exponenten.

Die Auslöschung der Selbstenergieeffekte und der Elektron-Loch-Wechselwirkung in unseren Resultaten ist fast vollständig. Aus diesem Grunde sind für die betrachteten Systeme die Energiedifferenzen von Kohn-Sham-Eigenwerten in DFT-LDA gute Näherungen der Anregungsenergien. Die Methode ordnet sich erfolgreich in die komplexeren Methoden ein, wie etwa der Kombination von GW-Rechnung und der Lösung der Bethe-Salpeter-Gleichung. Sie ermöglicht eine zuverlässige Bestimmung von Anregungsenergien insbesondere kleiner Kristallite. Das Verfahren wird inzwischen von einer Vielzahl von Forschungsgruppen angewandt.

Desweiteren wurde – erstmalig im Rahmen einer *ab-initio*-Methode – die Aufspaltung der Anregungsenergien von Singulett- und Tripletexziton aufgrund des Elektron-Loch-Austauschs berechnet. Dazu wurden spinpolarisierte Rechnungen im Rahmen der lokalen Spindichtenäherung (LSDA) durchgeführt. Trotz prinzipieller Probleme der LSDA bei der Beschreibung von Multipletts wurden Werte in guter Übereinstimmung mit dem Experiment erzeugt.

Ein unter dem Gesichtspunkt der Anwendung sehr wichtiges Resultat ist das Auftreten von starken optischen Übergängen an der Absorptionskante von Ge NCs. Das reflektiert die starken Beiträge der direkten (Γ - Γ) Bandlücke. Diese Interpretation der Resultate wurde durch Untersuchungen verschiedener Druckabhängigkeiten bestätigt. Anders als in Si NCs, die bis hinab zu sehr kleinen Durchmessern den indirekten Charakter des Volumenmaterials widerspiegeln, ist man in Germaniumkristalliten nicht auf phononen- oder defektunterstützte Übergänge angewiesen, um Lumineszenz zu erzielen. Lebensdauermessungen an Siliziumkristalliten können trotz der starken Streuung der experimentellen Werte als Bestätigung unserer Ergebnisse angesehen werden.

Neben der Charakterisierung der Kristallite durch Anregungsenergien und Lebensdauern ist auch der Gesamtverlauf der dielektrischen Funktion von Interesse. In der vorliegenden Arbeit wurden die Spektren in der Näherung unabhängiger Teilchen und unter Vernachlässigung von Lokalfeldeffekten berechnet. Damit wurde eine in wesentlichen gute Übereinstimmung mit experimentellen Spektren erzielt.

Im Rahmen dieser Arbeit wurden erstmals *ab-initio*-Berechnungen der Eigenschaften von Mischkristalliten im nm-Bereich durchgeführt. Die Bindungslängen der betrachteten $\text{Ge}_x\text{Si}_{1-x}$ -Kristallite stellen sich, ähnlich wie im Volumenmaterial, im wesentlichen so ein, daß die Vegardsche Regel erfüllt wird. Anregungsenergien und Lebensdauern ändern sich kontinuierlich mit der Zusammensetzung x . Damit konnten die Meßergebnisse für Photolumineszenz von $\text{Ge}_x\text{Si}_{1-x}$ Kristalliten durch intrinsische Effekte erklärt und Defekte als Hauptmechanismus der Bandlückenänderung ausgeschlossen werden. Die Ähnlichkeit der x -Abhängigkeit mit der des Volumenmaterials sowie die Skalierbarkeit von Anregungsenergien und Lebensdauern beim Vergleich mit experimentellen Werten zeugen von einer weitgehenden Unabhängigkeit der Effekte von *Confinement* und Mischung. Diese Vermutung wurde durch die Berechnung der zusammensetzungsabhängigen Druckabhängigkeit der Anregungsenergien bestätigt.

Um eine bessere Modellierung der Einbettung zu erzeugen, wurden Kristallite in einer kristallinen Matrix betrachtet. Am Modellsystem Ge oder Si in Siliziumkarbid haben wir die ersten *ab-initio*-Berechnungen der elektronischen und optischen Eigenschaften solcher Systeme durchgeführt. Zur Erzeugung der Modellstruktur wurden Silizium- und Kohlenstoffatome der Matrix durch Si oder Ge ersetzt, so daß aufgrund der Gitterfehlانpassung eine stark verspannte Struktur vorlag. Die einzige weitere *ab-initio*-Untersuchung eingebetteter Kristallite von Luppi *et al.*, arbeitet mit einem Modell, das ähnliche Beschränkungen wegen der Verspannung aufweist.

Eines der Hauptprobleme der vorliegenden Arbeit war die Brillouinonenintegration, welche insbesondere für die Berechnung der dielektrischen Funktion notwendig ist. Die konventionelle Tetraederintegrationsmethode, die in Volumenmaterialien sehr erfolgreich eingesetzt wird und die Anzahl der notwendigen \mathbf{k} -Punkte stark reduziert, versagt im Falle der Superzellmethode mit großen Zellen. Der Grund hierfür liegt in der Faltung der Bänder, nach der an jedem \mathbf{k} -Punkt sehr viele Bänder pro Energieintervall vorliegen. Da die *ab-initio*-Rechnungen keine Zuordnung der verschiedenen Energien zu Bändern zuläßt, ist eine Interpolation in einer Vielzahl von Fällen praktisch nicht möglich.

Um eine Beschreibung der Bandstruktur zu gewinnen, die eine Zuordnung von Energien zu Bändern ermöglicht, wurde eine auf $\mathbf{k}\cdot\mathbf{p}$ -Störungstheorie beruhende Extrapolation implementiert, die ausgehend von einem \mathbf{k} -Punkt innerhalb der irreduziblen Brillouinzone (IBZ) dieselbe überdeckt. Um die lineare Tetraedermethode anwenden zu können, wurde die IBZ in ein feineres Tetraedernetz unterteilt. In jedem dieser Tetraeder wurde eine Linearisierung der Bandenergien vorgenommen. Damit ist der Einsatz der linearen Tetraedermethode möglich. Zwei Korrekturen wurden einbezogen: Die relativ großen Extrapolationsfehler, die in der Nähe von „Anticrossings“ auftreten, wurden durch Störungstheorie für fast entartete Bänder korrigiert.

Außerdem wurde eine Extrapolation der Übergangsmatrixelemente implementiert, die auf einer Entwicklung des Übergangsoperators nach den Wellenfunktionen in erster Ordnung Störungstheorie beruht. Es stellte sich jedoch heraus, daß beide Korrekturen für die Berechnung der dielektrischen Funktion von untergeordneter Bedeutung sind.

Unser Modellsystem Germanium in kubischem SiC besitzt einen deutlichen Typ-II-Heterostrukturcharakter. Lokalisierte besetzte Zustände treten in der Bandlücke der Matrix auf. Das Absorptionsspektrum wird unterhalb des Absorptionsansatzes der Matrix fast ausschließlich durch die Beiträge dieser Zustände bestimmt. In Übereinstimmung mit dem Typ-II-Charakter finden jedoch keine Übergänge zwischen den Bandkanten statt; die Übergänge erfolgen höher in das Leitungsband.

In Kenntnis der starken Übergänge in den freien Germaniumkristalliten wurde eine Einbettung von Germanium in hexagonalem SiC vorgenommen. Dieses hat eine größere Bandlücke, worauf wir folgerichtig Lokalisation sowohl von besetzten als auch von unbesetzten Zuständen fanden. Entgegen den Erwartungen an eine solche Typ-I-Heterostruktur ist der Einfluß dieser Zustände auf die optischen Eigenschaften jedoch vernachlässigbar; es wurden keine starken Übergänge zwischen den lokalisierten Zuständen gefunden. Die Übergangswahrscheinlichkeiten vergrößerten sich jedoch im Zuge der ionischen Relaxation der Systems, was die Druck- oder Verspannungsabhängigkeit der Materialien als Grund für die schwachen Übergänge nahelegt. Die Berechnung der Druckabhängigkeit der Übergangswahrscheinlichkeiten bestätigte, daß unsere Modellstrukturen nicht in der Lage sind, die experimentelle Situation in bezug auf die Verspannung zu reproduzieren. Das gleiche gilt deshalb auch für die Lumineszenzeigenschaften. Erste Schritte, die Verspannung des Materials auf einfachem Wege zu beheben, zeigten, daß es sich dabei um eine schwierige Aufgabe handelt.

Die Druckabhängigkeit der elektronischen Eigenschaften der Kristallite ist im wesentlichen durch die im Volumenmaterial bestehende Druckabhängigkeit der direkten und indirekten Bandlücken gegeben. Diese bestimmt gleichzeitig die Zusammensetzung der Kristallitzustände aus den volumenmaterialartigen Wellenfunktionen. Unter hohem hydrostatischen Druck werden Germaniumkristallite siliziumartig. Mit anderen Worten, die Hauptbeiträge zu den LUMO-Wellenfunktionen entsprechen jenen der indirekten Bandlücke des Siliziums. In der Sprache des Experiments heißt das: Die Kristallite werden quasi-indirekt.

Die Druckabhängigkeit der Anregungsenergien in Mischkristalliten ähnelt – entsprechend der Zusammensetzung des LUMO – jener im Volumenmaterial. Unsere Resultate sind dahingehend zu interpretieren, daß auch die Veränderung der Eigenschaften unter Druck und das *Confinement* unabhängig voneinander erfolgen. Dasselbe gilt für Druckabhängigkeit und die Mischungseffekte in $\text{Ge}_x\text{Si}_{1-x}$ NCs. Die Ergebnisse der vorliegenden Arbeit ermöglichen eine konsistente Interpretation der Eigenschaften der Kristallite.

Um die strukturelle Reaktion auf eine elektronische Anregung zu untersuchen, wurde die ionische Relaxation für mit einem Elektron-Loch-Paar angeregte Kristallite durchgeführt. Dabei wurde die T_d -Symmetrie der Kristallite als Nebenbedingung zugrunde gelegt. Dieses Verfahren lieferte relativ kleine strukturelle Beiträge zur Stokes-Verschiebung. Bei Freigabe der Symmetrie wurden, in Übereinstimmung mit kürzlich publizierten Resultaten anderer Gruppen, deutlich größere Stokes-Verschiebungen berechnet. Die Spinpolarisation wurde im Rahmen der LSDA ebenfalls untersucht. Es ergab sich nur ein unwesentlicher Unterschied zu den Stokes-Verschiebungen der nicht-spinpolarisierten Rechnungen.

Die Arbeit ordnet sich in die Anstrengungen der jüngsten Zeit ein, ein einheitliches Verständnis der Effekte und Strukturen von Nanokristalliten zu erreichen. Sie betrachtet die durch die räumlichen Quantisierungseffekte beeinflussten Eigenschaften und erbrachte in bezug auf einige der betrachteten Größen die ersten verfügbaren *ab-initio*-Resultate. Die methodischen bzw. theoretischen Hauptbeiträge sind die Behandlung der Paaranregungsenergien durch eine Δ SCF-Methode mit Besetzungszahlvorgabe sowie die Implementierung einer extrapolativen Variante der Tetraederintegration, die für Rechnungen mit großen Superzellen anwendbar ist. Aus praktischer Sicht wichtige Ergebnisse sind die Vorhersage der quasi-direkten starken Übergänge am Absorptionsansatz von Germaniumkristalliten sowie die gefundene weitgehende Unabhängigkeit von *Confinement*-Effekten, der Druckabhängigkeit sowie von Mischungseffekten.

Ehrenwörtliche Erklärung

Ich erkläre hiermit ehrenwörtlich, daß ich die vorliegende Arbeit selbständig, ohne unzulässige Hilfe Dritter und ohne Benutzung anderer als der angegebenen Hilfsmittel und Literatur angefertigt habe. Die aus anderen Quellen direkt oder indirekt übernommenen Daten und Konzepte sind unter Angabe der Quelle gekennzeichnet.

Bei der Auswahl und Auswertung des Materials haben mir die nachstehend aufgeführten Personen in der jeweils beschriebenen Weise unentgeltlich geholfen:

1. Prof. Dr. Friedhelm Bechstedt (als betreuender Hochschullehrer),
2. Dr. Jürgen Furthmüller (Betreuung in bezug auf die Numerik).

Weitere Personen waren an der inhaltlich-materiellen Erstellung der vorliegenden Arbeit nicht beteiligt. Insbesondere habe ich hierfür nicht die entgeltliche Hilfe von Vermittlungs- bzw. Beratungsdiensten (Promotionsberater oder andere Personen) in Anspruch genommen. Niemand hat von mir unmittelbar oder mittelbar geldwerte Leistungen für Arbeiten erhalten, die im Zusammenhang mit dem Inhalt der vorgelegten Dissertation stehen.

Die Arbeit wurde bisher weder im In- noch im Ausland in gleicher oder ähnlicher Form einer anderen Prüfungsbehörde vorgelegt.

Die geltende Promotionsordnung der Physikalisch-Astronomischen Fakultät ist mir bekannt.

Ich versichere ehrenwörtlich, daß ich nach bestem Wissen die reine Wahrheit gesagt und nichts verschwiegen habe.

Jena, den 04. 06. 2004

Lebenslauf

Hans-Christian Weißker

- geboren 12.07.1971 in Greiz.
- Schulbesuch „Polytechnische Oberschule“ 1978 – 1988.
- „Erweiterte Oberschule“ 1988 – 1990; Abitur Juli 1990.
- Ziviler Ersatzdienst September 1990 – August 1991; Altenpflegeheim.
- **Wissenschaftlicher Werdegang**
Physik, Friedrich-Schiller Universität in Jena, 1991–1998.
 - **Diplom:** 23.12.1998, Thema: Exzitonen im Magnetfeld.
 - Studienablauf
 - * Unterbrechung wegen eines Unfalls 1992.
 - * Oktober 1994 – März 1995 University of Wales Colleges of Cardiff, UK, mit einem Carl-Duisberg-Stipendium.
 - * September 1995 – Mai 1996 Purdue University, West Lafayette, Indiana, USA, mit einem Fulbright-Stipendium.
- Wissenschaftlicher Mitarbeiter seit März 1999;
Institut für Festkörpertheorie und -Optik, FSU Jena.
 - November 2002 bis April 2003, Aufenthalt am *Laboratoire des Solides Irradiés* der *École Polytechnique*, Palaiseau, Frankreich, mit einem „Marie Curie Training Site scholarship.“

Jena, 03.06.2004

Publikationsliste

Hans-Christian Weißker

- Structure- and spin-dependent excitation energies and lifetimes of Si and Ge nanocrystals from *ab initio* calculations;
H.-Ch. Weissker, J. Furthmüller, F. Bechstedt, Phys. Rev. B **69**, 115310 (2004).
- Influence of structural relaxation on the optical and electronic properties of embedded Ge nanocrystals;
H.-Ch. Weissker, J. Furthmüller, F. Bechstedt, Surf. Sci. **566–568**, 961 (2004).
- Classical versus *ab initio* structural relaxation: electronic excitations and optical properties of Ge nanocrystals embedded in a SiC matrix;
G. Cappellini, H.-Ch. Weissker, D. De Salvator, J. Furthmüller, F. Bechstedt, G. Satta, F. Casula, L. Colombo, J. Phys.: Condens. Mat. (submitted).
- Long-range contribution to the exchange-correlation kernel of time-dependent density functional theory;
S. Botti, F. Sottile, N. Vast, V. Olevano, L. Reining, H.-Ch. Weissker, A. Rubio, G. Onida, R. Del Sole, R.W. Godby, Phys. Rev. B **69**, 155112 (2004).
- Structural relaxation in Si and Ge nanocrystallites: Influence on the electronic and optical properties;
H.-Ch. Weissker, J. Furthmüller, F. Bechstedt, Phys. Rev. B **67**, 245304 (2003).
- Quantum structures in SiC;
F. Bechstedt, A. Fissel, J. Furthmüller, U. Kaiser, H.-Ch. Weissker, W. Wesch, Applied Surface Science **212**, 820 (2003).
- Validity of effective-medium theory for optical properties of embedded nanocrystallites from *ab initio* supercell calculations;
H.-Ch. Weissker, J. Furthmüller, F. Bechstedt, Phys. Rev. B **67**, 165322 (2003).
- Excitation Energies and Radiative Lifetimes of $\text{Ge}_{1-x}\text{Si}_x$ Nanocrystals: Alloying versus Confinement Effects;
H.-Ch. Weissker, J. Furthmüller, F. Bechstedt, Phys. Rev. Lett. **90**, 085501 (2003).
- Oscillator strengths and excitation energies of Ge and Si nanocrystals from *ab initio* supercell calculations;
H.-Ch. Weissker, J. Furthmüller, F. Bechstedt, Materials Sci. and Engineering B **101**, 39 (2003).
- GW self-energy calculations for systems with huge supercells;
J. Furthmüller, G. Cappellini, H.-Ch. Weissker, F. Bechstedt, Phys. Rev. B **66**, 045110 (2002).

- Optical properties of Ge and Si nanocrystallites from *ab initio* calculations. II. Hydrogenated nanocrystallites;
H.-Ch. Weissker, J. Furthmüller, F. Bechstedt, Phys. Rev. B **65**, 155328 (2002).
- Optical properties of Ge and Si nanocrystallites from *ab initio* calculations. I. Embedded nanocrystallites;
H.-Ch. Weissker, J. Furthmüller, F. Bechstedt, Phys. Rev. B **65**, 155327 (2002).
- Modification of SiC properties by insertion of Ge and Si nanocrystals;
H.-Ch. Weissker, J. Furthmüller, F. Bechstedt, Mater. Sci. Forum **389–393**, 743 (2002).
- Towards quantum structures in SiC;
F. Bechstedt, A. Fissel, U. Grossner, U. Kaiser, H.-Ch. Weissker, W. Wesch, Mater. Sci. Forum **389–393**: 737 (2002).
- Calculation of optical properties and density of states for systems with huge unit cells;
H.-Ch. Weissker, J. Furthmüller, F. Bechstedt, Phys. Rev. B **64**, 035105 (2001).
- First-principles calculation of optical properties: Application to embedded Ge and Si dots;
H.-Ch. Weissker, J. Furthmüller, F. Bechstedt, phys. stat. sol. B **224**, 769 (2001).
- Ge nanocrystals in SiC: *ab initio* calculations of optical properties;
H.-Ch. Weissker, J. Furthmüller, F. Bechstedt, Reviews and short notes to nano-meeting-2001, 156, World Scientific (2001).
- Prediction of optical properties of Si and Ge dots in SiC;
H.-Ch. Weissker, J. Furthmüller, F. Bechstedt, Mater. Sci. Forum **353–356**: 413 (2000).
- Optical properties of Si and Ge nanocrystals from *ab initio* calculations;
F. Bechstedt, H.-Ch. Weissker, J. Furthmüller, G. Cappellini, Proc. 25th ICPS, 1315, Osaka 2000.

Vorträge, Poster, Aktivitäten

Hans-Christian Weißker

Vorträge:

- 03.04. 2003 Palaiseau, Laboratoire des Solides Irradiés, École Polytechnique;
Séminaire: Simulations numériques des propriétés optiques des nanocristaux.
- 26.05. 2003 Modena, Italy; INFN S3 Center of Excellence;
Vortrag: Optical properties of Ge and Si nanocrystals from *ab initio* calculations.
- 06.11. 2003 Livermore, CA., USA; Lawrence Livermore National Laboratory;
Vortrag: Ionic relaxation and the optical and electronic properties of Ge and Si nanocrystals – *ab initio* calculations.

Konferenzteilnahmen:

- 27.03.–31.03. 2000 Regensburg; Frühjahrstagung der Deutschen Physikalischen Gesellschaft;
Poster: Parameterfreie Berechnung optischer Eigenschaften von Gruppe-IV-Nanokristalliten.
- 31.07.–03.08. 2000 München; QD2000 (Quantum-dot Conference);
Poster: First-principles calculation of optical properties: Application to embedded Ge and Si dots.
- 03.09.–07.09. 2000 Kloster Banz, European Conference on SiC and Related Materials;
Poster: First-principles calculation of optical properties: Embedded Ge and Si nanocrystals.
- 19.07.–22.07. 2000 Lyon, CECAM workshop;
Poster: First-principles calculation of optical properties: Embedded Ge and Si nanocrystals.
- 26.03.–30.03. 2001 Hamburg; Frühjahrstagung der Deutschen Physikalischen Gesellschaft;
Vortrag: Optical properties of nanocrystallites from *ab initio* supercell calculations.
- 22.05.–25.05. 2001 Minsk; Nanomeeting 2001;
Vortrag: Ge nanocrystals in SiC: *ab initio* supercell calculations of optical properties.
- 12.08–13.08. 2001 Lyon; CECAM workshop;
Poster: Optical and electronic properties of spherical Ge and Si nanocrystallites.
- 28.10.–02.11. 2001 Tsukuba, International Conference on SiC and Related Materials;
Poster: Modification of SiC properties by insertion of Ge and Si nanocrystallites – Description by *ab initio* supercell calculations.

- 11.03.–15.03. 2002 Regensburg; Frühjahrstagung der Deutschen Physikalischen Gesellschaft;
Vortrag: *ab initio* optical properties of group-IV-Nanocrystallites – The influence of strain and matrix.
- 06.02.–08.02. 2002 Genua; INFM Silicon workshop;
Poster: Optical properties of nanocrystals from *ab initio* supercell calculations.
- 18.06–21.06. 2002 Strasbourg; E-MRS Spring Meeting;
Vortrag: Oscillator strengths and excitation energies of Ge and Si nanocrystals from *ab initio* supercell calculations.
- 24.06–25.06. 2002 Paderborn: Arbeitskreistreffen Siliziumkarbid, (DFG Rundgespräch);
Vortrag: Optische Eigenschaften von in SiC eingebetteten Nanokristalliten – *ab-initio*-Rechnungen.
- 10.11.–13.11. 2003 Richmond, VA., USA; International Symposium on Clusters and Nano-Assemblies: Physical and Biological Systems;
Vortrag: (ausgewählt als “hot topic presentation”) & **Poster:** Influence of structural relaxation on the optical and electronic properties of Ge and Si nanocrystals.
- 07.09.–12.09. 2003 Prag; ECOSS 22 – European Conference on Surface Science;
Vortrag: Influence of structural relaxation on the optical and electronic properties of Ge and Si nanocrystals.

Teilnahme an Workshops / Kursen:

- 09.08.–18.08.1999 Trieste; Workshop on Calculation of Material Properties using Total Energy and Force Methods and *ab initio* Molecular Dynamics.
- 24.02.–01.03. 2001 Kerkrade; Workshop „Quantum Simulations of many-body systems: From Theory to Algorithms“;
Poster: Optical properties of nanocrystals from *ab initio* supercell calculations.

Arbeitsgruppenseminare – IFTO, Jena:

- 08.06.1999 Optical properties of embedded clusters – motivation and methods.
- 16.11.1999 A “new” tetrahedron method: Energies from extrapolation.
- 30.05.2000 Optical properties of free and embedded dots.
- 30.01.2001 Optical properties of NCs – a status summary.
- 11.12.2001 Optical properties of nanocrystals – The influence of strain and matrix.
- 03.06.2003 Optical properties of Ge and Si nanocrystals from *ab initio* calculations.
- 20.01.2004 Excitation energies of Si nanocrystals: Self-energy approach vs. Δ SCF method.